A dissertation submitted to the
Institute of Environmental Physics and Remote Sensing
Faculty of Physics and Electrical Engineering
University of Bremen, Germany
in partial fulfilment
for the award of the degree
Doctor of Natural Sciences
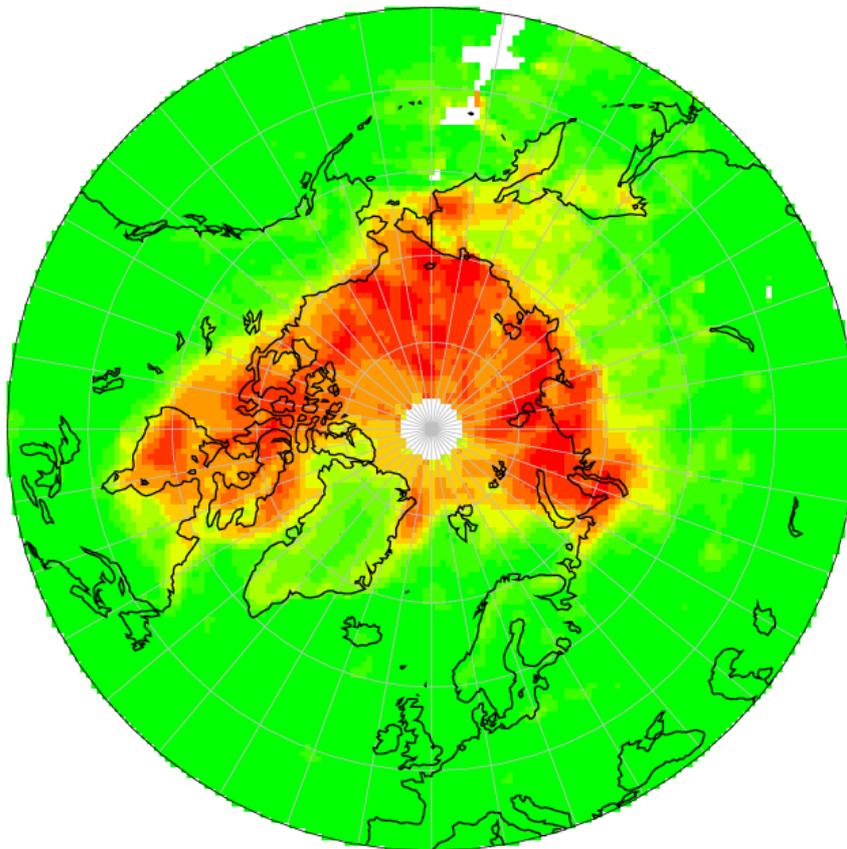
by

Oluyemi Temitayo Afe
B.Sc. (Hons) Engineering Physics, M.Sc (Physics)

Bremen, October 2005

Retrieval and Observations of Atmospheric BrO from SCIAMACHY nadir Measurements

Front-page Image: *BrO Explosion Event in Arctic Polar Spring*
(Monthly mean for April 2003) as observed by SCIAMACHY onboard ENVISAT.
Upper photo: ESA's ten-instrument ENVISAT in orbit has been observing the Earths
atmosphere for more than three years. Picture by EADS Astrium.
Credits: EADS Astrium, GmbH.

…. He stretches out the north over empty space, He hangs the world upon nothing. He binds up the water in His thick clouds, yet the clouds are not broken under it. He covers the face of His throne, and spreads his clouds over it. He drew a circular horizon on the face of the waters, at the boundary of light and darkness. The pillars of heaven tremble, and are astonished at his rebuke

Job 26: 7-11

Referees:

Prof. Dr. John P. Burrows
Institute of Environmental Physics
& Institute for Remote Sensing,
University of Bremen, Germany

Prof. Dr. Otto Schrems
Alfred Wegener Institute for Polar and Marine Research,
Bremerhaven, Germany

Dr. Andreas Richter
Institute of Environmental Physics
& Institute for Remote Sensing,
University of Bremen, Germany

Abstract

Measurements from the space-borne instrument SCIAMACHY launched in March 2002 onboard the ENVISAT platform, have been analysed for BrO absorption using the Differential Optical Absorption Spectroscopy (DOAS) method. BrO is an important atmospheric trace gas mainly responsible for the depletion of ozone in the polar boundary layer, the free troposphere and the stratosphere. Since 1995, global observations of BrO have been successfully demonstrated by the GOME instrument in several publications. This work reports the retrieval of BrO columns from the channel 2 UV/Visible spectral range of the SCIAMACHY nadir geometry. Although data analysis of GOME and SCIAMACHY BrO is very similar, a UV-shifted spectral range was employed to minimize the impact of residual structures from the polarisation sensitivity of the instrument. From this analysis, excellent agreement was obtained between the GOME and SCIAMACHY BrO columns. The impact of the improved spatial resolution of SCIAMACHY has also been utilised to explore the possibility for a volcanic source of BrO during major eruptions. In the polar regions over sea ice, frost flowers have been implicated as a major source of bromine to the atmosphere and BrO columns obtained from GOME and SCIAMACHY measurements correlates with areas potentially covered with frost flowers.

Contents

Chapter 1

Introduction

1.1 Vertical Structure of the Atmosphere

The earth's atmosphere consists of numerous gases the most abundant of which are nitrogen, N_2, (~78%) and oxygen, O_2, (~21%). See table 1.1 for a more detailed composition of the earth's atmosphere below 100 km. These gases and other particulate matter are attracted to the earth by the earth's gravitational field. The atmospheric pressure, p, decreases exponentially with height, h, according to the relation:

$$p(h) = p_0 . e^{-\frac{h}{h_s}} \qquad (1.1)$$

Where p_0 is the ground level pressure and h_s is the *scale height* (which is approximately ~7.5 km), i.e. the height at which the pressure has dropped to $1/e$.

Constituent	Molecular Weight	Content (fraction of total molecules)
Nitrogen (N_2)	28.016	0.7808 (75.51% by mass)
Oxygen (O_2)	32.00	0.2095 (23.14% by mass)
Argon (A)	39.94	0.0093 (1.28% by mass)
Water vapor (H_2O)	18.02	0 – 0.04
Carbon dioxide (CO_2)	44.01	325 parts per million
Neon (Ne)	20.18	18 parts per million
Helium (He)	4.00	18 parts per million
Krypton (Kr)	83.7	1 parts per million
Hydrogen (H)	2.02	0.5 parts per million
Ozone (O_3)	48.00	0 – 12 parts per million

Table 1.1: General Composition of the earth's atmosphere below 100 km [*Wallace and Hobbs*, 1977].

From equation 1.1 it follows that around 90% of the total mass of the atmosphere is found within the lowest 16 km and 99.9% within the lowest 50 km, corresponding to less than 1% of the earth's radius. The atmosphere can for most cases be treated as an ideal gas following the common gas law:

$$pV = Nk_B T \qquad (1.2)$$

Where V is the volume, N the number of molecules in that volume, T the temperature in Kelvin and k_B the Boltzmann constant.

The atmosphere is generally divided into regions/layers of different typical vertical temperature gradients, $-dT/dh$, or *lapse rates,* as seen in figure 1.1.
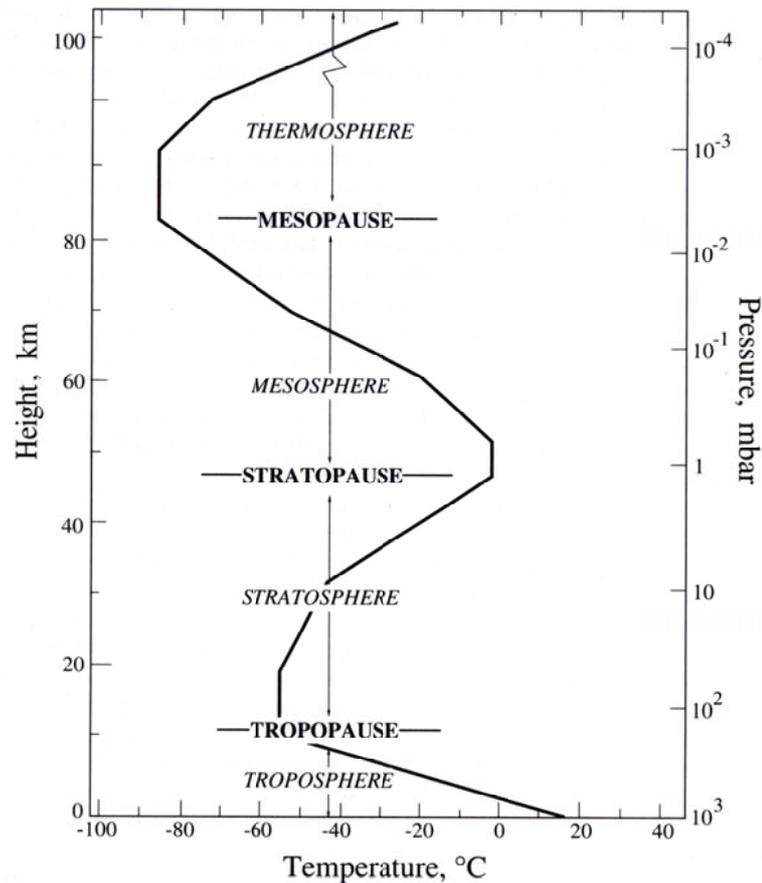
Figure 1.1: Vertical Temperature Profile depicting the Layers of the Atmosphere [*Wallace and Hobbs*, 1977].

In the lowermost layer, the *troposphere*, the temperature decreases with height due to strong surface heating. The *dry adiabatic lapse rate*, Γ_d, is 9.8 [K km^{-1}] for the troposphere. The wet adiabatic lapse rate, taking into account condensation of water vapor, is variable but always lower. The troposphere is characterized by strong turbulence and significant vertical mixing. Essentially all clouds, precipitation and water vapor are found in this layer. The troposphere extends up to the tropopause, defined as the altitude where $\Gamma_d < 2$ [K km^{-1}], which occurs at altitudes around 15 km at the equator and 7 km in high latitudes.

The layer above the tropopause is called the *stratosphere* and is characterized by a negative lapse rate due to increased heating from UV-photolysis of mainly O_3 (see section 2.1). Due to the negative lapse rate, the stratosphere is very stable with low vertical mixing and turbulence. In addition, the mixing between the troposphere and the stratosphere is small. The stratosphere is very dry (a few ppm H_2O), since virtually no water can cross the cold tropopause ($\sim$ 210 K), and since only small amounts are formed within the stratosphere from destruction of CH_4 molecules.

In the *mesosphere*, extending from approximately 50 km to 85 km, the lapse rate is again positive since the ozone concentration is decreasing with altitude. The coolest temperatures (<180 K) of the atmosphere are found at the summer mesopause for high latitudes, see figure 1.1. Above ~85 km the temperature will increase with height once more, this time mainly due to photolysis of O_2 and N_2. This region is denoted the *thermosphere*. Chemical and physical processes of these four regions can be substantially different.

1.2   General Dynamics

Transport of particles and chemical species between the stratosphere and troposphere is a key process in atmospheric chemistry. For example, anthropogenic species transported from the troposphere into the stratosphere initiate the chemistry responsible for stratospheric ozone depletion. Conversely, downward transport from the stratosphere represents a significant source of ozone into the troposphere and constitutes the ultimate removal mechanism for many stratospheric species, including those involved in ozone depletion. The phenomenon that distinguishes the troposphere from the stratosphere is the disparity in vertical mixing timescales. For example, vertical transport of air and chemical species throughout the depth of the troposphere can occur on timescales as short as a few hours via strong convective updrafts associated with large cumulus formation, whereas vertical transport over a similar altitude range in the stratosphere takes months to years. Inhomogeneous distribution of surface solar irradiation with latitude and season drives the Hadley circulation in the troposphere where air ascends at the Inter Tropical Convergence Zone (ITCZ) and descends at mid latitudes. This poleward motion of air in combination with the Coriolis force creates westerly zonal winds (jets), around the tropopause level. At latitudes higher than 30° large scale Rossby wave activity dominates. The stratosphere is dominated by large-scale ascent in the tropics and large-scale descent in the polar regions, with the strongest transport towards the winter hemisphere as outlined in figure 1.2. The transport is described as the 'global-scale fluid dynamical suction pump' [*Holton et al.*, 1995], and is driven by the breaking of planetary waves (such as Rossby waves) at high latitudes and the succeeding subsidence. The circulation is weaker than in the troposphere due to the stable conditions.
The part of the stratosphere whose isentropes[1] are found entirely above the tropopause ($\theta \geq 380K$) is denoted the '*over-world*' and should be distinguished from the lower most stratosphere where isentropic surfaces cross the tropopause, see figure 1.2 and from the '*under-world*' whose isentropes are entirely located in the troposphere. Stratospheric-tropospheric exchange (STE) can occur between the lower most stratosphere and the troposphere along these isentropes. Folding of the instantaneous tropopause and turbulent
mixing may also contribute to STE as well as cumulo-nimbus clouds in the ITCZ. Mixing between the southern hemisphere and the northern hemisphere and between the troposphere and stratosphere is relatively weak, having time scales of one year and several years respectively.

---

[1] A surface with constant potential temperature (θ), i.e. the temperature the air parcel would attain if adiabatically compressed to ground pressure (1000 hPa)
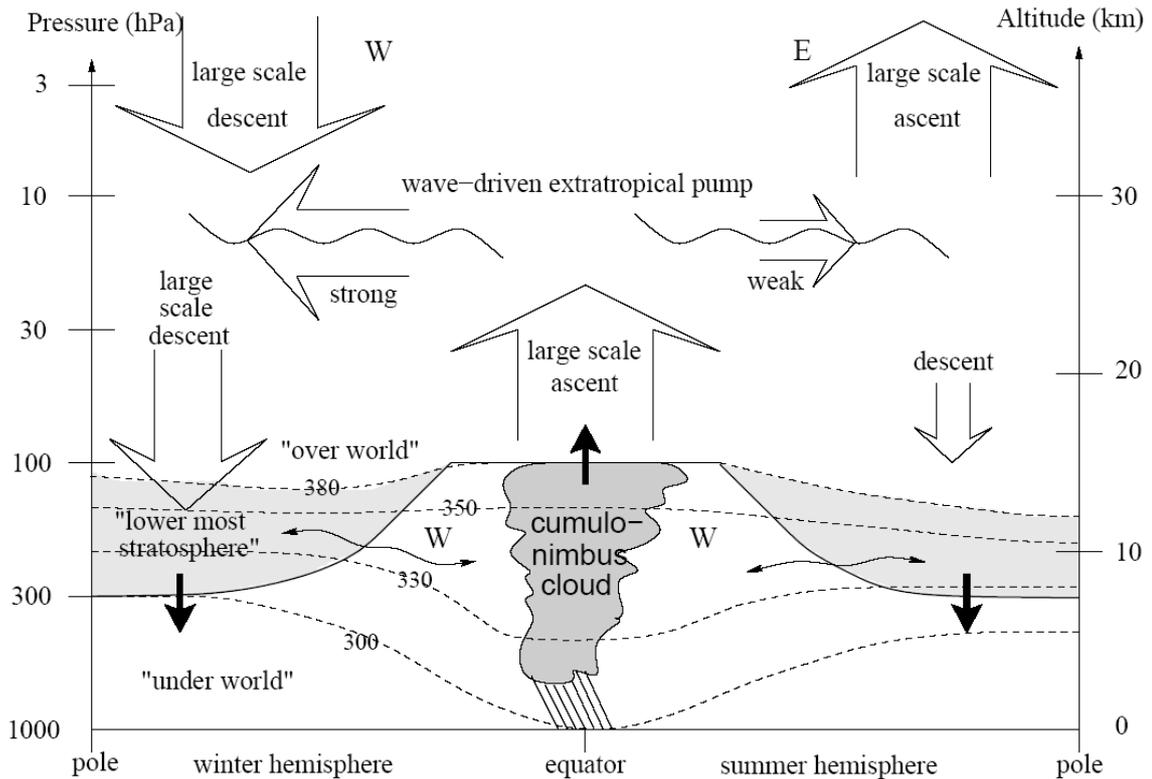
Figure 1.2: Dynamical illustration of stratospheric-tropospheric exchange of air masses. The thick line depicts the tropopause. Transport across the tropopause occurs both ways as large latitudinal displacements of the tropopause occur. The shaded regions within the stratosphere are areas where thin bands of stratospheric air intrude into the troposphere along strongly tilted isentropes (the so-called tropopause folding). STE and large-scale ascent takes place at the top of cumulonimbus clouds at the equator and along isentropes (dashed lines with temperatures [K]) at mid-latitudes between the lowermost stratosphere (shaded grey) and the upper troposphere. Large-scale subsidence of air masses is strongest in the winter hemisphere. The region of the stratosphere above 380 K potential temperature does not have direct STE exchange in the mid-latitudes. The broad arrows indicate transport by the global-scale circulation, which is driven by the 'extratropical pump'. Also shown are general wind direction, west (W) and east (E). From *Brohede.,* [2004].

The region of limited horizontal mixing at the over-world equator is named the '*tropical pipe*', [*Plumb*, 1996].

In the mesosphere, air is transported from the summer polar regions towards the winter hemisphere, driven by ozone heating in the lower regions. This creates the significant temperature gradients with extreme cold summer mesopause temperatures, through adiabatic expansion and compression. The transport produces strong mid-latitude easterly jets in the summer hemisphere and westerly in the winter hemisphere with maximum around the stratopause.

1.3 Radiation Balance of the Atmosphere: The Greenhouse Effect

Incoming solar radiation emitted from the Sun's photosphere and incident on the earth's atmosphere and surface determines the temperature of the earth's surface through its absorption and re-radiation. This energy is electromagnetic radiation in the visible wavelength region, with small amounts of infrared and ultraviolet radiation. Outside the earth's atmosphere, the solar flux approximates blackbody emission at ~ 5770 K. However, absorption and scattering of incoming solar radiation by atmospheric trace gases, in particular O_3, O_2, H_2O and CH_4 and other constituents modifies the spectral distribution. The attenuation due to the presence of various naturally occurring atmospheric constituents is shown by the hatched areas in Figure 1.3.
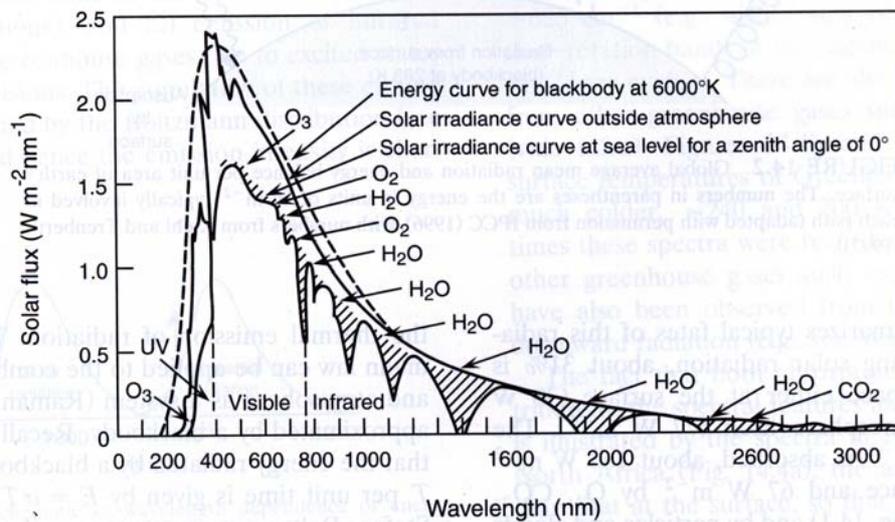
Figure 1.3: Solar flux outside the atmosphere and at sea level respectively. The emission of a blackbody at 6000 K is shown for comparison. The species responsible for light absorption (O_3, H_2O, etc.) are also shown [from *Howard et al.*, 1960].

The average incoming light intensity per unit area normal to the direction of propagation outside the earth's atmosphere, i.e., the solar constant, is 1368 W m^{-2}. This represents the energy density that would strike a planar disc of area πr^2. However, this incoming solar energy is spread over the entire $4\pi r^2$ surface area of the earth. The effective incoming solar radiation per unit area of the earth's surface is therefore 1368/4 = 342 W m^{-2}.

Figure 1.4 summarizes typical fates of this radiation. Of the incoming solar radiation, about 31% is reflected to space either at the surface (30 W m^{-2}) or by the atmosphere itself (77 W m^{-2}). The remaining 235 W m^{-2} is absorbed, about 168 W m^{-2} by the earth's surface and 67 W m^{-2} by O_3, O_2, H_2O and CO_2 and by particles and clouds in the atmosphere. While a small part of this (40 W m^{-2}) comes from direct emissions from the earth's surface in the atmospheric window where strong absorptions do not occur, the larger portion (165 + 30 = 195 W m^{-2}) comes from the lower temperature emissions from the greenhouse gases and the top of clouds (see figure 1.4). In addition, energy is also deposited in the atmosphere by convective, vertical mixing of surface heat through thermals (24 W m^{-2}), through the release of the latent heat of

evaporation of water when it condenses into liquid water (78 W m^{-2}), and by direct absorption of light (67 W m^{-2}).
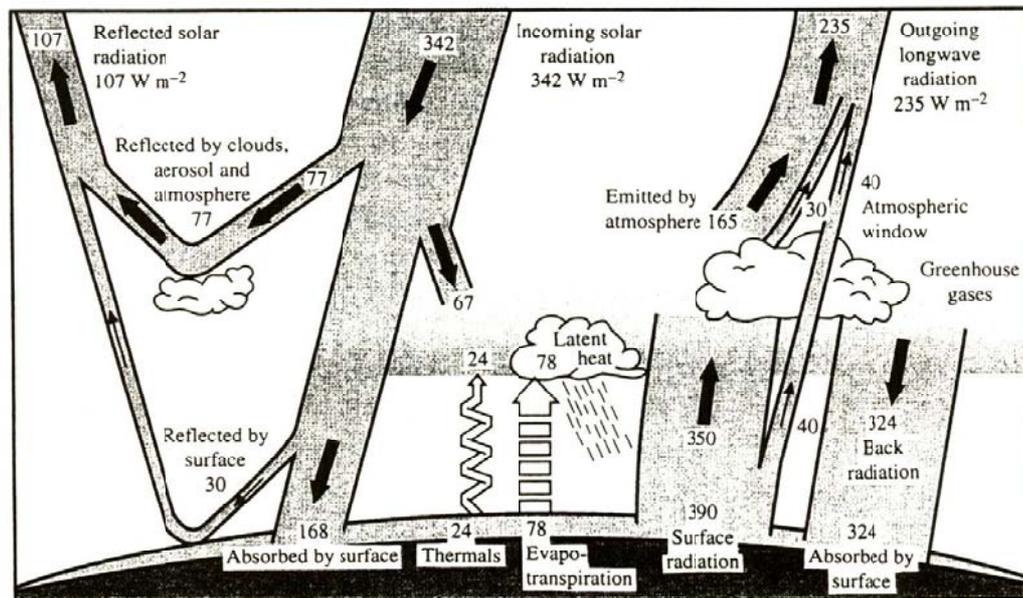
Figure 1.4: Global average mean radiation and energy balance per unit area of the earth's surface. The numbers are the energy in W m^{-2} due to the different contributions in the atmosphere and surface [from *Wayne*, 2000].

Since by the Stefan-Boltzmann law, 235 W m^{-2} of outgoing radiation corresponds to a temperature of 254 K, the emission of infrared radiation to space can then be thought of as occurring from an altitude where the temperature is 254 K, which is approximately 5.5 km above the earth's surface. In effect, then, infrared emissions to space by the greenhouse gases and clouds occur at lower temperatures than the corresponding absorptions. The 235 W m^{-2} of incoming solar radiation that is absorbed at the surface and in the atmosphere is ultimately balanced by the outgoing radiation from the upward emission (at lower temperatures) of ~195 W m^{-2} from atmospheric constituents, including the greenhouse gases and clouds, and of 40 W m^{-2} from the surface that occurs in the atmospheric window between the strong absorptions due to O_3, CO_2, and H_2O.

The difference of 155 W m^{-2} between the 390 W m^{-2} emitted by the earth's surface and the 235 W m^{-2} escaping from the atmosphere represents the amount of 'trapped' radiation known as the 'greenhouse effect'.

Chapter 2

Atmospheric Chemistry of Halogens Influencing Ozone

This chapter discusses the chemistry of halogen species in the atmosphere and their influence on atmospheric ozone. Stratospheric ozone depletion through catalytic chemistry involving e.g. man-made chlorofluorocarbons (CFCs) and halons is elucidated upon by revealing the key roles played by reactions of chlorine and bromine compounds on and within surfaces (heterogeneous chemistry), particularly under very cold conditions in polar regions. Mid-latitudinal ozone trends are also discussed. The sources of halogen compounds in the troposphere, in particular the marine and polar boundary layer and their impact on tropospheric ozone are highlighted. Finally, as the focus of this thesis is on the satellite measurements of atmospheric bromine monoxide (BrO), a section is devoted to its observation in the boundary layer, the free troposphere and the stratosphere.

2.1 Atmospheric Ozone

Ozone (O_3) is an important atmospheric trace gas that is naturally present in the earth's atmosphere. Discovered by C. F. Schönbein in 1839, it is characterized by a rather pungent odour noticeable around copy machines and laser printers that utilize electric discharge processes. Ozone is formed throughout the atmosphere in multistep chemical processes that require the absorption of ultraviolet (UV) radiation from the sun. About 90% of atmospheric ozone resides in the stratosphere, the peak at an altitude between ~15-30 km and because of the relatively high mixing ratios of O_3 initiated by the photolysis of molecular oxygen (reaction 2.1) at wavelengths $\lambda \leq 242$ nm [Chapman, 1930], this region of the atmosphere is generally referred to as the 'Ozone layer'.

$$O_2 + h\upsilon \rightarrow O + O \qquad (\lambda \leq 242\,\text{nm}) \qquad\qquad (2.1)$$

$$O + O_2 + M \rightarrow O_3 + M \qquad\qquad\qquad (2.2)$$

$$O_3 + h\upsilon \rightarrow O_2 + O\,(^1\text{D}) \qquad (\lambda \leq 320\,\text{nm}) \qquad\qquad (2.3)$$

$$O\,(^1\text{D}) + M \rightarrow \text{O} + M \qquad\qquad\qquad (2.4)$$

$$O_3 + h\upsilon \rightarrow O_2 + O \qquad (\lambda \leq 1180\,\text{nm}) \qquad\qquad (2.5)$$

$$O + O + M \rightarrow O_2 + M \qquad\qquad\qquad (2.6)$$

$$O + O_3 \rightarrow 2O_2 \qquad\qquad\qquad (2.7)$$
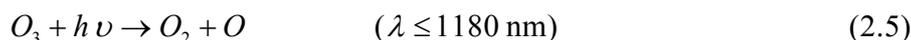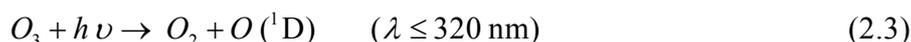
Chapman noted that ozone and atomic oxygen rapidly interchange with one another (reactions 2.2 to 2.6), while the sum of the two (reaction 2.7) is linked to much slower chemical processes.

Ozone in the troposphere has been steadily increasing due to a combination of a quasi-exponential growth in world population and industrialization leading to the increase in emission of nitrogen oxides and a host of hydrocarbons near the surface [e.g. *IPCC*, 2001; *WMO*, 2003]. Stratospheric ozone is considered beneficial to humans and other life forms because it offers protection by absorbing excessive and harmful solar UV-B radiation before reaching the troposphere. Ozone has an unusually strong absorption just at the critical wavelengths, λ, (230-290 nm). The UV region, λ < 400 nm, is often partitioned into what is known as the UV-A region (315-400 nm), the UV-B (280-315 nm) and the UV-C regions (200-280 nm). Excessive UV-B radiation can damage DNA, cause skin cancer and cataracts [e.g. *McKinlay and Diffey,* 1987]. It can also destroy terrestrial vegetation and the aquatic ecosystem [e.g. *Finlayson-Pitts & Pitts,* 2000]. Observations of integrated columns of ozone based on UV absorption in the earth's atmosphere began in the first few decades of the 20th century [e.g. *Fabry and Buisson,* 1913*; Dobson,* 1968, and references therein; *Dütsch*, 1974]. The total amount of ozone integrated from the surface of the earth to the top of the atmosphere, is often expressed in terms of *Dobson units* (DU)[*].
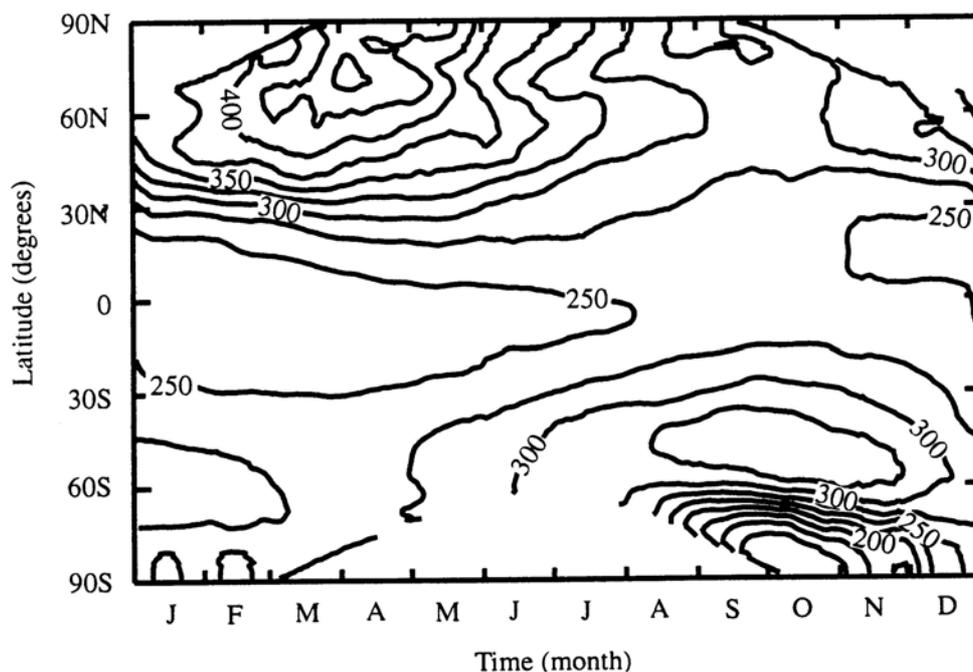
Figure 2.1: Averaged atmospheric ozone distribution as a function of latitude and season as observed by the space-borne GOME instrument in 1998. The contour lines are total overhead column abundances in Dobson units [*Burrows J. P. and Eichmann K. -U.*, IUP, University of Bremen, June 1999]. The plot was calculated using the GDP level 2 Version 2.3 dataset from DLR-DFD and ESA. *Figure from R. P. Wayne 2000.*

Average ozone column values range from ~250 DU (from the equatorial regions) to 450 DU (at the polar regions) over the globe the variability depending on latitude and season as illustrated in figure 2.1, as an example, which shows measurements from the GOME satellite instrument.

---

[*] 1 Dobson units = 10^{-3} atm cm ~ 2.69×10^{16} molecules cm^{-2} at standard temperature and pressure (273 K and 1 atmosphere).

Long-term ground-based measurements of ozone [e.g. *Staehelin et al.*, 1998a,b] coupled with satellite observations [e.g. *Hollandsworth et al.*, 1995; *Bodeker et al.*, 2001a] have revealed that the total ozone abundances over many regions of the globe have shown a downward trend since about 1980 [*Solomon*, 1999].

2.1.1   The Ozone Hole

In 1985 a team of scientists from the British Antarctic Survey (BAS) reported massive losses in total ozone columns measured from the ground over a period of about 8 years at Halley Bay, Antarctica, 76°S during polar sunrise (from September to October) of each year [*Farman et al.*, 1985; see also *Jones and Shanklin*, 1995]. It turned out much later from the measurements of the Total Ozone Mapping Spectrometer (TOMS) and the Solar Backscattered Ultraviolet (SBUV) instrument aboard the Nimbus 7 satellite, the scale of this unprecedented decline of total ozone during austral spring (referred to as the 'Antarctic Ozone hole') extends over several million square miles [e.g. *Stolarski et al.*, 1986]. Columns of ozone remain however even in the most extreme depletions observed for example in the mid 1990s when October ozone minima were near 100 DU over the south pole [*Hoffmann et al.*, 1997]. Evidence emerged that the dramatic depletion of stratospheric ozone over the Antarctic and the Arctic is conclusively linked to heterogeneous chemistry that occurs on the surfaces of Polar Stratospheric Clouds (PSCs) at cold temperatures in the polar vortex [*McElroy et al., 1986*; *Solomon et al.*, 1986; *Molina*, 1991]. However ozone depletion in the Arctic stratosphere is generally less dramatic compared to the Antarctic stratosphere [e.g. *Newman et al.*, 1997] due to warmer temperatures (~10 K higher) a less-stable polar vortex [*McCormick et al.*, 1982, *Pyle et al.*, 1992]. Measurements of large amounts of ClO, a key ozone destruction catalyst, indicate that the anthropogenic release of chlorofluorocarbons (CFCs) is the primary cause of this change [*Solomon et al.*, 1999]. The mechanism leading to the polar destruction of ozone in the stratosphere, at altitudes between ~12-24 km, requires the presence of two ingredients: *cold temperatures (as low as 183K) and sunlight.* The cold temperatures are needed to form the PSCs (which occur at altitudes between ~10-25 km) to provide the surfaces on which the heterogeneous reactions take place. The major reservoirs species $ClONO_2$, HCl and N_2O_5 react heterogeneously with PSCs, *on which HCl has been efficiently absorbed* to release photolytically active chlorine species Cl_2, $ClNO_2$, and HOCl. At sunrise, these gaseous chlorine species are photolysed to release free chlorine atoms that efficiently destroy ozone. For more details on the chemistry involving halogen destruction of stratospheric ozone under 'Ozone hole' and 'non-Ozone hole' conditions, see subsection 2.3 *(Stratospheric Halogen Chemistry).*

2.1.2   Ozone at Mid-Latitudes

After the discovery of the Antarctic Ozone hole, questions were raised on whether other latitudes, most especially the mid-latitudes, display significant ozone losses since this is where the bulk of human population resides. Detecting and quantifying ozone trends at mid-latitudes from anthropogenic contributions is complex due to the effects of natural variations in stratospheric ozone and to the interactions between the

various effects [e.g. *Krzyscin*, 1994; *Zerefos et al.*, 1997; *Hood*, 1997]. Thus, long-term trends in ozone must be extracted from variability due to e.g. the solar cycle, which has an 11-year period associated with it, as well as the quasi-biennial cycle (QBO), which is an oscillation of the zonal winds in the stratosphere around the equator and which has a 26-30 month cycle [e.g. *Kane et al.*, 1998; *Finlayson-Pitts and Pitts*, 2000]. For example, ozone column measurements were made at Reykjavíc from 1957-1990 by using a Dobson spectrometer and applying a stratospheric model that takes into account variations due to the seasons, the solar cycle and a linear trend. The combination of data and model showed a variation of 3.5±0.8% in O_3 column over a solar cycle and 2.1±0.6% over a QBO, on top of a linear trend of decreasing O_3 [*Bjarnason et al.*, 1993]. Secondly, there is an observed correlation between total column ozone and the El Niño Southern Oscillation (ENSO) in the tropical troposphere, with decreases in total ozone in middle and sometimes polar latitudes [*Zerefos et al.*, 1992]. *Harris et al.*, 1997 reported that at altitudes of 16-17 km in mid-latitudes, the ozone trend measured using SAGE (Stratospheric Aerosol and Gas Experiment satellite measurement) is as much as -20±8% per decade, whereas ozonesonde measurements in the Northern Hemisphere give an average of -7±3% per decade. Elaborate analysis of satellite, ground-based measurements (including the Umkehr techniques) and ozonesondes have established trends in significant ozone losses for northern and southern mid-latitudes which are observed to be typically larger in local winter and spring season than in summer [see e.g. *Ozone Trends Panel*, 1988 and references therein; *Stolarski et al.*, 1991; *Miller et al., 1995; McPeters et al.*, 1996a, b; *Harris et al.*, 1997; *Staehelin et al.*, 1998; *WMO*, 1999]. Mid-latitude ozone column trends as of the 1990s are of the order of ~5-10% much smaller than those of the Antarctic [*Jones and Shanklin*, 1985; *Hollandsworth et al.*, 1995; *Solomon et al.*; 1999]. As in Antarctica, analysis have shown that the bulk of the Northern mid-latitude ozone (35°N-60°N) decline is occurring in the lower stratosphere near ~12-20 km [*McCormick et al.*, 1992; *Miller et al.*, 1995; *WMO/UNEP*, 1994; *Bojkov and Fioletov*, 1997; *Harris et al.*, 1998]. In general, there is strong evidence for negative trends in total column ozone in mid and high latitudes particularly during winter and spring seasons, being -3 to -6% per decade in the Northern Hemisphere, and reaching as much as -10% in the Southern Hemisphere, largely as a result of the influence of polar ozone holes [*WMO*, 1999; *Wayne*, 2000]. The break-up of the polar vortices can lead to the dilution of mid-latitude ozone by ozone-poor air. However, the absolute magnitudes at a particular location and time have a high degree of uncertainty associated with them and large fluctuations are evident from year to year. Because of such uncertainties, trend analysis of ozone total column is an active area of current research.

2.1.3 Tropospheric Ozone

Whereas stratospheric ozone is thinning, tropospheric ozone is increasing [*IPCC*, 2001; *WMO*, 2003]. Tropospheric ozone serves as a major greenhouse gas [Mickley et al., 2001], thus playing a vital role in the energy balance of the atmosphere. It has both natural and anthropogenic sources. The primary natural source is in the form of stratospheric-tropospheric exchange (STE) which accounts for about 475 Tg (O_3)/yr based on observed correlations with other gases [*Murphy and Fahey*, 1994; *McLinden et al.*, 2000], while the main anthropogenic source of tropospheric ozone results from

the photochemical reactions of NO_2 produced by combustion of fossil fuel from human activities and the burning of large quantity of biomass [*Schultz et al.*, 1999; *Talbot et al.*, 1999]. Ozone abundances in the troposphere typically vary from less than 10 ppb over remote tropical oceans up to about 100 ppb in the upper troposphere, and often exceed 100 ppb downwind of polluted metropolitan regions. The current burden of tropospheric O_3 is about 370 Tg (O_3), which is equivalent to a globally averaged column density of 34 DU [*Park et al.*, 1999; *IPCC*, 2001]. Tropospheric O_3 represents the main source of hydroxyl radicals (OH) through its photolysis, which produces electronically excited oxygen atoms that rapidly combine with water vapor molecules to form OH.

$$O_3 + h\upsilon \rightarrow O(^1D) + O_2 \qquad (\lambda \leq 320 \ nm) \qquad (2.8)$$

$$O(^1D) + H_2O \rightarrow OH + OH \qquad (2.9)$$
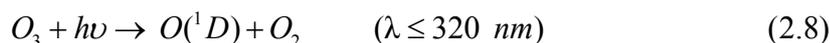
Since H_2O itself is a minor component of the atmosphere, reaction in process (2.9) is a minor fate of $O(^1D)$ atoms compared with quenching i.e.

$$O(^1D) + M \rightarrow O + M \qquad (M = N_2, O_2) \qquad (2.10)$$

$$O + O_2 + M \rightarrow O_3 + M \qquad (2.11)$$
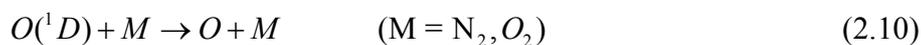
Approximately 70% of the OH radicals formed in reaction (2.9) react with CO and 30% with methane (CH_4), in the unpolluted atmosphere [*Wayne*, 2000].

$$OH + CO \rightarrow H + CO_2 \qquad (2.12)$$

$$OH + CH_4 \rightarrow CH_3 + H_2O \qquad (2.13)$$

O_3 reacts with nitrogen dioxide (NO_2) to produce nitrate radicals (NO_3). These radical species in concert with O_3 largely determine the oxidative capacity of the atmosphere, keeping it clean of harmful chemical species, and their absence could exert dramatic and unpredictable consequences.

Production of O_3 in the tropical troposphere is believed to be controlled by the supply of nitrogen oxide radicals ($NO_x = NO + NO_2$) originating from lightning, biomass burning, and soils [*Jacob et al.*, 1996].

$$NO_2 + h\upsilon \rightarrow O + NO \qquad (\lambda < 400 \ \text{nm}) \qquad (2.14)$$

$$O + O_2 + M \rightarrow O_3 + M \qquad (2.15)$$

$$OH + CO \rightarrow H + CO_2$$

$$H + O_2 + M \rightarrow HO_2 + M \qquad (2.16)$$

$$HO_2 + NO \rightarrow OH + NO_2 \qquad (2.17)$$

$$net: CO + 2O_2 + h\upsilon \rightarrow CO_2 + O_3 \qquad (2.18)$$
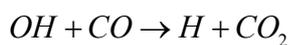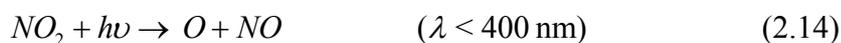
In tropospheric regions where *NO* concentrations are very low, peroxy radicals HO_2 and CH_3O_2 (produced from $(CH_3 + O_2 + M \rightarrow CH_3O_2 + M)$) are mainly consumed in the reactions:

$$HO_2 + HO_2 \rightarrow H_2O_2 + O_2 \qquad\qquad (2.19)$$

$$CH_3O_2 + HO_2 \rightarrow CH_3OOH + O_2 \qquad\qquad (2.20)$$
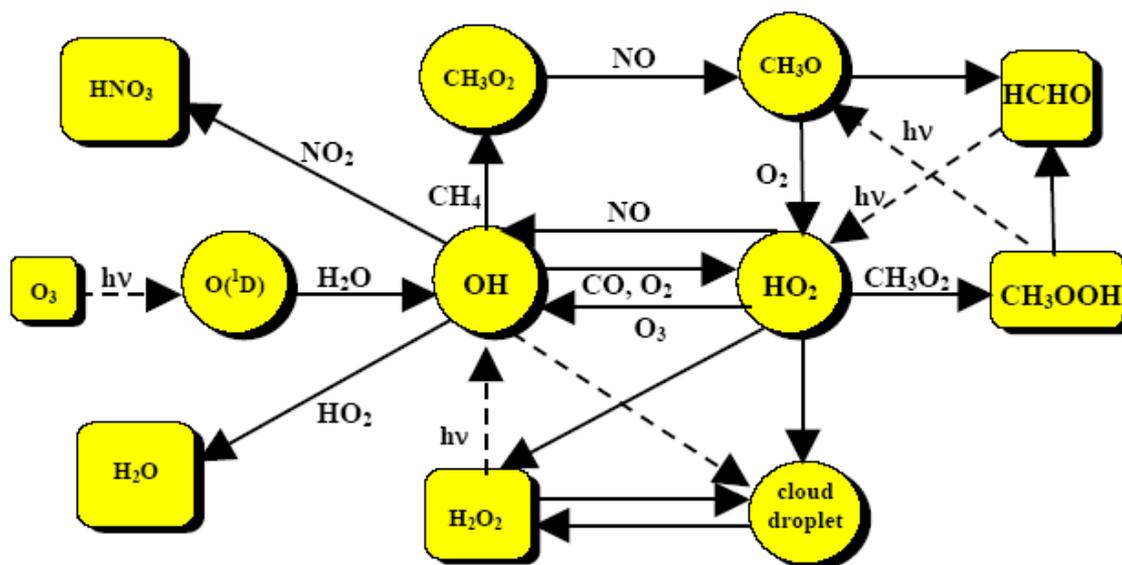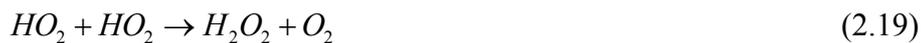
Figure 2.2: Schematic diagram that emphasizes the processes that create and destroy the OH and HO_2 radicals, key intermediates in oxidation steps of the chemistry in the troposphere. [*Adapted from Wayne, 2000*].

The hydrogen peroxide (H_2O_2) and the methyl hydroperoxide (CH_3OOH) are easily dissolved and readily removed by wet deposition. The figure above summarizes the key oxidation reactions involving the *OH* and *HO_2* radicals in tropospheric chemistry. Global model calculations suggest that most of the NO_x in the tropical troposphere is from lightning [*Lamarque et al.,* 1996] and satellite-based observations of large-scale tropospheric O_3 enhancements are associated with emissions of NO_x from lightning [*Martin et al.,* 2000]. This is in contrast to the large springtime enhancements of O_3 in the southern tropics caused by NO_x emissions from biomass burning [*Thompson et al.*, 1996; *Schultz et al.,* 1999].

2.2   Tropospheric Halogen Chemistry

2.2.1   Sources of Reactive Halogen Species in the Atmosphere

The mechanisms governing the release of reactive halogen species (RHS) in the troposphere has received increasing attention in recent years and has been the focus of many field, model and laboratory studies. Although there still remain some unresolved details, today, two major sources have been clearly identified: Liberation of halogens from sea-salt aerosols and degradation of partially halogenated organic compounds. These processes amongst other sources are described in more detail below.

Liberation from Sea Salt Aerosols:

- **Autocatalytic (or Halogen-catalysed) liberation from sea salt**: Deliquesced sea-salt aerosol is a large and rapidly cycling reservoir of liquid water in the marine boundary layer (MBL)[2] produced at the sea surface by the bursting of air bubbles [e.g. *Smith* 1872, *Keene et al.*, 1999]. In the marine boundary layer outside the polar regions, Bromide (Br−), a dominant form of inorganic bromine in sea-water [*Stumm and Brauner*, 1975], is injected into the atmosphere in association with sea-salt aerosol by the breaking of waves and biological processes on the ocean surface [*Mozurkewich*, 1995; *Tang and McConnell*, 1996; *Vogt* et al., 1996; *Sander et al.*, 2003]. In the high Arctic, it has been observed that the upward migration of sea salt ions to surface marine snowpack needs to be considered as a major source of sea salt aerosol in addition to wind-blown frost flowers and sea spray [*Domine et al.,* 2004]. Recently, frost flowers have been recognized as a prolific source of sea salt aerosol in the Antarctic, and it has been speculated that they could be involved in processes causing severe tropospheric ozone depletion events during polar sunrise [*Rankin et al.,* 2002]. Frost flowers are fragile ice crystals (*see figure 2.3*) that grow on frozen leads (linear breaks in sea ice cover) and polynyas (openings between drift ice and fast ice) [*Kaleschke et al.*, 2004]. They exhibit enhanced salinities of about 100g/kg and have a high specific surface area that would provide favorable sites for bromine activation [*Perovich and Richter-Menge*, 1994; *Rankin et al.,* 2002].

---

[2] The marine boundary layer (MBL) is in the lowest 500-1000 m deep part of the troposphere that is in direct contact with the sea surface. It is separated from the free troposphere by a temperature and humidity inversion and is generally well mixed.

Figure 2.3: Frost flowers on sea ice covering a lead: Stellar dendrites of about 1 to 2 cm height on young sea ice (Courtesy of Stefan Kern, University of Hamburg). The photograph was taken at 75°58´N 25°34´E, 24 March 2003. The air temperature was about –18°C. Image from *Kaleschke et al.,* 2004

Sea-salt contains (by weight) 55.7% Cl⁻, 0.19% Br⁻, and 0.00002% I⁻ [*Holland*, 1978; *Seinfeld and Pandis*, 1998]. The generation of sea-salt aerosols at the ocean surface outside the polar region is about 6.2 Tg/a of bromide [*Sander et al.*, 2003]. The global flux of sea salt is between 180 Tg/a and 10^4 Tg/a with a best estimate of 1500 Tg/a [*Jaenicke*, 1988; *Seinfeld and Pandis*, 1998]. Several processes of special interest in the troposphere releasing RHS from sea salt have been proposed and confirmed in the laboratory (*see figure 2.4 for a graphic overview*). [*Fan and Jacob*, 1992] proposed a reaction cycle converting Br− to Br_2:

Cycle I:

$$Br_2 + h\upsilon \rightarrow 2Br \qquad\qquad \lambda < 600\,nm \qquad\qquad (2.20)$$

$$2(Br + O_3) \rightarrow 2(BrO + O_2) \qquad\qquad (2.21)$$

$$2(Br + HO_2) \rightarrow 2(HOBr + O_2) \qquad\qquad (2.22)$$

$$2\,HOBr \rightarrow 2\,HOBr_{aq} \qquad\qquad (2.23)$$

$$2(HOBr_{aq} + H^+ + Br^-) \rightarrow 2(Br_{2,aq} + H_2O) \qquad\qquad (2.24)$$

$$2\,Br_{2,aq} \rightarrow 2\,Br_2 \qquad\qquad (2.25)$$

$$net: 2O_3 + 2HO_2 + 2Br^- + 2H^+ \rightarrow Br_2 + 4O_2 + 2H_2O \qquad\qquad (2.26)$$
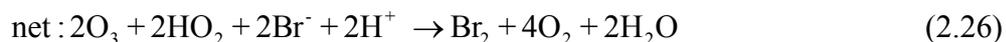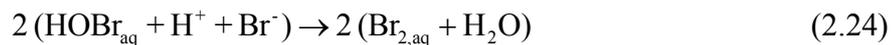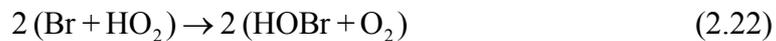
Vogt et al., 1996 proposed a similar set of reaction:

Cycle II: $\quad BrCl + h\upsilon \rightarrow Br + Cl \qquad\quad \lambda < 560\,nm \qquad\qquad (2.27)$

$$Br + O_3 \rightarrow BrO + O_2 \qquad\qquad (2.28)$$

$$BrO + HO_2 \rightarrow HOBr + O_2 \qquad\qquad (2.29)$$

$$HOBr \rightarrow HOBr_{aq} \qquad\qquad (2.30)$$

14

$$HOBr_{aq} + H^+ + Cl^- \rightarrow BrCl_{aq} + H_2O \qquad\qquad (2.31)$$

$$BrCl_{aq} \rightarrow BrCl \qquad\qquad\qquad (2.32)$$

$$net: O_3 + HO_2 + Cl^- + H^+ \rightarrow Cl + 2O_2 + H_2O \qquad (2.33)$$
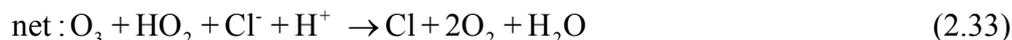
BrCl can also take part in the following aqueous autocatalytic cycle (when sufficient Br$^-$ is available) leading to the release of Br$_2$ [*Vogt et al.*, 1996].

Cycle III:

$$BrCl + h\upsilon \rightarrow Br + Cl \qquad \lambda < 560\,nm \qquad (2.34)$$

$$Br + O_3 \rightarrow BrO + O_2 \qquad\qquad\qquad (2.35)$$

$$BrO + HO_2 \rightarrow HOBr + O_2 \qquad\qquad\qquad (2.36)$$

$$HOBr \rightarrow HOBr_{aq} \qquad\qquad\qquad (2.37)$$

$$HOBr_{aq} + H^+ + Cl^- \rightarrow BrCl_{aq} + H_2O \qquad (2.38)$$

$$BrCl_{aq} + Br^- \leftrightarrow Br_2Cl^- \qquad\qquad\qquad (2.39)$$

$$Br_2Cl^- \leftrightarrow Br_{2aq} + Cl^- \qquad\qquad\qquad (2.40)$$

$$net: BrCl + O_3 + HO_2 + Br^- + H^+ \rightarrow Cl + Br_2 + H_2O + 2O_2 \qquad (2.41)$$
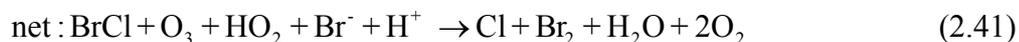
In cycles II and III, an additional Br$^-$ ion is released to the gas phase upon uptake of HOBr, which makes these cycles autocatalytic. If sufficient Br$^-$ is available and if gas phase Br loss processes are less than 50%, then these cycles lead to the exponential release of Br, which is often referred to as the 'Bromine Explosion'. It is important to note that reactions (2.20)-(2.41) are acid-catalyzed. Many laboratory studies [e.g. *Abbatt and Waschewsky*, 1998; *Mochida et al.*, 1998; *Fickert et al.*, 1999] have investigated the reaction cycles (2.20)-(2.41) with aqueous salt solutions or dry salt crystals and confirmed the rapid uptake of HOBr and the release of Br$_2$ and BrCl depending on the composition of the condensed phase. *Behnke et al.*, 1999 examined the reaction cycle of HOBr in a smog chamber with suspended sea salt aerosols of different composition and verified the cycles (2.20)-(2.41). Keene et al. [1998] studied the influence of the pH on halogen activation. They showed that significant sea salt dehalogenation is limited to acidified aerosol but that differences between a pH of 5.5 and 3 are not significant. *Fickert et al.*, 1999 verified that the production of Br$_2$ and BrCl upon uptake of HOBr onto aqueous salt solutions was pH-dependent with greater release/outgassing of Br$_2$ and BrCl for lower pH.
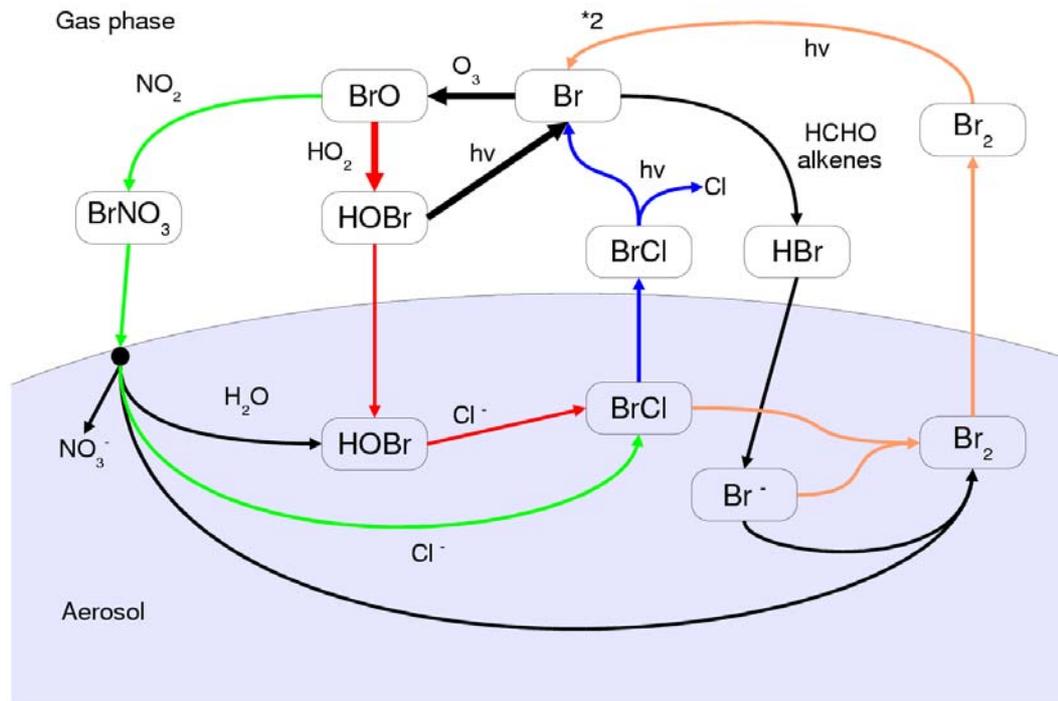
Figure 2.4: Simplified reaction scheme of the bromine chemistry in the MOCCA (Model Of Chemistry Considering Aerosols) box model in the MBL. Thick lines show the bromine-catalyzed ozone destruction cycle. Red lines show the heterogeneous production of aqueous-phase BrCl via HOBr. The green lines show an additional contribution via $BrNO_3$. If sufficient Br− is available, Br_2 is formed and escapes into the gas phase (orange lines). In bromide-depleted aerosols, BrCl escapes directly (blue lines). However, reactions involving halides are obviously restricted to sea-salt particles and to those sulfate particles that have scavenged some HBr and HCl from the gas phase (from *Sander et al.*, 1999).

- **Halogen release via reaction of Nitrogen Oxides on salt surfaces**

Under polluted conditions, the reactions of N_2O_5 and NO_2 with NaCl, KBr and salt surfaces is known to release XNO and XNO_2 [e.g. *Behnke et al.,* 1992, 1993; *Finlayson-Pitts and Johnson*, 1988; *Zetsch and Behnke*, 1993; *Behnke et al.,* 1994] via the following reactions:

$$N_2O_5 + H_2O \ \rightarrow \ 2HNO_{3,aq} \tag{2.42}$$

$$N_2O_5 + NaX \ \rightarrow \ XNO_2 + NaNO_3 \qquad (\text{where } X = Cl, Br \text{ or } I) \tag{2.43}$$

$$2\,NO_2 + NaX \ \rightarrow \ XNO + NaNO_3 \tag{2.44}$$

It was shown that the uptake of N_2O_5 leading to the release of halogen nitrites from sea salt aerosols competes with the reaction with water. Photolysis of XNO_2 and XNO releases halogen radicals to the gas phase. Similar reactions have been proposed for the uptake of XNO_3 [*Sander et al.*, 1999, 2003]. However, in clean marine air, the concentrations of nitrogen oxides are low and thus these reactions cannot explain the large bromine deficits measured in unpolluted regions of the MBL [e.g. Sander et al., 2003].

- **Halogen release via the action of strong acids on Halides**

Hydrogen halides can be liberated from sea salt aerosols by the action of strong acids such as H_2SO_4 and HNO_3.

$$H_2SO_4 + 2\,NaX_{(aerosol)} \rightarrow 2\,HX + Na_2SO_4 \qquad (2.45)$$

In polar regions, the recycling of gaseous HX through heterogeneous reaction is a possibility and can be of importance [e.g. McFiggans et al. 2000; Sander et al. 1999; *Vogt et al.,* 1999]. They can also be of significance in the remote marine boundary layer [e.g. *Seisel and Rossi*, 1997].

- **Degradation from (Partially) Halogenated Organic Compounds**

It has been known for several decades that oceanic phytoplankton emits CH_3X [e.g. *Lovelock et al.,* 1973; *Lovelock, 1975; Giese et al.,* 1999]. Degradation of short-lived organohalogen compounds like CH_3Br [e.g. *Khalil et al.,* 1993; *Yokouchi et al.,* 2000) and $CHBr_3$ [*Quack and Wallace*, 2003] via photolysis and reaction with OH also represents a source of inorganic bromine in the marine boundary layer. Global fluxes of 0.043 to 0.244 Tg/a of CH_3Br and 0.1965 Tg/a of $CHBr_3$ have been reported [*WMO* (1998)]. However, these numbers are upper limits for the contribution to inorganic reactive bromine because only a part of these molecules reacts in the MBL [*Sander et al.,* 2003].

- **Biomass Burning**

Biomass burning is a significant source of reactive halogen such as Br, which is emitted into the atmosphere during combustion [*Crutzen et al.,* 1979; *Crutzen and Andreae,* 1990; *Levine,* 1996; *Andreae et al.,* 1996; *McKenzie et al.,* 1996]. Inefficient combustion, which is typical of smouldering processes, was found to be associated with large emissions of CH_3Cl with a possibility due to the reaction:

$$CH_3OH + HCl \rightarrow CH_3Cl + H_2O \qquad (2.46)$$

Particulate Br is enriched in biomass burning plumes, particularly from savanna fires [e.g. *Echalar et al.,* 1995; *Maenhaut et al.,* 1996b; *Andreae et al.,* 1998; *Kleeman et al.,* 1999; *Sander et al.,* 2003]. It appears to be a significant source of dichloromethane (CH_2Cl_2) and the single largest natural contributor of organic chlorine in the atmosphere in the form of methyl chloride (CH_3Cl) [e.g. *Lobert et al.,* 1999]. Methyl bromide (CH_3Br) represents ~55% of the organic bromine at the tropical tropopause [*Schauffler et al.,* 1998; *Kourtidis et al.,* 1998]. The global average mixing ratio of atmospheric CH_3Cl is about 540 pptv[*][*Lobert et al.,* 1999; *Khalil et al.,* 1999].

---

[*] 1 pptv = 1 molecule gas per 10^{12} molecules air

- **Volcanoes**

  Volcanic eruptions can be sufficiently explosive that they inject large quantities of gases and particles into the stratosphere [e.g. *Finlayson-Pitts and Pitts*, 2000]. Volcanoes are significant sources of SO_2, HCl, HF, and SiF_4 [e.g. *Mankin and Coffey*, 1984; *Symonds et al.*, 1988; *Bekki*, 1995; *Francis et al.*, 1995]. In the troposphere, most of the HCl is rapidly removed by uptake on aerosols and subsequent wet deposition. Recently, bromine monoxide (BrO) was observed in large amounts (up to $2.0E15$ molecules cm^{-2}) from the degassing vents of the Soufrière Hills volcano on Montserrat by ground-based spectroscopic instruments [*Bobrowski et al.*, 2003]. Similar observations have been reported from the Stromboli, Etna, Villarica and Masaya volcanic plumes, though the $BrO:SO_2$ amounts were smaller compared to that observed on Montserrat [*Bobrowski et al.*, 2005]. For large eruptions however, satellite evaluations of volcanic plumes from SCIAMACHY and GOME measurements reveal that relatively little BrO could be seen from the plumes of active volcanoes [*Afe et al.*, 2004]. *See section 7 for more details.*

- **Industrial Emissions and Fossil fuel Burning**

  Halons are brominated organic compounds. They have anthropogenic sources and are used primarily as fire extinguishers. Halons currently represent the bulk of the organic bromine accounting for ~38% at the tropical tropopause [*Schauffler et al.*, 1998]. In the troposphere (i.e., lower atmosphere), observations show that the total combined effective abundance of ozone-depleting compounds continues to decline slowly from the peak that occurred in 1992-1994 [*WMO*, 1998]. Total chlorine is declining, while bromine from industrial halons is still increasing, albeit at a slower rate than was occurring previously (and as reported in the 1998 Assessment). Total tropospheric *chlorine* from the long- and short-lived chlorocarbons was about 5% lower in 2000 than that observed at its peak in 1992- 1994, and the rate of change in 2000 was about ~22 parts per trillion per year (−0.6% per year) [*UNEP/WMO*, 2002]. The once-dominant influence of methyl chloroform (CH_3CCl_3) on this total decline is diminishing because the atmospheric abundance of methyl chloroform is sharply decreasing. Total tropospheric bromine from halons continues to increase at about 3% per year, which is about two-thirds of the rate for 1996 reported in the 1998 Assessment of the WMO report. The observed abundances of CFCs, hydrochlorofluorocarbons (HCFCs), and methyl chloroform in the lower atmosphere continue to be consistent with reported production and estimated emissions. [*UNEP/WMO*, 2002].

2.2.2 Chlorine Chemistry in the Troposphere

The generation of sea salt aerosol by turbulence at the air-sea interface is the major source of Cl in the Earth's atmosphere [*Graedel and Keene*, 1995, 1996]. Investigations of surface marine air in the Arctic and at lower latitudes over the past decade have provided compelling evidence that halogen radical chemistry significantly influences the composition of the MBL. Levels of chlorine of up to ~150 ppt have been observed in the marine areas [e.g. *Keene et al.,* 1993; *Pszenny et al.,* 1993; *Spicer et al.*, 1998]. However, measurements of hydrocarbons and non-radical Cl species in the MBL at mid-latitudes and in the tropics suggest that Cl atoms may be present at least occasionally at concentrations in the range 10^4-10^5 atoms cm^{-3} [*Keene et al.*, 1990, 1996; *Pszenny et al.*, 1993; *Singh et al.*, 1996; *Spicer et al.*, 1998]. At such concentrations, oxidation by Cl atoms would provide a major sink for dimethylsulfide and alkanes in the MBL.

$$Cl + CH_3SCH_3 \rightarrow HCl + CH_3SCH_2 \tag{2.47}$$

Chlorine (Cl$_2$) is of particular interest in the troposphere because atomic Cl efficiently oxidizes many alkanes, including methane (CH$_4$), which influences net O$_3$ production through subsequent reactions. In particular, the chlorine initiation of methane oxidation in the free troposphere can contribute more than 10%, and in some regions up to 50%, of the total rate of initiation [*Lary*, 2004].

$$Cl_2 + h\upsilon \rightarrow 2Cl \tag{2.48}$$
$$Cl + O_3 \rightarrow ClO + O_2 \tag{2.49}$$
$$Cl + CH_4 + O_2 \rightarrow HCl + CH_3O_2 \tag{2.50}$$
$$CH_3O_2 + CH_3O_2 \rightarrow CH_3O + CH_3O + O_2 \tag{2.51}$$
$$CH_3O + O_2 \rightarrow HO_2 + CH_2O \tag{2.52}$$
$$ClO + HO_2 \rightarrow HOCl + O_2 \tag{2.53}$$
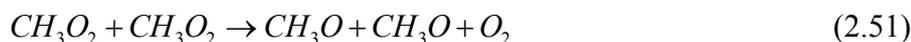
While Br atoms cannot abstract hydrogen from alkanes, part of the Cl atoms react with hydrocarbons to yield stable hydrochloric acid, HCl, and a peroxy radical (equation 2.50). In the case of methane the methylperoxy radical is formed, which is a precursor of formaldehyde (equation 2.51).

$$H^+ + Cl^- + HOBr \rightarrow BrCl + H_2O \tag{2.54}$$
$$H^+ + Cl^- + HOCl \rightarrow Cl_2 + H_2O \tag{2.55}$$

The lifetime of Cl atoms against reaction with methane is ~0.5 sec. [*Martinez et al.,* 1999]. HOBr or HOCl may heterogeneously oxidize HCl on ice surfaces (Equations 2.54, 2.55), to yield molecular halogens.

2.2.3   Bromine Chemistry in the Troposphere

The chemistry of bromine in the troposphere has received increasing attention in recent years most especially after the discovery of drastic depletions in boundary layer ozone in the Arctic in polar spring [e.g. *Oltmans and Komhyr*, 1986; *Barrie et al.*, 1988; *Hausmann and Platt,* 1994] and also recently in the Antarctic [*Frieß et al.*, 2004]. These low ozone depletion events were correlated with elevated concentrations of filterable bromine (f-Br) giving the first indication that reactive halogen species are involved in the destruction of ozone [*Bottenheim et al.,* 1988]. To facilitate the discussion in the following sections, a summary of the main bromine reaction cycles that are of importance for the troposphere is presented.

Bromine radicals are formed in the troposphere by the photolysis of molecular bromine or other species such as BrCl, HOBr, BrNO$_3$ or BrNO$_2$ (e.g. reactions 2.20, 2.27 and 2.47). These radicals rapidly react with O$_3$ thereby producing bromine monoxide.

$$Br + O_3 \rightarrow BrO + O_2$$
$$BrO + h\upsilon \xrightarrow{\ O_2, M\ } Br + O_3 \qquad (2.56)$$

Among the main O$_3$ destruction paths involving these radicals are reactions of BrO with HO$_2$:

$$Br + O_3 \rightarrow BrO + O_2$$
$$BrO + HO_2 \rightarrow HOBr + O_2$$
$$HOBr + h\upsilon \rightarrow Br + OH$$
$$OH + CO \xrightarrow{\ O_2\ } CO_2 + HO_2 \qquad (2.57)$$
$$net: CO + O_3 \rightarrow CO_2 + O_2 \qquad (2.58)$$
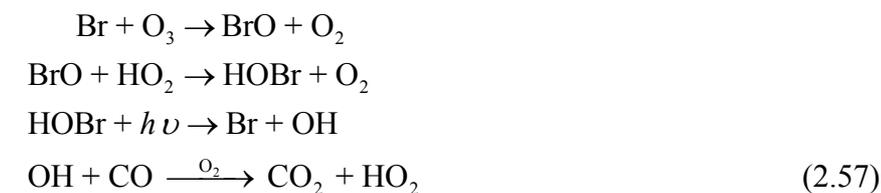
BrO self-reaction proposed by [*Barrie et al.,* 1988] represents a strong catalytic O$_3$ destruction cycle if large amounts of BrO are present especially during polar sunrise:

$$2(Br + O_3) \rightarrow 2(BrO + O_2)$$
$$BrO + BrO \rightarrow 2Br + O_2 \qquad (2.59)$$
$$\rightarrow Br_2 + O_2 \qquad (2.59)$$
$$Br_2 + h\upsilon \rightarrow 2Br$$
$$net: \quad 2O_3 \rightarrow 3O_2 \qquad (2.60)$$
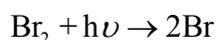
The cross-reactions between BrO and ClO may also play a role in tropospheric O$_3$ loss:

$$Br + O_3 \rightarrow BrO + O_2$$
$$Cl + O_3 \rightarrow ClO + O_2$$
$$BrO + ClO \rightarrow Br + Cl + O_2 \qquad (2.61)$$
$$net: \quad 2O_3 \rightarrow 3O_2$$
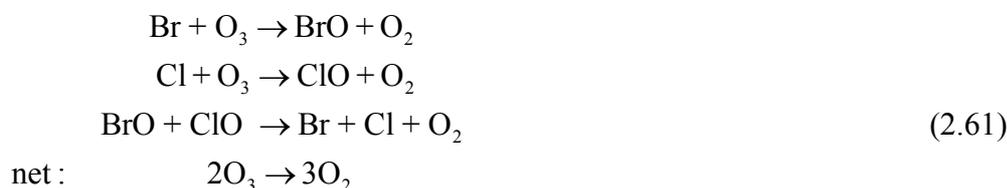
In region with elevated amounts of NO_x, bromine nitrates are formed which can either photolyse or react on surfaces:

$$BrO + NO_2 \rightarrow BrNO_3 \tag{2.62}$$

Of special interest in the troposphere are reactions that release halogens from salt deposits or sea salt aerosols, which has already been discussed in detail in the preceding section. BrO has also been postulated to be an important sink for dimethylsulfide (DMS) and O_3 in the marine boundary layer (equation 2.63) [*Toumi,* 1994]. BrO contributes roughly 44% to the oxidation of DMS and new kinetic data for this reaction suggests that BrO could be detected in the atmosphere by measurements of the ratio DMSO/DMS [*Ingham et al.,* 1999]:

$$BrO + CH_3SCH_3 \rightarrow CH_3S(O)CH_3 + Br \tag{2.63}$$
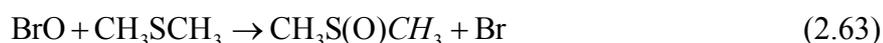
BrO also causes significant O_3 depletion in the MBL through catalytic cycles involving iodine oxide:

$$BrO + IO \rightarrow Br + I + O_2 \tag{2.64}$$

$$I + O_3 \rightarrow IO + O_2 \tag{2.65}$$

$$net: \ 2O_3 \rightarrow 3O_2 \tag{2.66}$$

2.2.4 Iodine Chemistry in the Marine Boundary Layer

Photochemical production of gaseous iodocarbons emitted from the ocean surface is the principal source of iodine for the atmosphere [*Richter and Wallace,* 2004]. The recent demonstration of the chamber formation of new particles from the photolytic production of condensable iodine-containing compounds from diiodomethane (CH_2I_2) [*O' Dowd et al.,* 2002; *Kolb,* 2002; *Jimenez et al.,* 2003a] provides an additional mechanism to the gas-to-particle conversion of sulphuric acid formed in the photo-oxidation of dimethylsulphide for marine aerosol repopulation. CH_2I_2 is the dominant organic iodine species released from seaweeds and the common rocky shore algae Laminaria digitata and Laminaria saccharina [*Carpenter et al.,* 1999, 2000; *McFiggans et al.,* 2004] and has been suggested as an initiator of particle formation. Photolysis of these compounds in the troposphere is rapid (lifetimes of minutes to days) and the resulting iodine atoms rapidly react to form IO and other reactive species (*see figure 2.5 below for the different chemical pathways*). These species in turn play significant roles in the chemistry of the troposphere and potentially in some parts of the lower-stratosphere.
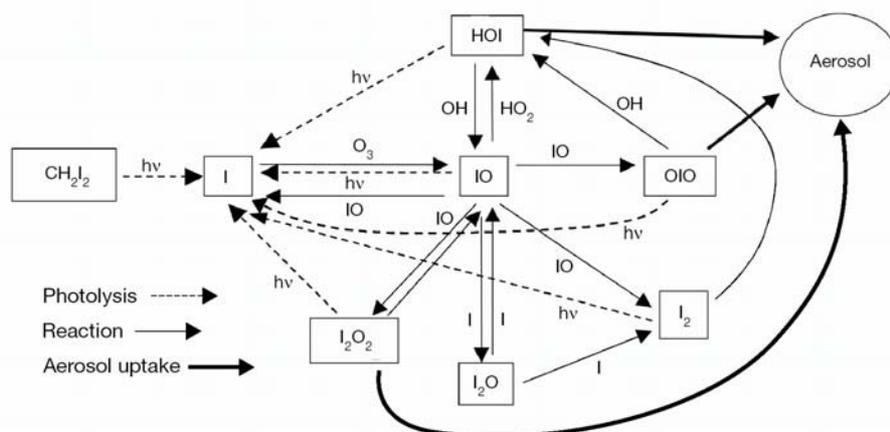
Figure 2.5: Chemical pathways from CH_2I_2 to aerosol production, on the basis of the current state of knowledge of the gas-phase chemistry [*from Colin O' Dowd et al., 2002*].

CH_3I and other alkyl halides like CH_2I_2 photolyze to form iodine atoms as depicted in the diagram above. These iodine atoms react with O_3, forming the IO radicals, which can potentially oxidize DMS to DMSO, regenerating iodine atoms in a chain process:

$$CH_3I + h\upsilon \rightarrow CH_3 + I \qquad (2.67)$$

$$I + O_3 \rightarrow IO + O_2 \qquad (2.68)$$

$$IO + CH_3SCH_3 \rightarrow I + CH_3S(O)CH_3 \qquad (2.69)$$
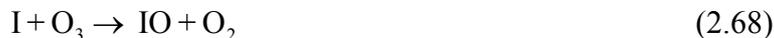
Several studies have developed gas-phase atmospheric oxidation mechanisms for iodine species [*Sander et al.,* 1997; *Vogt et al.,* 1999; *McFiggans et al.,* 2000], but the molecular routes leading to new particle formation and particle growth have not been unequivocally established [*Jimenez et al.,* 2003a]. Recently, observations of iodine oxides IO [e.g., *Alicke et al.,* 1999; *Wittrock et al.,* 2000; *Saiz-Lopez and Plane,* 2004; *Peters et al.,* 2005], OIO [*Allan et al.,* 2001; *Saiz-Lopez and Plane,* 2004] and molecular iodine, I_2, in the troposphere [*Saiz-Lopez and Plane,* 2004] at several coastal sites by ground-based DOAS measurements indicate that iodine chemistry significantly influences the formation of new particles and the oxidizing capacity of the atmosphere in the marine boundary layer.

2.3   Stratospheric Halogen Chemistry

In recent decades, various human activities have released ozone-destroying chemicals into the atmosphere. Of particular importance are halogen atoms, chlorine and bromine. Chemicals released into the atmosphere by industrial practices include chlorocarbon compounds (such as CCl_4 and CH_3Cl), chlorofluorocarbon compounds, CFCs, (such as $CFCl_3$ and CF_2Cl_2), and halons, especially CF_3Br (Halon-1301) and CF_2ClBr (Halon-1301). Chlorocarbon compounds are used primarily as industrial solvents, degreasing compounds, and CFC precursors. The CFCs are used as working

fluids in refrigeration and air conditioning systems, as foam-blowing agents, and through the 1970s, as aerosol propellants. The halons are used as fire suppressants. CFCs and halons have long lifetimes in the troposphere but once in the stratosphere, they are broken apart by solar ultraviolet radiation, releasing their chlorine or bromine atoms to initiate ozone destruction. For example:

$$CF_2Cl_2 + h\upsilon\,(\lambda < 240\,nm) \rightarrow CF_2Cl + Cl \tag{2.70}$$

Each chlorine atom can initiate a cycle that can destroy up to 100,000 ozone molecules. Bromine atoms are even more efficient destroyers. Probably the only continuous natural source of chlorine into the stratosphere is methyl chloride, CH_3Cl, which has a sufficiently long tropospheric lifetime (~1.5 years) [*Seinfeld and Pandis*, 1998]. Transport through the tropopause into the stratosphere ensures that a portion of CH_3Cl is photolysed while reaction with the OH radical is the primary loss process. However, regardless of the reaction pathway, the chlorine atom in CH_3Cl is released as active chlorine.

2.3.1   Chlorine Chemistry in the Stratosphere

Gas-Phase Chemistry in the Stratosphere (ClO$_x$ Cycles):

 The Cl atom released by photolysis of the CFCs reacts in a catalytic chain reaction that leads to the destruction of O_3:

$$Cl + O_3 \rightarrow ClO + O_2 \tag{2.71}$$
$$ClO + O \rightarrow Cl + O_2 \tag{2.72}$$
$$net: O_3 + O \rightarrow 2O_2$$
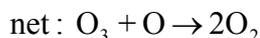
The reaction cycle (2.71) and (2.72) is important primarily in the middle and upper stratosphere where concentrations of oxygen atoms increase with altitude [e.g. *Garcia and Solomon*, 1994]. For the lower stratosphere, however, it is only responsible for ~5% of the total O_3 loss at 15 km and ~25% at 21 km [*Wennberg et al.*, 1994].
Most of the O_3 loss reaction associated with ClO$_x$ and BrO$_x$ is due to the following HO$_x$/ClO$_x$ cycle [*Solomon et al.*, 1986; *Crutzen and Arnold*, 1986]:

$$Cl + O_3 \; \rightarrow \; ClO + O_2 \tag{2.71}$$
$$ClO + HO_2 \; \rightarrow \; HOCl + O_2 \tag{2.73}$$
$$HOCl + h\upsilon \rightarrow Cl + OH \tag{2.74}$$
$$OH + O_3 \; \rightarrow HO_2 + O_2 \tag{2.75}$$
$$net: 2O_3 \; \rightarrow \; 3O_2$$

This cycle accounts for ~30% of the O_3 loss due to halogens in the lower stratosphere, and the corresponding cycle for bromine for ~20-30% [*Wennberg et al.*, 1994].
At lower altitudes where atomic oxygen levels are significantly lower, other cycles (NO$_x$/ClO$_x$) which involve the coupling of ClO$_x$ and NO$_x$ become important:

$$Cl + O_3 \rightarrow ClO + O_2 \qquad (2.71)$$
$$NO + O_3 \rightarrow NO_2 + O_2 \qquad (2.76)$$
$$ClO + NO_2 + M \rightarrow ClONO_2 + M \qquad (2.77)$$
$$ClONO_2 + hv \rightarrow Cl + NO_3 \qquad (2.78)$$
$$NO_3 + hv \rightarrow NO + O_2 \qquad (2.79)$$
$$\text{net:} \quad O_3 + O_3 \rightarrow 3O_2$$
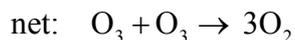
In addition, the ClO_x and the BrO_x cycles are interconnected by the reaction of ClO and BrO [*Yung et al.*, 1980*; McElroy et al.*, 1986; *Wayne et al.*, 1995]:

$$ClO + BrO \rightarrow Br + Cl + O_2 \qquad (2.80)$$
$$\rightarrow Br + OClO \qquad (2.81)$$
$$\rightarrow Br + ClOO \qquad (2.81a)$$
$$\rightarrow BrCl + O_2 \qquad (2.81b)$$
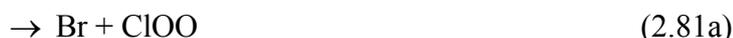
Reaction (2.81) is responsible for much of the uncertainty (~21%) in model predictions of O_3 loss in the Arctic [*Fish and Burton*, 1997].

The destruction of O_3 by chlorine and bromine can be 'short-circuited' by removing either Cl or Br or alternatively, ClO and BrO. For chlorine atoms, this occurs by the reaction with methane that has been transported from the troposphere:

$$Cl + CH_4 \rightarrow HCl + CH_3 \qquad (2.81)$$

ClO forms chlorine nitrate, by reaction with NO_2.
$$ClO + NO_2 \xrightarrow{M} ClONO_2 \qquad (2.77)$$

Both HCl and $ClONO_2$ are known as 'temporary reservoirs' for chlorine, since active chlorine can be regenerated via the reactions:

$$HCl + OH \rightarrow Cl + H_2O \qquad (2.79)$$
$$ClONO_2 + hv \rightarrow Cl + NO_3 \qquad (2.80)$$
$$\rightarrow ClO + NO_2 \qquad (2.81)$$
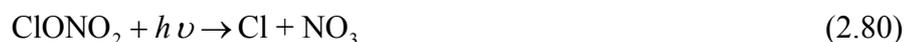
Partitioning of chlorine between reactive (e.g. Cl and ClO) and reservoir forms (e.g. HCl and $ClONO_2$) depends on temperature, altitude, and latitude history of an air parcel. For the mid-latitude, lower stratosphere, HCl and $ClONO_2$ are the dominant reservoir species for chlorine, constituting over 90% of the total inorganic chlorine [*Seinfeld and Pandis*, 1998].

Stratospheric Chlorine Chemistry under Ozone hole conditions:

Section 2.1.1. already gave an overview of the conditions necessary for the depletion of ozone in the polar stratosphere in austral spring. Here in this section, the chemistry and conditions taking place in the polar vortex under ozone hole conditions is discussed.

As noted, little ozone is produced in the polar stratosphere as the low sun elevation (large solar zenith angle) results in essentially no photodissociation of O_2. Thus catalytic cycles that require oxygen atoms were not able to explain the massive ozone depletion. Also, since the Antarctic ozone hole is sharply defined to altitudes between 12-24 km, the contribution from CFCs and halons to O_3 destruction was exonerated since they would be most effective at altitudes of ~40 km in the Antarctic stratosphere.

In 1987, Molina and Molina proposed that a mechanism involving the ClO dimer, Cl_2O_2, might be involved:

$$ClO + ClO + M \rightarrow Cl_2O_2 + M \tag{2.82}$$

$$Cl_2O_2 + h\upsilon \rightarrow Cl + Cl + O_2 \tag{2.83}$$

$$2(Cl + O_3 \rightarrow ClO + O_2) \tag{2.71}$$

$$\text{net: } 2O_3 + h\upsilon \rightarrow 3O_2$$
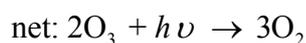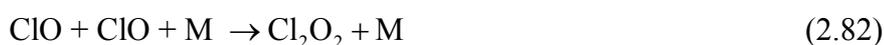
The termolecular reaction 2.82 is facilitated at higher pressures (i.e. larger M), and low temperatures and it has been shown to be responsible for ~40 % of the O_3 losses between 13-18km in the Antarctic springtime contributing to the 'ozone hole' formation (*Lee et al.*, 2002). Cl_2O_2 has been shown to have the symmetric structure ClOOCl [*McGrath et al*., 1990]. Photolysis of ClOOCl has two possible channels:

$$ClOOCl + h\upsilon \rightarrow Cl + ClOO \tag{2.84a}$$

$$\rightarrow ClO + ClO \tag{2.84b}$$

Reaction 2.84a is the main photolysis path [*Molina et al.,* 1990] and can lead to an ozone destruction cycle. The ClOO product rapidly decomposes to yield a Cl atom and O_2.

$$ClOO + M \rightarrow Cl + O_2 + M \tag{2.85}$$

If sufficient ClO could be generated, then the cycle of reactions 2.82, 2.83, 2.71 could lead to substantial O_3 depletion. However, solely gas-phase chemistry in the ClO_x system does not produce the necessary ClO concentrations to account for the ozone hole.

Polar Stratospheric Clouds (PSCs) and the Ozone Hole

Polar Stratospheric Clouds (PSCs) are formed during the long polar night from small amounts of water vapor that are condensed at temperatures as low as ~183 K at heights of between 15-20 km. The lower temperatures are more prevalent in the Antarctic than the Arctic presumably because of the more stable polar vortex. PSCs have been classified into two types; Type I and Type II PSCs. Type I PSCS have been further subdivided into Type Ia and Type Ib. Type Ia PSCs are composed of non-spherical crystals of nitric acid trihydrate, $HNO_3.3H_2O$ (denoted sometimes as NAT)

that form when temperatures are below ~195 K. Type Ib PSCs consist of supercooled solutions of $HNO_3/H_2SO_4/H_2O$ that form at the same temperature threshold. Type II PSCs are composed mainly of non-spherical, frozen water ice crystals that form at temperatures generally below the frost point (~188-190 K).

Heterogeneous reactions occurring on PSCs play the pivotal role in polar ozone depletion [*McElroy et al.,* 1986; *Solomon et al.,* 1986; *Molina,* 1991]. The ozone hole is sharply defined between about ~ 12-25 km. Liberation of active chlorine from the reservoir species HCl and $ClONO_2$ is rather slow, but the PSCs promote the conversion of the major chlorine species, HCl and $ClONO_2$, to photolytically active chlorine via the efficient absorption of gaseous HCl by PSCs. When stratospheric temperatures drop below 200 K, the stratospheric particles absorb water and allow HCl to be absorbed. This step is followed by the heterogeneous reaction of gaseous $ClONO_2$ with the particle (stratospheric aerosol, denoted by s) on the surface of the ice:

$$HCl\,(s) + ClONO_2 \xrightarrow[\text{fast}]{ice/particle} Cl_2 + HNO_3\,(s) \qquad (2.86)$$
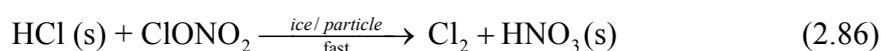
Molecular chlorine liberated, as a gas is rapidly photolyzed and nitric acid is retained in the particle.

$$HCl\,(s) + ClONO_2 \rightarrow Cl_2 + HNO_3\,(s) \qquad (2.86)$$

$$Cl_2 + h\upsilon \rightarrow 2Cl \qquad (2.87)$$

$$2[\,Cl + O_3 \rightarrow ClO + O_2\,] \qquad (2.71)$$

$$ClO + NO_2 + M \rightarrow ClONO_2 + M \qquad (2.77)$$

$$net:\, HCl + NO_2 + O_3 \rightarrow ClO + HNO_3\,(s) + 2O_2 \qquad (2.88)$$
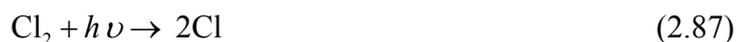
The reaction between $ClONO_2$ and H_2O (s) can also occur but it's very slow in the gas phase.

$$ClONO_2 + H_2O(s) \rightarrow HOCl + HNO_3\,(s) \qquad (2.89)$$

Gaseous HOCl rapidly photolyses to yield a free chlorine atom. The HOCl can also undergo a subsequent heterogeneous reaction [*Abbatt and Molina*, 1992].

$$HOCl + HCl(s) \rightarrow Cl_2 + H_2O \qquad (2.90)$$

If N_2O_5 is present, a further heterogeneous reaction reconverts HCl into active chlorine [*Hanson and Ravishankara*, 1991] and $ClNO_2$ released in the gas phase is rapidly photolyzed to yield active chlorine.

$$N_2O_5 + HCl(s) \xrightarrow[\text{fast}]{ice/particle} ClNO_2 + HNO_3\,(s) \qquad (2.91)$$

The mechanism of ozone destruction in the polar stratosphere is as follows. Two ingredients are necessary: *cold temperatures* (which are needed to form the PSCs to provide the surfaces on which the heterogeneous reactions takes place) and *sunlight*. The reservoir species $ClONO_2$ and N_2O_5 react heterogeneously with PSCs, on which HCl has been absorbed to produce gaseous Cl_2, HOCl, and $ClNO_2$. Subsequent photolysis of these species by sunlight follows during polar sunrise and free chlorine atoms are released which then react with ozone by reaction (2.71) to yield ClO, which accumulates. When the ClO concentrations are sufficiently large, the reactions (2.82), (2.84a), (2.85) and finally (2.71) becomes active:

$$ClO + ClO + M \rightarrow Cl_2O_2 + M \qquad\qquad (2.82)$$

$$ClOOCl + h\upsilon \rightarrow Cl + ClOO \qquad\qquad (2.84a)$$

$$ClOO + M \rightarrow Cl + O_2 + M \qquad\qquad (2.85)$$

$$2(Cl + O_3 \rightarrow ClO + O_2) \qquad\qquad (2.71)$$

$$\text{net: } 2O_3 + h\upsilon \rightarrow 3O_2$$
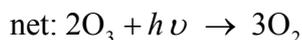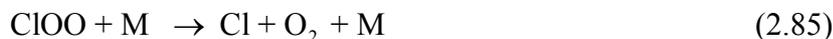
2.3.2   Bromine Chemistry in the Stratosphere

Brominated organic compounds are released into the atmosphere through a variety of natural and anthropogenic sources. Methyl bromide (CH_3Br) is the most abundant organobromine compound emitted into the stratosphere accounting for $\sim$ 55-60% of the total bromine loading [*Kourtidis et al.*, 1998; *Schauffler et al.*, 1998; *Wamsley et al.,* 1998]. The ocean and the terrestrial ecosystems (e.g. through biomass burning) accounts for the bulk of natural sources of methyl bromide which contributes $\sim$ 27-42% of the bromine loading currently in the stratosphere (*see figure 2.6 (i))* [*WMO,* 2002]. Very short-lived gases containing bromine, such as bromoform ($CHBr_3$), are also released to the atmosphere by the oceans. The estimated contribution of these gases to stratospheric bromine (about 15%) is uncertain at this time. Methyl bromide is used primarily as an agricultural fumigant. It is also used in quarantine treatment and insect and rodent controls. Halons are the second largest source of stratospheric bromine (comprising $\sim$38% of the organic bromine at the tropopause [*Schauffler et al.*, 1998].
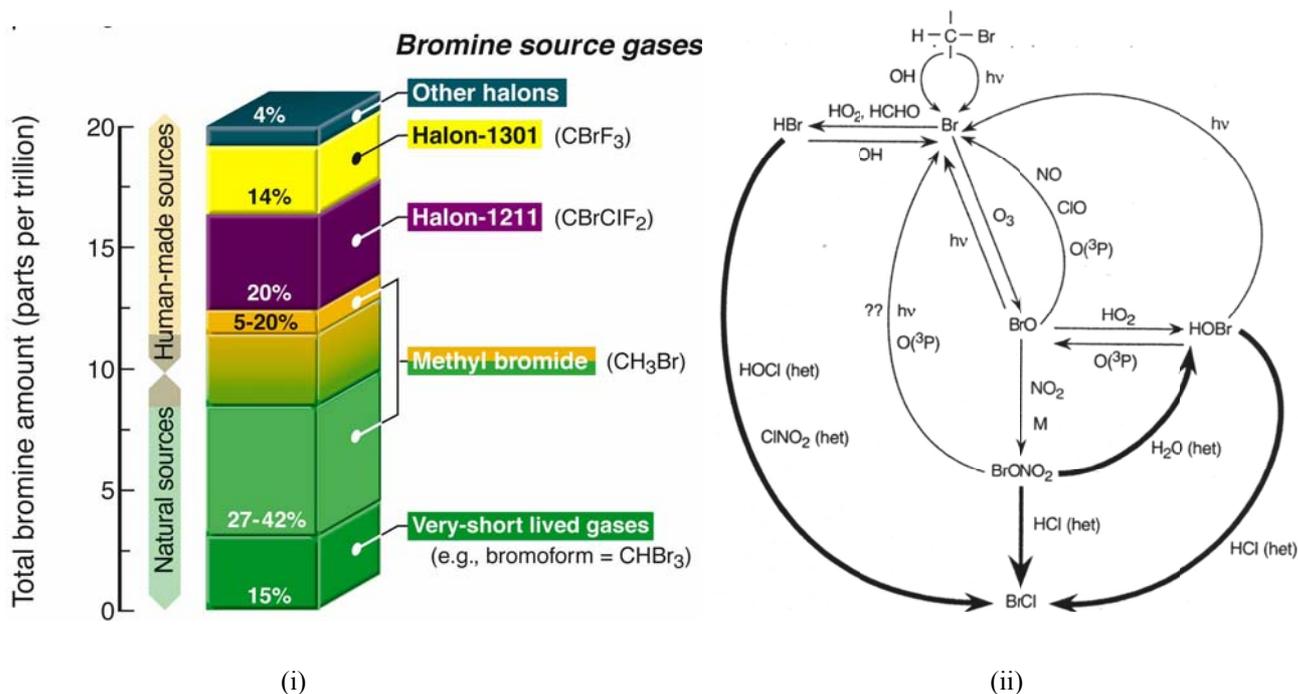
Figure 2.6: (i) Primary sources for bromine-containing compounds in the Stratosphere in 1999 (Left, *from WMO, 2002*) and (ii) the schematic of the gas phase and heterogeneous bromine chemistry in the stratosphere. The heavier dark lines show the heterogeneous chemistry [Right, *from Finlayson-Pits and Pitts, 2000*].

Figure 2.6 (ii) summarizes the most important chemistry of bromine in the stratosphere for both gas-phase and heterogeneous (shown as the darker lines) reactions. Once the bromine organics reach the stratosphere, they undergo photolysis in a manner similar to chlorofluorocarbons. Oxidation of organic bromine compounds to generate inorganic bromine is sufficiently fast that after a few years, inorganic forms comprise almost all of the stratospheric bromine [*Finlayson-Pitts and Pitts*, 2000]. For example, it has been shown that ~97.5% of stratospheric bromine is in the form of inorganic species in an air parcel that has been present in the stratosphere for about 6 years [*Wamsley et al*, 1998]. Bromine is more effective, per atom, in destroying O_3 than is chlorine for several reasons. First, unlike chlorine atoms, atomic bromine does not rapidly react with organics. For example, the reaction of Br with CH_4 is too slow to represent a significant loss process, unlike the analogous chlorine atom reaction. Atomic bromine does react with HCHO at a reasonable rate ($K^{298K} = 1.1 \times 10^{-12}$ cm^3 molecule^{-1} s^{-1}) as well as with higher aldehydes in the stratosphere. Another difference between chlorine and bromine compounds is their photochemistry. The absorption cross sections of bromine compounds tend to be larger than those of the corresponding chlorine compounds, especially at longer wavelengths where the intensity of the solar radiation available for photolysis is larger. Hence, the conversion of bromine compounds into active forms is generally faster. As a result, conversion of BrO to Br + O, for example, through photolysis is important for BrO but the analogous reaction for ClO is not. Indeed the lifetime of BrO with respect to photolysis in the stratosphere is of the order of seconds [*Lary*, 1996].

As discussed in section 2.3.1, the chemistry of ClO$_x$ and BrO$_x$ are closely interrelated via the gas-phase reactions of ClO and BrO (*see reactions 2.80, 2.81, 2.81a, 2.81b*), which play an important role in the Antarctic ozone hole formation.

2.3.3   Reactive Iodine in the Lower Stratosphere

Even though all the natural sources of iodine are short-lived, their upward transport via rapid convection in the tropics could supply iodine to the lower stratosphere [*Solomon et al.*, 1994]. *Davis et al.*, 1996, observed episodic transports of CH_3I as high as 1 ppt at ~ 10-12 km when a typhoon provided strong vertical upward motion. It was hypothesized that below ~ 20 km, iodine might contribute to ozone destruction if there were up to 1 ppt of iodine in the stratosphere. In this hypothesis, it was assumed that the reaction of IO with ClO would be very rapid [*Solomon et al.*, 1994], as in the case of the reaction of IO with itself or of IO with BrO. The rate coefficients for the reaction of IO were subsequently measured in the laboratory and found to be a factor of 3-4 slower than assumed [*Gilles et al.*, 1997].

$$I + O_3 \rightarrow IO + O_2 \tag{2.86}$$

$$ClO + IO \rightarrow I + OClO \quad (k = 5.1 \times 10^{-12} e^{280/T} \ cm^3 \ mol.^{-1} \ s^{-1}) \tag{2.87a}$$

$$\rightarrow I + ClOO \tag{2.87b}$$

$$\rightarrow ICl + O_2 \tag{2.87c}$$

$$\rightarrow I + Cl + O_2 \tag{2.87d}$$

$$\rightarrow OIO + Cl \tag{2.87e}$$

$$\rightarrow IOO + Cl \tag{2.87f}$$

$$\rightarrow IO_2Cl \tag{2.87g}$$
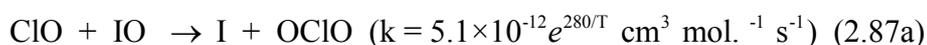
The cross reaction between BrO and IO is expected to generate Br + OIO as the major pathway [*Bedjanian et al.*, 1997b, 1998; *Lazlo et al.*, 1997; *Gilles et al.*, 1997]. Reactions of IO with HO_2, O, and NO_2 will also occur [*DeMore et al.*, 1997]:

$$IO + HO_2 \rightarrow HOI + O_2 \tag{2.88}$$

$$IO + O \rightarrow O_2 + I \tag{2.89}$$

$$IO + NO \rightarrow I + NO_2 \tag{2.90}$$

$$IO + h\upsilon \rightarrow I + O \tag{2.91}$$

Recent measurements and model studies imply that iodine chemistry does not dominate the ozone trends observed in the tropopause region, but could contribute to them.

2.4   BrO in the Atmosphere

2.4.1   Extra-Polar Boundary Layer

Observations of atmospheric BrO from many ground-based platforms have been demonstrated in several publications. At the salt pan regions of the Salar de Uyuni, Bolivia, and at mid-latitudes over the salt pan regions of the Dead Sea, Israel, ground-based DOAS measurements observed BrO mixing ratios of > 20 ppt and up to 176 ppt respectively which was correlated with low-boundary layer ozone mixing ratios [*Hönninger et al.,* 2004; *Hebestreit et al.,* 1999; *Matveev et al.,* 2001]. Significant amounts of BrO have also been observed at the Great Salt Lake region of the USA in the mid-latitude boundary layer [*Stutz et al.*, 2002]. Recently, ground-based measurements of BrO in the mid-latitude marine boundary layer were carried out using a MAX-DOAS instrument onboard a research shipping vessel [*Leser et al.,* 2003]. The highest significant individual measurement in BrO mixing ratios of 2.4 ± 2.1 ppt was reported. Typical levels in the marine lower troposphere were less than 1 - 3.6 ppt.

Disappointingly, satellite-based DOAS evaluations of BrO from GOME and SCIAMACHY (equipped with an even higher spatial resolution compared to GOME) see no clear signature of enhanced BrO in these mid-latitude hotspots of the Dead Sea and salt lakes regions over North America. This indicates that the high mixing ratios of BrO observed in the extra-polar boundary layer from ground-based platforms are probably restricted to a shallow layer close to the surface and hence do not constitute a large vertical column.

2.4.2 Ozone Depletion Events at Polar Sunrise – Bromine Explosion

Sudden boundary layer (BL) ozone depletion events were observed more than two decades ago at Barrow, Alaska (71°N, 157°W), [*Oltmans and Komhyr,* 1986] and at Alert, northern Canada (82.5°N, 62.3°W), [*Bottenheim et al.*, 1986; *Tuckermann et al.*, 1997; *Hönninger and Platt,* 2002] in late arctic winter/early spring. These low ozone events were correlated with elevated concentrations of filterable bromine (f-Br), giving the first indication that reactive halogen species are involved in the destruction of ozone [*Barrie et al.,* 1988, 1989]. Later the Polar Sunrise Experiment in 1992, led to the observation of up to 17 ppt BrO by long-path DOAS [*Hausmann and Platt*, 1994]. At Ny-Ålesund, spectroscopic results on BrO and ClO have been published by *Tuckermann et al.,* (1997). Simultaneous observations by ground-based zenith sky DOAS confirmed the existence of tropospheric BrO [*Wittrock et al.,* 1996]. Since then several studies have confirmed these observations also in Antarctica [*Wessel et al.,* 1998; *Kreher et al.,* 1996, 1997; *Frieß et al.,* 2004]. Huge 'clouds' (*Bromine Explosion Events*) of BrO enriched air masses over the polar sea ice of both hemispheres in polar springtime have also been impressively shown by satellite measurements of BrO vertical columns [*Richter et al.* 1998, 2001; *Wagner et al.* 1998]. These events of highly elevated BrO in polar regions, with mixing ratios of up to 30 ppt, have been always coincident with low levels of ozone in the polar boundary

layer, strongly suggesting that reactive bromine is responsible for its catalytic destruction. Enhanced BrO in the polar boundary layer associated with ozone destruction has also been detected over the Caspian Sea [*Wagner,* 1999].

2.4.3   Involvement with Atmospheric Mercury

Atmospheric mercury (Hg) is one out of a family of 'heavy metals', which exists in ambient air predominantly in the gaseous form. Its anthropogenic sources (some of which are fossil fuel combustion and waste incineration) outweight the natural sources. In ambient air, Hg exists predominantly in the gaseous elemental form and can undergo long-range atmospheric transport on continental and global scales [*Petersen et al.,* 1995; *Schroeder and Munthe*, 1998]. It was discovered that sometimes during months after polar sunrise, in the Arctic and Antarctic boundary layer total gaseous mercury (TGM) levels are often significantly depleted while mercury concentrations in the snow pack are concurrently increased [*Lu et al.,* 2001, *Ebinghaus et al.*, 2002; *Lindberg et al.,* 2002]. The possible explanation for these episodes was credited to photochemical oxidation of Hg^0 to Hg^{2+} resulting in particle-associated mercury (PM) and or reactive gaseous mercury (RGM). The reactions probably involve the same reactive bromine and chlorine compounds involved in tropospheric ozone destruction. An evaluation of trajectories at Ny-Ålesund for selected mercury depletion events and comparisons with BrO vertical column densities obtained from the GOME instrument indicates that air masses exhibiting low Hg^0 concentrations originate from areas with high BrO densities [*Sommar et al.,* 2004].

2.4.4   BrO in the Free Troposphere

There are indications that there are significant amounts of BrO in the free troposphere of the order of ~0.5–2 ppt, if uniform distribution over the entire troposphere is assumed [*Ferlemann et al.,* 1998; *Frieß et al.,* 1999; *McElroy et al.,* 1999; *Fitzenberger et al.,* 2000; *Richter et al.,* 2002; *Van Roozendael et al.,* 2002]. Comparison of GOME BrO vertical columns with models and measurements from balloon-borne and ground-based platforms [*Pundt et al.* 2000; *Fitzenberger et al.,* 2000; *Richter et al.,* 2002; *Wagner,* 1999, 2001; *Van Roozendael et al.,* 1999, 2001; *Schofield*, 2003] has led to the conclusion, that a significant tropospheric background of several ppt BrO must be present in the atmosphere at all latitudes.

2.4.5   BrO in the Stratosphere

In the lower stratosphere, bromine is photochemically released from its source gases (e.g. CH_3Br, CH_2Br_2, $CBrClF_2$) which presently amounts up to 18-20 ppt in total bromine [e.g. *Schauffler et al.,* 1998; *Wamsley et al.,* 1998; *Pfeilsticker et al.,* 2000], however the largest single contributor of stratospheric bromine is CH_3Br which has a tropospheric mixing ratio of ~9.8±0.6 ppt [*Lobert et al.,* 1995; *Penkett et al.,* 1995]. After release bromine is present in the inorganic form BrO, Br, Br_2, BrCl, $BrONO_2$, HOBr, and HBr (known collectively as Br_y). The main inorganic bromine species in the stratosphere during daytime is BrO, which could represent about 30-70% of the total Br_y during daytime [*Lary,* 1996; *Sinnhuber et al.,* 2002]. The main destruction pathway or sink for BrO in the sunlit lower stratosphere is by photolysis into subsequent atomic constituents [*Lary,* 1996]. At twilight, a dominant loss process for BrO is the termolecular reaction with NO_2 to form the reservoir specie, $BrONO_2$. Since the variation of stratospheric BrO columns is found to be anticorrelated with that of NO_2, measured by the same instruments, it has been suggested that this reaction largely controls the BrO amounts in the stratosphere [e.g. *Fish et al.,* 1997; *Richter et al.,* 1999]. The latitudinal and seasonal changes of BrO concentrations are largely controlled by the vertical transport of total inorganic bromine and to a smaller extent by photochemistry [e.g. *Pundt et al.,* 2002]. Spectroscopic measurements of stratospheric BrO columns at different latitudes and season from a combination of several ground-based, balloon- and space-borne platforms have been made and the results compared to modeled BrO columns [e.g. *Harder et al.,* 1998 2000; *Ferlemann et al.,* 1998; *Pundt et al.,* 2002; *Schofield et al.,* 2004; *Sinnhuber et al., 2002, 2005; Aliwell et al.,* 2002; *Van Roozendael et al.,* 2002]. For example, significant BrO amounts were observed at all latitudes and seasons, with peak concentration altitude varying from 15 km in the winter vortex to ~22 km in the tropics by balloon-borne spectroscopy [*Pundt et al.,* 2002]. BrO measurements from SCIAMACHY limb and nadir observations coupled with modeled BrO profiles provided for the first time a global view of the BrO loading in the stratosphere [*Sinnhuber et al.,* 2005]. Ground-based twilight measurements report significant BrO column amounts from middle to high latitudes in both hemispheres with, significant seasonal and latitudinal variations. Typically, BrO column densities are found to be larger in winter at high latitudes compared to the mid-latitude summer [*Arpag et al.,* 1994; *Aliwell et al.,* 1997; *Fish et al.,* 1997; *Richter et al.,* 1999; *Kreher et al.,* 1997; *Otten et al.,* 1998; *Sinnhuber et al.,* 2002]. At the opposite, BrO mixing ratios are smallest during permanent polar day and at mid-latitudes in summer where the NO_2 concentration is the largest [e.g. *Pundt et al.,* 2002]. Global noontime observations of BrO by GOME reveal similar latitudinal and seasonal variations, although the BrO column amounts includes a tropospheric contribution, which dominates the signal in polar regions in spring [*Richter et al.,* 1998, 2002; *Wagner and Platt;* 1998; *Wagner,* 1999].

Chapter 3

The Space-borne Instruments GOME and SCIAMACHY

3.1 The Global Ozone Monitoring Experiment (GOME)

GOME is a passive imaging spectrometer that was launched on the 21st of April 1995 aboard the second European Remote Sensing satellite (ERS-2) by the European Space Agency (ESA). The launch marked the beginning of a long-term European effort to monitor atmospheric O_3 and NO_2 as well as important trace gases which have comparatively weak atmospheric absorptions amongst which are as BrO, HCHO, SO_2, and OClO [*ESA*, 1995; *Burrows et al.,* 1999; *Richter et al.,* 1998; *Wagner et al.,* 1998] in the earth's atmosphere. GOME measures the earthshine radiance and the solar irradiance in the UV/Visible spectral range, 240-790 nm, at a moderate spectral resolution of 0.2-0.4 nm. The large spectral range of GOME combined with the high spectral resolution permits the application of the DOAS algorithm to the retrieval of column amounts of many trace gases [*Platt,* 1994, and references therein]. Onboard the ERS-2 are five other instruments namely the Active Microwave Instrument (AMI); the Radar Altimeter (RA); the Along-Track Scanning Radiometer (ATSR), which consists of an InfraRed Radiometer (IRR) and a MicroWave Sounder (MWS) and the Precise Range and Range Rate Equipment (PRARE). The ERS-2 moves in a near-polar sun-synchronous orbit at a mean altitude of about 795 km.

3.1.1 Instrumental Layout of GOME

The schematics of the spectrometer optics are shown in figure 3.1a and 3.1b below. The instrument weighs about 30 kg with dimensions of about $60 \times 30 \times 20$ cm^3, operating at a total power consumption of about 30 W [*ESA*, 1995]. GOME collects light arriving from the sun-illuminated atmosphere and light reflected from the surface and decomposes it into its spectral components. In order to provide both the spectral coverage from 240 - 790 nm and a good spectral resolution of 0.2 - 0.4 nm at high straylight rejection, this decomposition is done in two steps: first by a quartz pre-disperser prism, from which the light is split into four different channels.
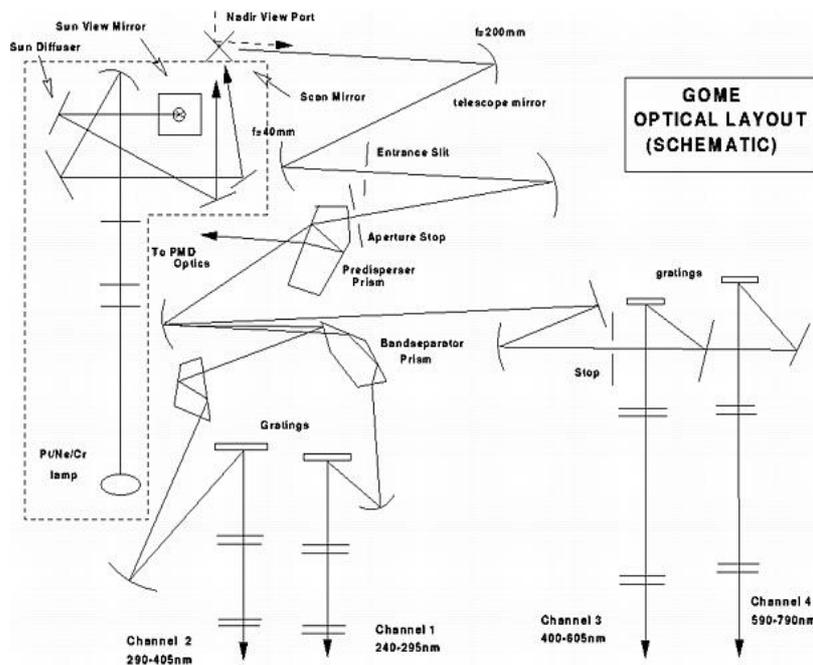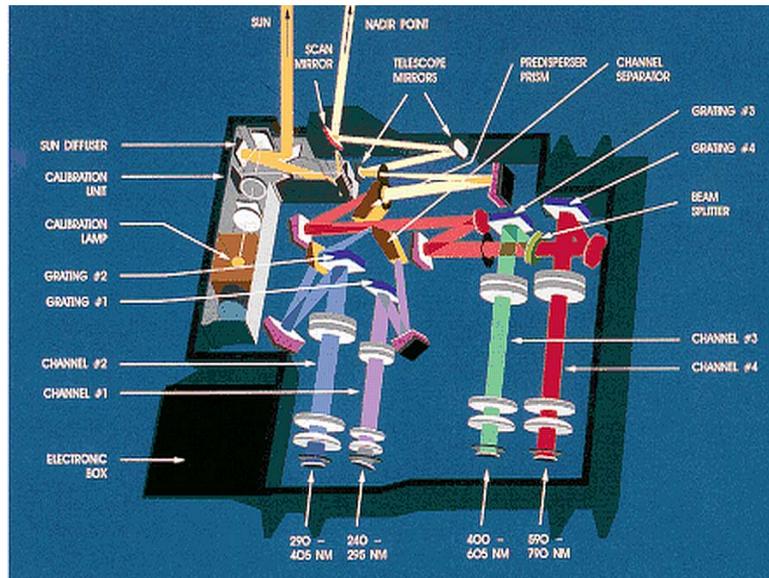
Figure 3.1: (Top) Instrumental set-up of GOME [Courtesy, ESA] and Fig 3.1b (Bottom) Schematics of GOME Optics [*Weber et al.* 1998]. The GOME instrument is a four-channel spectrometer. Adjacent to the spectrometer is a calibration unit housing a Pt/Cr/Ne hollow cathode discharge lamp for wavelength calibration and the fore optics for solar viewing. Not shown is an additional mirror, which directs the lamplight to the solar diffuser plate for diffuser reflectivity measurements.

Part of the light which reaches the pre-disperser prism is branched out and recorded with three broadband polarization monitoring devices (PMDs), which approximately cover the spectral range in channels 2 (300-400 nm), 3 (400-600 nm), and 4 (600-800 nm), respectively. The PMDs measure the amount of light at an instrument defined polarization angle. Each of the channels possesses a grating as second dispersing element, and a 1024 pixel silicon array detector. The integration times on the chip can be multiples of 93.75 msec, with 1.5 sec (this is the integration time including co-adding) for the visible and 12 sec for the UV being the default values. The entire instrument can be broken down into the following functional blocks:

- The spectrometer
- The 4 Focal Plane Assemblies (FPA's)
- The calibration unit
- The scan unit with the scan mechanism and the scan unit electronics assembly
- The Polarisation Measurement Device (PMD)
- The Digital Data Handling Unit (DDHU)
- The optical bench structure
- The thermal control hardware

The light reflected off the scan mirror is focussed by an anamorphic telescope such that the shape of the focus matches the entrance slit of the spectrometer, with dimension 10 mm x 100 mm. After the slit, an off-axis parabolic mirror collimates the light.

The incident light on the quartz pre-disperser prism causes a moderately dispersed wavelength beam. Another prism acts as channel separator: the upper edge of this prism reaches into the wavelength dispersed beam, letting pass the longer wavelengths, reflecting the wavelength range 290 - 405 nm into channel-2 by means of a dielectric reflecting coating, and guiding internally the wavelength range 240 - 295 into the channel 1. The unaffected wavelength range 405 - 790 nm is then split up by a dichroic beam splitter into the channels 3 (400 - 605 nm) and 4 (590 - 790 nm). Each individual channel consist of an off-axis parabola, a grating, and an objective with f-numbers 2 (channel 1 and 2) and 3 (channel 3 and 4), respectively, finally focussing the light onto the detectors, contained in their respective Focal Plane Assemblies.

3.1.2   Viewing mode, Spatial coverage and Resolution

GOME is a nadir-viewing spectrometer that provides continuous spectral measurements of backscattered earth radiances and solar irradiances in the UV/visible wavelength range (*see Figure 3.2 below*).
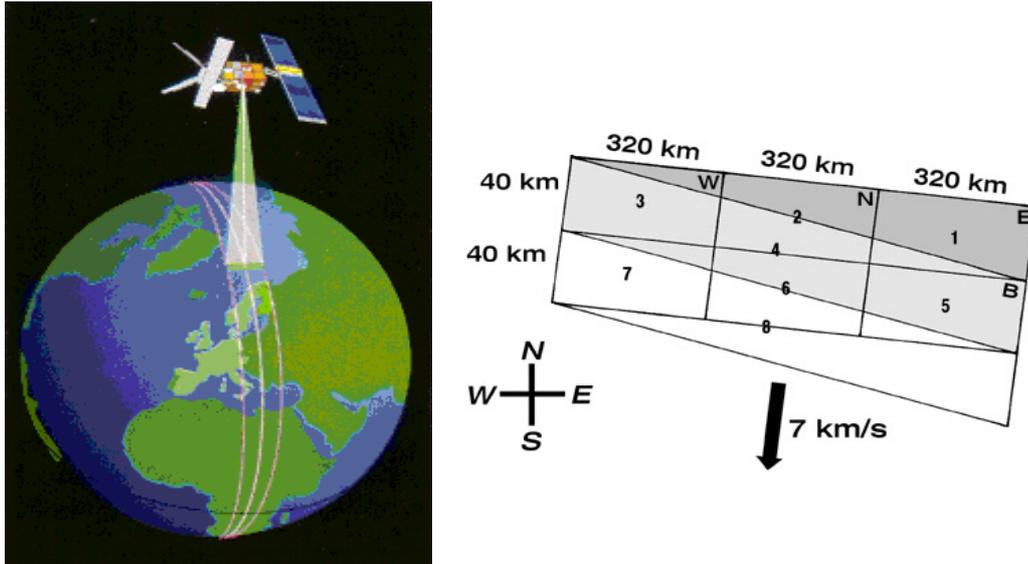
Figure 3.2. An artist's impression of nadir-viewing GOME (right) and GOME scan pattern (left). GOME scans the Earth normal to flight direction with the help of a mirror. During the 4.5 sec forward movement of the mirror, three-ground pixels 40 x 320 km^2 in size are generated. The back motion of the mirror occurs at threefold speed (Images courtesy ESA).

It scans the earth's surface at an angular range of ± 31°, corresponding to a cross track swath width of 960 km. In the event of every scan, three standard ground pixels are mapped out with a spatial resolution of 320 km East-to-West and 40 km North-to-South subsequently followed by a back scan ground scene at 960×40 km^2 each at 1.5 seconds integration time. Besides the Standard Swath Mode (SSM), GOME also operates three days a month (Since the end of July 1997) in the Narrow Swath Mode (NSM) corresponding to a spatial extent of 80×40 km^2 at a reduced scan angle of ± 8.7°. In the SSM, GOME achieves global coverage every three days at a descending node with an equator crossing time of 10:30 local time and after approximately one day at 65° with a repeat cycle of about 35 days [*Bednarz,* 1995]. The speed of the satellite along its orbit is ~ 7 kms^{-1}. Below (in tabularized form) are the spectral properties of the GOME instrument.

Channel	Wavelength (nm)	Integration Time (sec)	Spectral Resolution (nm)	Pixel Size (nm)
1A	237-283	12	0.20	0.11
1B	283-316	1.5	0.20	0.11
2	311-405	1.5	0.17	0.12
3	405-611	1.5	0.29	0.30
4	595-793	1.5	0.33	0.35

Table 3.1. GOME spectral range, wavelength interval, and resolution coverage for the four different channels.

3.1.3   Instrumental Problems and Limitations

Following the availability of the GOME spectra for analysis it soon became obvious that application of independent DOAS algorithms (developed by several groups from different research institutes) to the GOME spectra to derive slant columns of trace gas species indicated inaccuracies through relatively large residuals obtained from the DOAS procedure. The residuals were observed to exhibit poorer signal-to-noise (SNR) ratio when the solar irradiance was used as a background to derive absolute slant columns. The errors were observed to be systematic and seem to become stable over relatively longer time series [*Richter and Wagner*, 2001]. GOME irradiance measurements are done over a diffuser plate and in the flight direction. Hence the solar measurements suffer a systematic variation in the azimuth angle between the diffuser and the sun over one year as a result of the wavelength-dependence of diffuser reflectivity (which introduces the residuals) and the solar measurements affected by a Doppler shift in the wavelength registration. Use of an Earthshine spectrum as background largely improved the residuals of the fit but a problem arises on how to account for the uncertainties of the unknown absorption in the background spectra. Several factors have been identified to contribute to the poorer-than-expected residuals:

- Uncertainties as a result of slight errors in the Ring spectrum.

- Variations in the effective slit function resulting from non-uniformity in illumination of ground pixels.

- Undersampling of the spectra in relation to the Doppler shift of the solar irradiance.

Strong Etalon structures due to ice formation on the detectors of the instrument from the residual water vapour in the satellite also interfere with the GOME spectra resulting in structures of amplitudes comparable to those of ozone in the Chappuis bands; hence no reliable ozone retrieval can be done in the visible spectral range.

The Southern Atlantic Anomaly (SAA): Over the Southern Atlantic Ocean off the coast of Brazil, a part of the inner Van Allen belt dips down ~ 200 km into the upper region of the atmosphere. This region, known as the South Atlantic Anomaly affects measurements subjecting them to large errors and high-frequency structures. In practice, measurements made by GOME over the region of the SAA are avoided.

Limited GOME data availability: On June 22 2003, the ERS-2 tape recorder became permanently unavailable due to a technical failure. The ERS-2 tape recorders were used to record the ERS-2 Low Rate mission globally. After eight years of continuous acquisition, this service was discontinued. The ERS-2 Low Rate mission is continued within the visibility of ESA ground stations over Europe, North Atlantic, the Arctic and western North America.

3.2 The SCIAMACHY Instrument

The SCIAMACHY (SCanning Imaging Absorption spectroMeter for Atmospheric CHartographY) instrument [*Burrows et al.,* 1995; *Bovensmann et al.,* 1999] is part of the payload of ESA's Environmental Satellite (ENVISAT), which was launched into a sun-synchronous orbit on the 1st March 2002. It is a UV/visible/NIR (240-2380 nm) grating spectrometer that observes the upwelling radiance from the earth's atmosphere/surface and the extraterrestrial solar irradiance. The SCIAMACHY instrument is designed to retrieve the tropospheric and stratospheric abundances of various atmospheric trace gases (e.g. O_3, O_4, NO_2, BrO, CH_4, CO, CO_2, H_2O, OClO, SO_2, and HCHO) and aerosols and their distribution as well as cloud cover and cloud top height. The absorption, reflection and scattering characteristics of the atmosphere are determined by comparing the extraterrestrial solar irradiance with the earthshine radiance observed in the different viewing geometries.

3.2.1 Optical Layout of the Instrument

The diagram below (Figure 3.4) illustrates the SCIAMACHY optical layout which consists of a mirror system, a telescope, a spectrometer, several detectors, gratings and both thermal and electronic subsystems.
Incoming radiation enters the instrument through one of three ports:

- The earthshine radiance is directed via a scanning unit consisting of the Azimuth and Elevation Scan Mirrors (ASM and ESM) into a telescope mirror, which then focuses the light onto the (0.190×9.6 mm^2) entrance slit of the spectrometer. The Elevation Scanning Mirror (ESM) is used during nadir measurements.

- For the limb and solar/lunar occultation measurements, incoming radiation is reflected via the limb (Elevation) mirror to the nadir (Azimuth) mirror, which focuses the beam onto the entrance slit of the spectrometer. The ASM mechanism is used to control the azimuth of the Instantaneous Field Of View (IFOV) when performing limb/occultation measurements.

- Line lamps and solar radiation, used for internal and subsolar calibration measurements, are directed via the nadir mirror into the telescope.
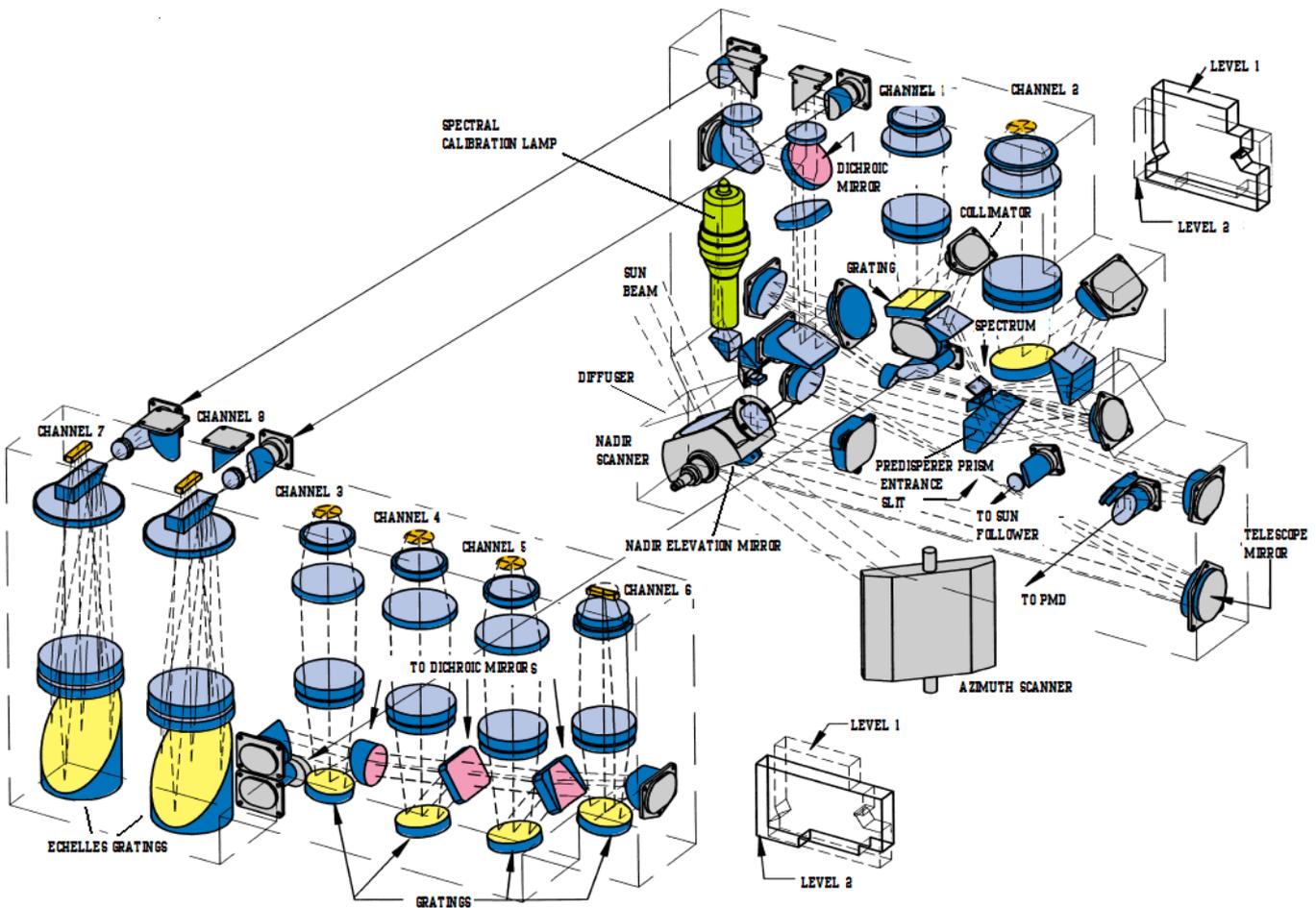
Figure 3.4: SCIAMACHY Optical Layout emphasizing an array of light paths through the instrument *(Courtesy Astrium, GmbH)*.

To enhance the durability of the SCIAMACHY instrument, only the Scan mirrors are movable (all other parts are fixed). Because of the large differences in order of magnitude between the measured earthshine radiance and the solar irradiance over the same spectral range, the SCIAMACHY spectrometer suppresses straylights within the instrument through a combination of predispersing prisms and gratings. Light from the entrance slit is collimated and directed onto the predispersing prism.

The main beam of light leaving the predispersing prisms forms a spectrum in the middle of the instrument. Reflective optics splits the spectrum into four different parts:

- Light of shorter wavelengths from the spectrum is directed into channels 1 (240-314 nm) and 2 (309 – 405 nm). *Tables 3.2 (below) elaborate on the characteristics of the separate channels.*

- The main part of the light in the spectrum between (405-1750 nm) passes without reflection into channels 3 to 6.

- The infrared component of spectrum of the spectrum is reflected towards channels 7 and 8.

Light reflected off the spectrometer slit is also directed to a four-quadrant sensor known as the Sun Follower (SF), which controls the scan mirrors in the sun and moon occultation mode and evaluates the images reflected from the blades of the slit. Dichroic mirrors are used to select the wavelength ranges for channels 3-8. Each channel comprises a grating, transmission optics and a diode array detector. The grating further disperses the light, which is then focused onto eight linear 1024-pixel detector arrays. The diode arrays are cooled to reduce detector noise and dark current. The operating temperatures for the eight separate channels are listed in table 3.2. The entire instrument is cooled to about 235 K to minimize infrared emissions that influences the detectors of channels 6-8. The SCIAMACHY instrument has radiometric and wavelength accuracy typically better than 4% and 0.01 nm respectively. Power consumption is about 155 W and the instrument weighs about 215 kg.

3.2.2   Viewing Geometries, Spatial coverage and Resolution

SCIAMACHY measurements are performed in three different viewing modes: nadir, limb and solar/lunar occultation (*see Fig 3.5 below*) from an altitude of about 800 km. In nadir mode, the atmospheric volume beneath the spacecraft is observed and the nadir mirror scans an area on ground corresponding to a maximum swath width of 30 km along track by 960 km across track. The edge of the swath width has a Line-Of-Sight (LOS) varying from 0° to a maximum of about 30.9°. Typical footprints of 30 km (along track) × 60 km (across track) are obtained for nadir observations, but this can be up to 30 km × 30 km depending on scan speed and integration time.
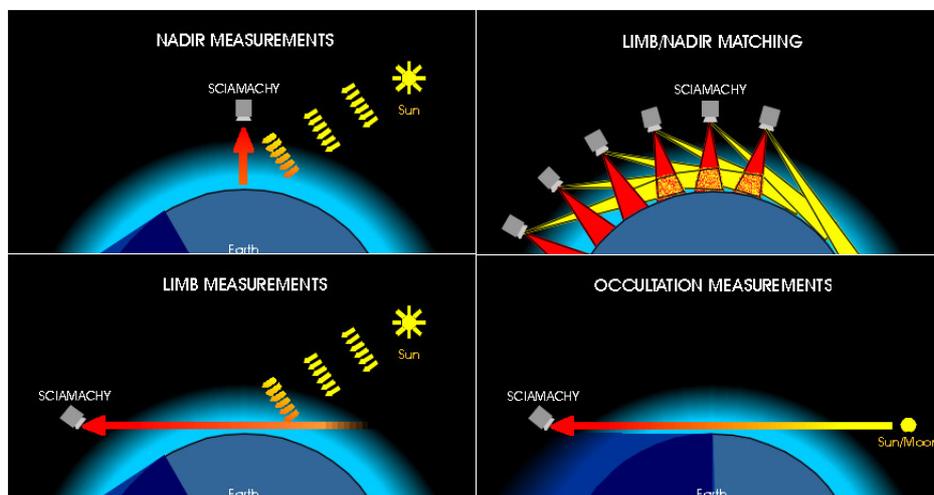
Figure 3.5: SCIAMACHY measurement modes in nadir, limb and occultation geometry.(available from http://www.iup.physik.uni-bremen.de/sciamachy/)

In the limb mode, the spectrometer slit is projected parallel to the horizon in-flight direction by a combination of the limb and the nadir mirror. In this mode, both elevation and azimuth mirrors are used to record atmospheric spectra; the atmosphere is observed tangential to the earth's surface. The limb mirror scans the atmosphere through different tangent heights from 0 to 100 km in horizontal (azimuth) direction; whereas, appropriate movement of the nadir mirror results in a vertical (elevation) scan direction. A typical limb scan cycle comprises 34 horizontal scans (azimuth) at different tangent heights (elevation), starting 3 km below the horizon. After each horizontal scan, which has duration of about 1.5 seconds, a 3 km-step in elevation is made by the elevation mirror. No measurements are made during this repositioning, which takes about 150 ms.

Each horizontal scan of the atmosphere in limb mode covers 960 km (across track). The vertical resolution is about 3 km but this is dependent on the geometrical field of view, the pointing stability of the instrument and the multiple scattering of light in the atmosphere. The individual spatial resolution within a 960 km swath width in the horizontal direction across track is typically 240 km. This is determined by the integration time, which is typically about 0.375 seconds.

Occultation measurements are performed using the elevation and azimuth scan mirrors in a manner similar to the limb mode, but with the sun or moon in the full view of the instrument. SCIAMACHY selects a target, the sun or the moon and tracks it as soon as it comes above the horizon and until the line of sight reaches a maximum tangent height of 100 km. Spectra of the source radiation transmitted through the atmosphere are recorded during the complete sequence.

A novel feature of the SCIAMACHY instrument is ability to observe the same atmospheric volume first in limb and thereafter in nadir modes within a time ~ 7 minutes apart. This feature, called limb-nadir-matching, enables in principle the

separation of the tropospheric trace gas amounts from the total column for a variety of atmospheric trace gases amongst which are (O_3, BrO, NO_2, CH_4, SO_2 and H_2O).

Channel	Spectral range (nm)	Spectral resolution (nm)	Operating temperature (K)	PMD	Spectral range (nm)
1	240 - 314	0.24	185 - 215	1	310-377
2	309 - 405	0.26	185 - 215	2	450 - 525
3	394 - 620	0.44	215 - 235	3	617 - 705
4	604 - 805	0.48	215 - 235	4	805 - 900
5	785 - 1050	0.54	225 - 235	5	1508 - 1645
6	1000 - 1750	1.48	190 - 210	6	2265 - 2380
7	1940 - 2040	0.22	130 - 160	45°	802 - 905
8	2265 - 2380	0.26	130 - 160		

Table 3.2. Detector and PMD Characteristics of the SCIAMACHY instrument highlighting the spectral range and resolution of the separate channels and the operating temperatures.

Geometry	IFOV		
Nadir	0.045 / 1.8	+/- 0.003 ° / +/- 0.200 °	across track / along track
Limb	0.045 / 1.8	+/- 0.003 ° / +/- 0.200 °	in elevation / in azimuth
Solar Occultation	0.045 / 0.72	+/- 0.003 ° / +/- 0.020 °	in elevation / in azimuth
Moon Occultation	0.045 / 1.8	+/- 0.003 ° / +/- 0.200 °	in elevation / in azimuth

Table 3.3. Defines fields of view for the different viewing geometries for SCIAMACHY. The IFOV defines the instantaneous solid angle from which spectral radiance is detected. The size of the IFOV is defined by the contour, where the energy is 50% of the maximum energy inside the IFOV.

3.3 Data Products

SCIAMACHY data products are divided into Level 1B, Level 2 (NRT, NRT meteo and off-line products). Table 3.4 gives an overview of SCIAMACHY data products. The product generation has been split between Near Real Time (NRT) processing (products available three hours after data acquisition) and off-line processing (produced using improved ancillary data that becomes available after spectrum acquisition, e.g., analysed temperature and pressure fields).

	Nadir			Limb		
	UV/Vis	IR	UV/Vis/IR	UV/Vis	IR	UV/Vis/IR
NRT	O_3^*, NO_2, SO_2^*, $OClO^*$, H_2CO^*	H_2O, CO, N_2O, CH_4	Clouds, Aerosols			
Off-Line	O_3, NO_2, BrO^{**}, SO_2^*, $OClO^*$, H_2CO^*, UV-index**	H_2O, CO^{**}, CO_2, N_2O^{**}, CH_4, P, T	Clouds, Aerosols	O_3, NO_2, BrO^{**}	H_2O, CO^{**}, O_2, N_2O^{**}, CH_4, P, T	Aerosols

Table 3.4: Near Real Time (NRT) and Off-Line SCIAMACHY level 2 operational products for the Nadir and Limb viewing modes covering SCIAMACHY's entire spectral range.

3.4 Instrumental Problems and Limitation

Currently, several problems have been identified in the SCIAMACHY measurements. Some of which are relevant to this study includes:

- Presence of strong polarisation features in Channels 2 and 3 interfere significantly with retrievals of column amounts of relevant trace gases (e.g. BrO, HCHO and O_3) in these wavelength regions.

- Reduced spatial coverage in SCIAMACHY data compared to GOME measurements. Half the data sets are devoted to limb measurements but lost for nadir observations.

- Some problems with data dissemination but improvements are evident from day-to-day.

- Problems in radiometric calibration have been identified in Lv-1 data products

- Early results indicate a solar irradiance offset of 10-15% when compared to reference data.

- Presence of Etalon structures as a result of ice formation encountered in Channels 7 and 8.

- Pointing problems associated with SCIAMACHY limb measurements.

- Cloud detection and characterisation.

---

*Observed under special conditions (Volcanic eruptions, Ozone hole, heavy tropospheric pollution.
** Recommended by the Science Advisory Group.

Chapter 4

Radiative Transfer and Absorption Spectroscopy

Remote sensing measurements of atmospheric species from space using extraterrestrial light sources require detailed understanding of the absorption, reflection and scattering properties of the many trace gases and particles/aerosols in the earth's atmosphere. Therefore, accurate determination of the relevant parameters such as, for example, the scattering properties of the ground surface (or albedo) and clouds is key to the retrieval of atmospheric constituents using Differential Optical (UV/visible) Optical Absorption Spectroscopy (DOAS). Radiative transfer calculations is a valuable tool used for many applications such as the retrieval of atmospheric constituents, the calculation of air mass factors and vertical columns of atmospheric trace gases and cloud top height retrieval from remote radiance measurements.

4.1 SCIAMACHY Radiance and Solar Irradiance from Nadir Geometry in Channel 2.

The figures below show the spectrum of the earthshine radiance and solar irradiance retrieved from the channel 2 UV/visible wavelength range of SCIAMACHY in nadir mode for the 25th of September 2003. These have been extracted from the available lv-1 data files, applying only dark current and wavelength (spectral) calibration options. Unfortunately, other known calibration options such as the Radiometric, Polarisation correction and Etalon calibration options have not been applied to the retrieved spectra due to these calibration options not yet functioning correctly.
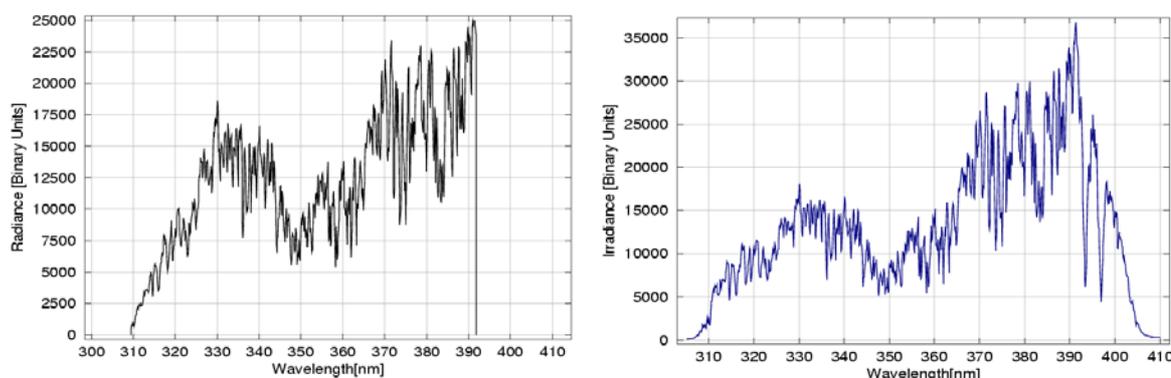
Figure 4.1. SCIAMACHY UV/visible radiance and solar irradiance obtained from nadir-viewing geometry in channel 2 taken on the 25th September 2003. The radiance spectrum (taken at SZA=33.45°, Lat. =23.48°, Long. =68.45°and Time = 05:42:56.46) contains spectral features of known trace gas absorptions in the earth's atmosphere while the irradiance spectrum is in principle free of such absorption. Note the strong polarisation structures prominent around 350 nm.

4.2 The Differential Optical Absorption Spectroscopy (DOAS) method

The DOAS method [*Platt*, 1994] is an open-path retrieval technique based on the identification and quantification of atmospheric trace gases by their unique absorption spectra in the UV/visible spectral range. In recent years, the method has been used extensively for zenith-sky absorption measurements of tropospheric and stratospheric constituents from the ground. Recent applications of DOAS to the retrieval of trace gases from space-borne platforms have been successfully demonstrated using GOME measurements for O_3, NO_2, BrO, OClO, SO_2, O_4 and H_2CO [e.g. *Burrows et al.,* 1999; *Richter et al.,* 1998, 2005; *Eisinger and Burrows*, 1998; *Wagner and Platt*, 1998, 2002; *van Roozendael* et al., 1994]. A brief overview of the DOAS concept is given as follows:

Given the measured earthshine radiance $I(\lambda)$ and the solar irradiance $I_0(\lambda)$, both measured by GOME or SCIAMACHY, and the absorption cross-section of the relevant atmospheric trace gas which is temperature-, pressure- and wavelength-dependent (i.e. $\sigma(\lambda) \equiv \sigma(\lambda, p(s), T(s))$), the basic equation of absorption spectroscopy describing pure absorption for an ensemble of absorbers, *j*, in a homogeneous media is given by the Beer-Lambert equation:

$$I(\lambda) = I_0(\lambda) \exp\left\{-\sum_{i=1}^{j}\left(\sigma_i(\lambda).\int_s \rho_i(s)ds\right)\right\} \qquad (4.1)$$

Where the slant column density, SCD_i, is by definition the particle number density, ρ_i, integrated along the light path, *s*, and strongly depends on θ i.e. the solar zenith angle (SZA).

$$SCD_i(\lambda, \theta) = \int_s \rho_i(s)ds \qquad (4.2)$$

The cross-section for individual species, σ_i, can be separated into two components; one that slowly varies with wavelength, $\sigma_i^s(\lambda)$, and another rapidly varying part, $\sigma_i'(\lambda)$. The rapidly varying cross-section is also called the 'differential cross-section'. Hence, the total cross-section, $\sigma_i(\lambda)$, is by definition the sum of the two:

$$\sigma_i(\lambda) = \sigma_i^s(\lambda) + \sigma_i'(\lambda) \qquad (4.3)$$

The slowly varying component describes the general slope, and the differential cross-section corresponds to the difference between the slope and the total cross-section.

In real atmospheric conditions, in addition to the absorption, Rayleigh and Mie scattering also contribute to the radiation extinction as a result of air molecules and aerosols scattering light away from the line of sight. Thus, Rayleigh, Mie and Rotational Raman scattering are taken into account. The Raman scattering is responsible for the so-called 'Ring Effect' [*Grainger and Ring*, 1962]. Adding these contributions to equation 4.1 results in:

$$I(\lambda) = I_0(\lambda) \exp\left\{ -\left[\sum_{i=1}^{j} \left(\sigma_i(\lambda).\int_s \rho_i(s)ds \right) + \int_s \int \varepsilon^R(\lambda) + \int_s \varepsilon^M(\lambda) + \sigma_{ring}(\lambda)\int_s \rho_{ring}(s) \right] \right\} \quad (4.4)$$

$$I(\lambda) = I_0(\lambda) \exp\left\{ -\int_s \left[\sum_{i=1}^{j} \sigma_i(\lambda)\rho_i(s) + \sigma_R(\lambda)\rho_R(s) + \sigma_M(\lambda)\rho_M(s) + \sigma_{ring}(\lambda).\rho_{ring}(s) \right] \right\} \quad (4.5)$$

Where $\varepsilon^R(\lambda)$ is the Rayleigh extinction coefficient, which is the product of the Rayleigh cross-section, $\sigma^R(\lambda)$ and the number density of air, $\rho_R(s)$. Similarly, the Mie extinction coefficient, $\varepsilon^M(\lambda)$, corresponds to $\sigma^M(\lambda).\rho_M(s)$. In equation (4.5), the Ring-Effect is approximated and included as an additional absorber in the fitting procedure [*Solomon et al.*, 1987]. Simplification and approximation of equation (4.5) yields in terms of slant column densities:

$$I(\lambda) = I_0(\lambda) \exp\left\{ -\sum_{i=1}^{j} \sigma_i(\lambda)SCD_i - \sigma_R(\lambda)SCD_R - \sigma_M(\lambda)SCD_M - \sigma_{ring}(\lambda)SCD_{ring} \right\} \quad (4.6)$$

In practice, the separation of the differential cross-section $\sigma_i'(\lambda)$, in equation (4.3) is achieved by subtraction of a fitted polynomial of low order, which also compensates the effects of Mie and Raleigh scattering. Hence from equation (4.6):

$$\ln I(\lambda) - \ln I_0(\lambda) = \sum_p [a_p.\lambda^p] - \sum_{i=1}^{j+1} \sigma_i'(\lambda).SCD_i \quad (4.7)$$

where a_p are the polynomial coefficients, p, the index of the order of the polynomial, and SCD_i are the slant column densities of the absorbers and $\sigma_j = \sigma_{Ring}$.

For satellite-based instruments, an appropriate reference spectrum would be an extraterrestrial solar spectrum, $I_0(\lambda)$, which is free of background absorption, while the earthshine spectrum, $I(\lambda)$ contains the absorption signatures of the known trace gases in the atmosphere. The conversion from slant columns for each trace gas to vertical columns requires a suitable airmass factor $AMF_i(\Theta, \lambda)$ for each trace gas:

$$VCD_i = \frac{SCD_i(\lambda, \Theta)}{AMF_i(\lambda, \Theta)} \quad (4.8)$$

The AMF describes the enhancement of the absorption due to the slant path viewing geometry and the solar elevation. The AMFs are calculated from a radiative transfer model (RTM), which requires trace gas profiles of absorber as part of the input and simulates the light path through the atmosphere.

4.3   The Radiative Transfer Model SCIATRAN

The radiative transfer model SCIATRAN (formerly GOMETRAN) [*V. Rozanov et al.,* 1997, 1998; *A. Rozanov et al.,* 2000, 2001, 2002; *Kurosu et al.,* 1997] computes a numerical solution of the radiative transfer equation (RTM) in the atmosphere. In a plane-parallel atmosphere that absorbs and scatters radiant energy, the radiative transfer for the diffuse radiance field ($I^{\pm}$) may be written as a two-coupled integro-differential equation:

$$\mu\frac{dI^+(\mu,\varphi)}{dz} = -\alpha I^+(\mu,\varphi) + \frac{b}{4\pi}\int_0^{2\pi} d\varphi'\int_0^1 p(\mu,\mu',\varphi,\varphi')I^+(\mu',\varphi')d\mu'$$

$$+\frac{b}{4\pi}\int_0^{2\pi} d\varphi'\int_0^1 p(\mu,-\mu',\varphi,\varphi')I^-(\mu',\varphi')d\mu'$$

$$+\frac{b}{4\pi}AF\mu_0 e^{-\frac{\tau_0}{\mu_0}}\int_0^{2\pi} d\varphi'\int_0^1 p(\mu,\mu',\varphi,\varphi')e^{-\frac{\tau_0-\tau}{\mu'}}d\mu' \qquad (4.9)$$

$$+\frac{bF}{4}e^{-\frac{\tau}{\mu_0}}p(\mu,-\mu_0,\varphi,\varphi_0)$$

and

$$-\mu\frac{dI^-(\mu,\varphi)}{dz} = -\alpha I^-(\mu,\varphi) + \frac{b}{4\pi}\int_0^{2\pi} d\varphi'\int_0^1 p(-\mu,\mu',\varphi,\varphi')I^+(\mu',\varphi')d\mu'$$

$$+\frac{b}{4\pi}\int_0^{2\pi} d\varphi'\int_0^1 p(-\mu,-\mu',\varphi,\varphi')I^-(\mu',\varphi')d\mu'$$

$$+\frac{b}{4\pi}AF\mu_0 e^{-\frac{\tau_0}{\mu_0}}\int_0^{2\pi} d\varphi'\int_0^1 p(-\mu,\mu',\varphi,\varphi')e^{-\frac{\tau_0-\tau}{\mu'}}d\mu' \qquad (4.10)$$

$$+\frac{b}{4\pi}e^{-\frac{\tau}{\mu_0}}p(-\mu,-\mu_0,\varphi,\varphi_0)$$

Where I^+ and I^- are the radiance fields at the top of the atmosphere for the upward and downward components in the direction $(-\mu, \varphi)$ and (μ, φ), respectively. μ and μ' are cosines of the zenith angle (also called the polar angle, θ); α represents the total extinction coefficient; φ_0, φ and φ' are the azimuth angles; b is the total scattering coefficient; $p(\mu, \mu', \varphi, \varphi')$ is the total scattering phase function; πF is the (spectral) solar flux or solar (spectral) irradiance [energy per time interval per unit area normal to the direction of propagation and per unit bandwidth], usually in [*photons/s/nm/cm²*]; τ is the total optical thickness of the atmosphere.
The last two terms on the right hand side of the equations (4.9) and (4.10) describe (I) Photons that are scattered for the first time in the atmosphere at height z after reflection at the surface and

(II) Photons that are scattered for the first time in the atmosphere at height z but without surface-reflection.

Amongst other inputs implemented in SCIATRAN are:

- the incorporation of the surface boundary conditions for direct and diffuse radiance which takes into account Lamberts laws of reflection (an alternative exists to use an arbitrary bi-directional scattering distribution function (BSDF))
- the discretisation of the RTE
- Implementation of a pseudospherical approximation that includes single-scattering treated in full spherical approximation and multiple-scattering treated in a plane parallel approximation

Essential parameters relevant to the determination and quantification of constituents that are of import in atmospheric physics and chemistry such as the surface albedo, A, of the reflecting surface, aerosol scenarios, simulated (but realistic) vertical profiles of the different trace gases for the calculation of e.g. airmass factors. Detailed information about the algorithms and implementation of SCIATRAN can be found at the IUP web page: http://www.iup.physik.uni-bremen.de/sciatran/instructions.html

4.4 Airmass Factors (AMF)

From the DOAS analysis of spectra obtained from measurements by a satellite-based instrument, the slant column densities (SCDs) of the absorbing molecules, i.e. the integrated concentration of the trace gases along the light path from the point of observation to the instrument are directly determined. But since the SCDs are strongly dependent on the viewing geometry (i.e. the SZA), it is necessary to convert them into their respective Vertical Column Densities (VCDs), which by definition is the vertically integrated concentration of the trace gas under consideration from the point of observation to the top of the atmosphere. This conversion is realized by dividing the SCDs by the so-called AMFs [*Solomon et al.*, 1987b]:

$$AMF = \frac{SCD}{VCD}; \quad hence \quad VCD = \frac{SCD}{AMF} \tag{4.11}$$

The AMFs are determined from a RTM, SCIATRAN, which takes into account the simulated atmospheric conditions (e.g. cloud cover and aerosol distribution) and the *a priori* of the trace gas profile under consideration.

For the simplest case involving simple reflection of the light path on the ground, the increase in the light path is given by $1/\cos(\theta)$, which results in an excellent approximation (at SZA< ~75°) for the geometric AMF (AMF_{geo}) suitable for stratospheric absorbers:

$$AMF_{geo} = 1 + \frac{1}{\cos(\theta)} = 1 + \sec(\theta) \tag{4.12}$$

4.4.1   AMF Computation for Stratospheric BrO Profile

The apriori information needed for the AMF computation of Stratospheric BrO profiles in this work were based on balloon-borne measurements in particular [*Pundt et al.*, 2002] and comparisons with several measurements from balloon-borne, ground-based, space borne platforms and modeled data [e.g. *Pundt et al.*, 2000, 2002; Harder et al., 2000; *Van Roozendael et al.,* 2002, *Ferlemann et al.,* 1998; *Aliwell et al.,* 2002; *Sinnhuber et al.,* 2002]. Because of the difficulties entailed in simulating precise atmospheric conditions that take into account the atmospheric parameters needed as input into the RTM, calculation of appropriate AMFs represents a major hurdle. Hence, what is done is to calculate 'standard AMFs' for several typical atmospheric BrO profiles that take into account the dependence on properties such as the ground albedo, aerosol extinction, typical height profiles of temperature, pressure, O_3 and NO_2 distribution [*Richter et al.,* 1998; *Wagner,* 1999]. The RTM used, SCIATRAN [Rozanov et al., 2004] takes into account full spherical geometry and multiple-scattering processes in the atmosphere.
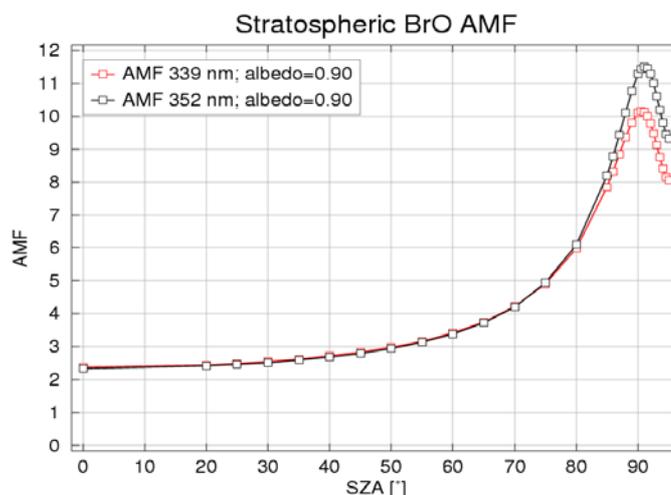
Figure 4.3: A 'standard' stratospheric AMF calculated for a stratospheric BrO profile for different SZAs at two wavelengths (339 nm and 352 nm) for a winter background maritime aerosol scenario, full multiple scattering treatment and an albedo of 90%. Note the similarities (from 0°-75° SZA) and the divergence in AMFs thereafter.
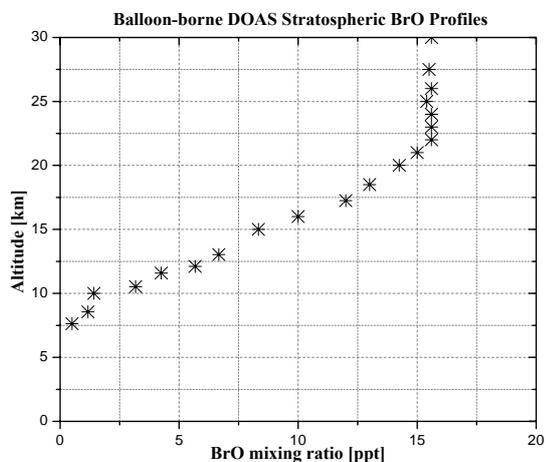
Figure 4.4: A Stratospheric BrO profile used in calculating the AMFs above. Profiles are based on measurements from balloon-borne platforms [Adapted from *Pundt et al.,* 2002].

4.4.2   AMF Computation for Tropospheric BrO Profile

AMF computation for tropospheric absorbers is a more cumbersome process not only because detailed information is required for parameters such as the surface albedo and aerosol loading near the surface but also because of multiple-scattering from partly-cloudy or cloudy scenes which complicates radiative transfer through the troposphere.
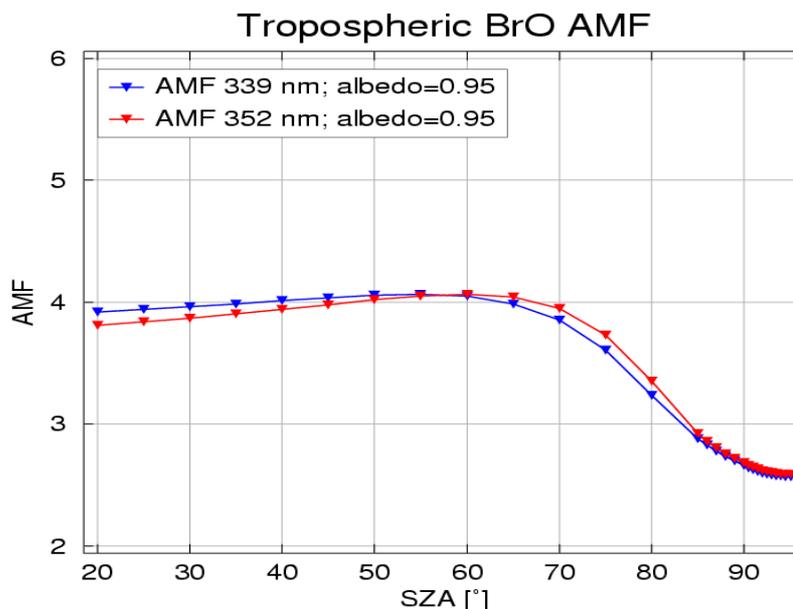
Figure 4.5: AMF for a Tropospheric BrO profile accounting for ~ 0.5-1.0 ppt BrO input from 0-2 km altitude, 95% albedo and a winter background maritime aerosol scenario.

Figure 4.5 shows calculated AMFs for a tropospheric BrO profile that accounts for a BrO mixing ratio of 0.5-1 ppt from the surface to 2 km. Troposphere AMFs are less dependent on SZA's compared to stratospheric AMFs. In contrast to stratospheric AMFs, AMFs for tropospheric species are much more influenced by variations in atmospheric conditions. Hence without adequate information about parameters such as the ground albedo and the aerosol loading the uncertainties are within a factor of 3 to 4 [*Wagner*, 1999].

4.4.3   Influence of Surface Albedo

For nadir-viewing space-borne instruments such as GOME or SCIAMACHY, photons registered by detectors have either been reflected from the earth's surface or scattered by particles (including clouds) in the atmosphere. Therefore information about the average surface albedo for a cloud-free scene of the ground pixel and the average albedo of a cloudy scenario is needed because the ratio between reflected and scattered photons depends strongly on surface albedo, wavelength and atmospheric aerosol loading. In particular, abrupt changes in reflecting characteristics such as the border between land and ocean surface can significantly influence retrievals. Figure 4.5 shows typical scenarios for a stratospheric BrO profile for different surface albedo:
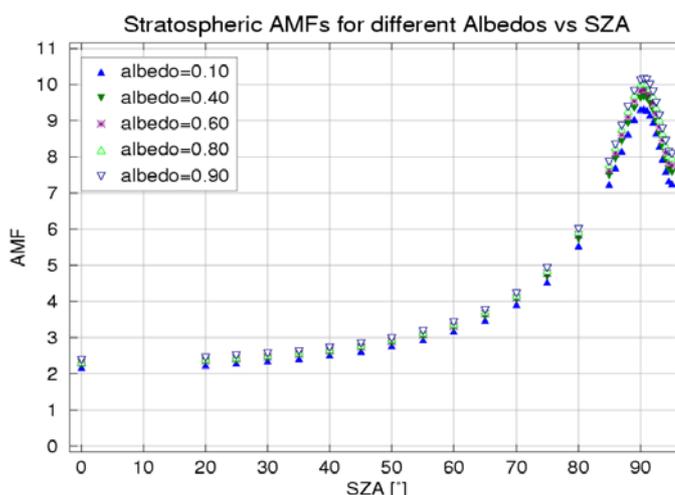
Figure 4.5: Effect of changes in surface albedo variations on BrO AMFs as a function of SZA at 339.0 nm

There exists only a slight influence at smaller SZAs for stratospheric AMFs, though the difference seems to amplify towards larger SZA. The influence of the surface albedo is even more pronounced on satellite AMF for tropospheric species.
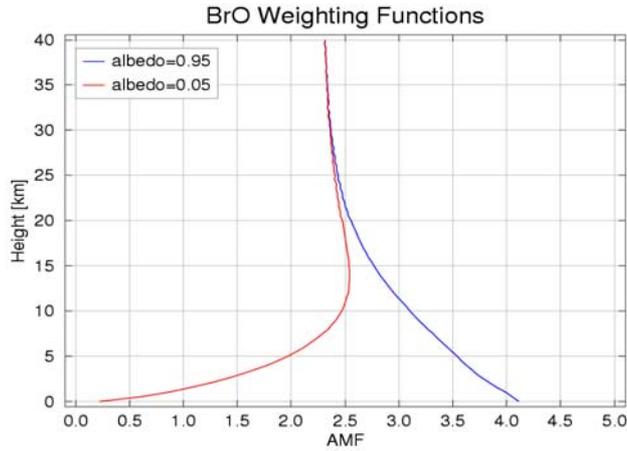
Figure 4.6: Sensitivity of satellite measurements of BrO at 352nm: Airmass factor variation as a function of altitude for 40° SZA, 5% and 95% albedo and a cloud-free scene.

Figure 4.6 shows the influence of surface albedo on satellite AMFs from the surface up to an altitude of about 40 km. For tropospheric species, low surface albedo corresponds to low AMFs while high reflectivity at the surface corresponds to high AMFs.

4.4.4   Influence of Aerosol scenario

Aerosol loading of the atmosphere can significantly influence retrievals from space-borne platforms not only because they can obstruct the light path to the troposphere especially in the case of large volcanic eruptions but also because the light path absorption can be elongated due to multiple scattering. Hence, aerosols act to significantly alter the earth's radiation budget. Tropospheric aerosols have a relatively short lifetime (5-10 days) [*Penner et al.*, 2002] and a high degree of variability. Partly as a result of this variability, models have become the primary means used for assessing the global atmospheric effects of aerosols. Large uncertainties thus exist when assessing the influence of aerosols on satellite-based retrievals as a result of high variability in space and time.

4.5   The Influence of Clouds on Satellite Retrievals

Nadir-viewing satellite instruments such as GOME or SCIAMACHY are strongly influenced by the presence of clouds, as a result of the enhanced reflection of the incident light especially in the visible [*Kurosu et al.,* 1997; *Pfeilsticker,* 1998; *Richter et al.*, 1998; *Wagner*, 1999]. Accurate evaluation of the observed radiances from such instruments therefore requires the detection of the presence of clouds in a ground pixel. For a satellite-based instrument, clouds effectively obstruct the line of sight to parts of the troposphere below cloud top height (figure 4.7). Although multiple scattering processes inside the cloud can occur thereby promoting the enhancement of

the light path, this effect is of less importance for reflected light when compared to light transmitted through the cloud [*Kurosu et al.,* 1997; *Pfeilsticker,* 1998; *Richter et al.*, 1998; *Wagner*, 1999].
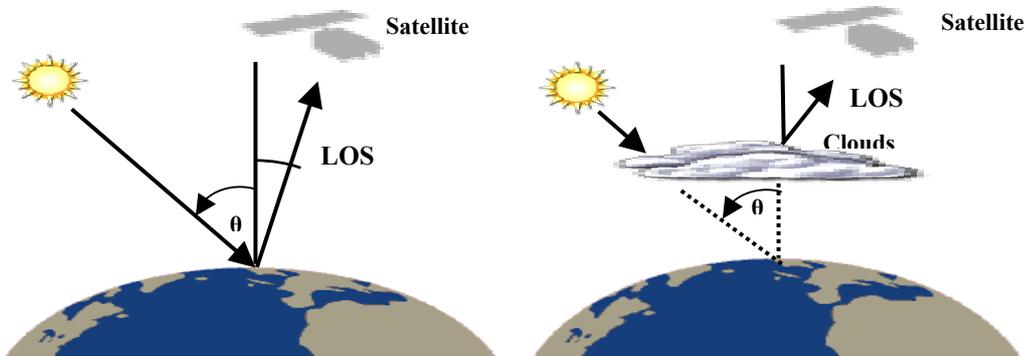
Figure 4.7: For a nadir-viewing instrument, complications arise especially in the retrieval of tropospheric constituents due to e.g. cloud cover and aerosol scenarios obstructing and scattering the light path in the atmosphere. AMF calculations are also strongly dependent on the surface albedo in question.

The influence of the surface albedo (*see figure 4.6*) also enhances sensitivity to absorption above clouds.

4.6   The Ring Effect

When light encounters molecules in the air, the photons experience not only elastic scattering due to Rayleigh- and Mie-scattering but also inelastic Raman scattering which in this case causes changes in photon energy. Fraunhofer spectra were observed that corresponds to an effective 'Filling-in' of the Fraunhofer structures [*Brinkmann,* 1968; *Bussemer,* 1993; *Vountas et al.,* 1998].
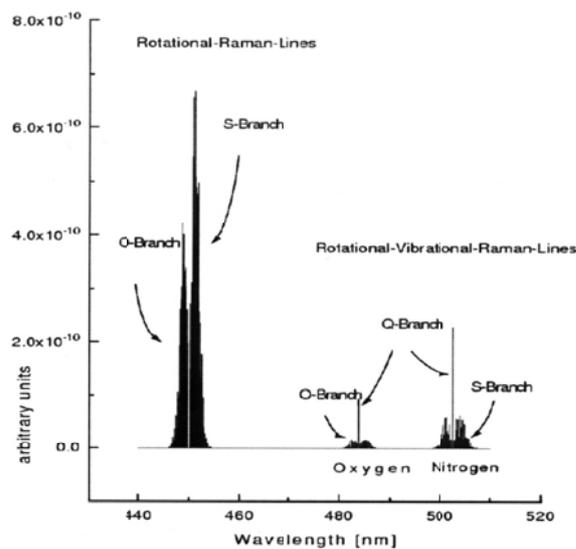
Figure. 4.8: Transition states for rotational and vibrational Raman scattering on O_2 and N_2 molecules [Haug, 1996].

This effect is called the 'Ring-Effect' [*Grainger and Ring,* 1962] after its discoverer and complicates the complete removal of the Fraunhofer structures. The spectra of scattered sunlight have Fraunhofer lines less deep than in direct sun measurements. The Fraunhofer lines of the measured spectra cannot be completely corrected for by inclusion of the Fraunhofer spectrum in the fitting procedure. It is accounted for by including a Ring spectrum, which is calculated from the ratio of Rayleigh and Raman cross-sections in the fitting procedure [*Solomon et al.,* 1987]. The cross-section for Raman scattering can be calculated from the known energies of N_2 and O_2. For more details see *Wagner* (1999) and references therein.

4.7   The Solar I_0 Effect

As a result of the limited spectral resolution of DOAS instruments in the UV/Visible region (typically in the range of about a few tenths to several nanometers), the natural line widths of the solar and the atmospheric absorptions are usually not spectrally resolved. This is especially true for absorptions showing narrow spectral structures. The absorptions found in the measured atmospheric spectra cannot be properly fitted by the respective laboratory cross-sections that are usually derived using a light source with a smooth spectrum. Hence dividing the measured spectrum by the Fraunhofer spectrum fails in totally removing the Fraunhofer structures, because the convolution ratio cannot be exchanged [*Wagner et al.,* 2001]. Since this effect arises from the spectral structure of the solar spectrum (I_0), it was referred to as the 'solar I_0 effect' [*Johnston,* 1996; *Richter,* 1997; *Aliwell et al.,* 2001]. Details for the correction of the I_0 effect can be found in *Wagner,* 1999 and *Wagner et al.,* 2001 but what is done is to account for the 'I_0-corrected' cross-sections, which are calculated by convolving the highly resolved solar spectrum (I_0) and the absorption spectrum of the chosen trace gas with the instrument slit function.

Thus, the derived cross-sections can now match the absorptions in the measured atmospheric spectrum. It has been shown for GOME measurements of BrO that errors introduced as a result of the solar I_0 Effect was found to be in the range of only a few percent [*Wagner,* 1999]. However for ground-based measurements of BrO at summer mid-latitudes, errors of up to 30% has been reported [*Aliwell et al.,* 2001].

Chapter 5

BrO DOAS Analysis from GOME Nadir Observations

5.1 GOME Calibrated Irradiance and Radiance Spectra

GOME level 0-1 processing [*see Balzer et al.,* 1996] involves two calibration tasks: *Spectral calibration* and the *radiometric calibration*. The radiometric calibration comprises the adjustments of the lv-0 data to account for the *leakage current*, *straylight*, and the *detector pixel-to-pixel variability* (using on-board LED measurements). The *polarisation correction,* which is a complicated part of the radiometric calibration, transforms the measured signal into a signal that would have been measured if the same light intensity had been detected with unpolarised light. Finally, the measured signal (in binary units per second) is converted into radiance by using the Bi-directional Scattering Distribution Function (BSDF) of the calibration unit (sun diffuser) and the radiance response function of the instrument, both functions determined during pre-flight calibration.
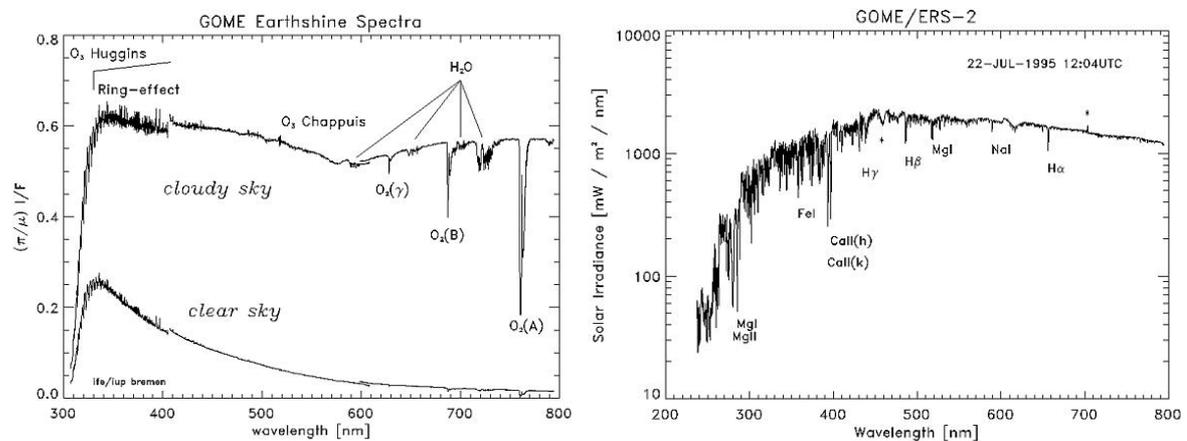
Figure 5.1: (Left-hand panel) Two examples of sun-normalised earthshine spectra recorded in September 1995 by GOME [*Burrows et al.,* 1995]. The uppermost curve is a reflectivity spectrum for a cloudy scene and the lower spectrum was taken under cloud-free conditions. Reflectivity is here defined as R=(I/F)(π/cos SZA), where *I* is the backscattered radiation, *F*, the directly measured solar irradiance, and SZA, the solar zenith angle. The absorption of the O_2 A-band at 760nm is used to determine the fractional cloud cover and (Right-hand panel) GOME Solar Spectrum taken on the 22nd July 1995 [*Weber et al.* 1998]. Selected prominent Fraunhofer lines are shown. The asterisks denote instrumental artefacts due to the changing transmission characteristics of the anti-reflection coating on the channel 3 beamsplitter (450nm) and due to a Wood's anomaly in the Channel 4 holographic grating (700nm). The overlap regions of the four optical GOME channels are at 315nm, 405nm, and 600nm.

Once a day (every fourteenth orbit) GOME solar irradiance measurements are carried out when the ERS-2 satellite crosses the terminator in the north polar region coming from the night side. Since GOME is not equipped to actively track the sun, viewing of the full solar disc is only possible for a time span of about 50 sec. Integration times are 0.75 sec for all channels, except for the UV channel, where the integration time is doubled. A mean solar spectrum is constructed from the series of measurements during full disc solar viewing. Figure 5.1 shows a calibrated mean solar spectrum measured by GOME in 1995.

5.2 Reference Spectra and Ring Spectrum for derivation of Optimal Slant Column Densities

For the determination of the GOME BrO slant column densities, there are two options for the absorption cross-sections used in the analysis: either using high accuracy and spectral resolution cross-sections and convolving them with the instrument slit function or using cross-sections measured with the instrument itself. The reference spectra of BrO, NO_2, OClO, O_4, and O_3 (at two temperatures 221 and 241 K) and calculated Ring and Fraunhofer spectrum listed in table 5.1 are used. I0 corrections are applied to O_3 and NO_2 spectra. Optimisation and recommendation for the fitting process then follows the propositions issued in the extensive studies of *Aliwell et al.*, 2002.

Ref. spectrum	Temperature [K]	Source
BrO	228	Wahner et al., 1999
O_3*	221	GOME-FM [Burrows et al., 1999]
O_3*	241	GOME-FM [Burrows et al., 1999]
NO_2*	221	GOME-FM [Burrows et al., 1998]
OClO	213	Kromminga al., 1999
O_4	296	Greenblatt et al., 1991
Calc. Ring Spectrum	---	Vountas et al., 1998
Fraunhofer Spectrum		Kurucz
Undersampling		Chance, 1998
Wavelength calibration based on Kurucz solar spectrum		
Offset (constant + slope); (*- denotes shift in cross-sections of 0.03 nm)		

Table 5.1: Reference spectra used in the GOME BrO analysis.

5.3 Undersampling and Doppler Shift Correction in GOME Spectra

The GOME instrument suffers from significant spectral undersampling. The undersampling problem arises from the poor sampling ratio of the instrument, which results in loss of spectral information when interpolating the earthshine radiance during the DOAS fitting process. As a result substantial residual structures, largely constant from spectrum to spectrum are found in the initial radiance fitting regions used for NO_2, BrO, OClO and HCHO, leading to difficulties in the analysis of the atmospheric radiances [*Chance*, 1998; *van Roozendael et al.*, 1999; *Wagner*, 1999]. To some extent, this can largely be corrected for by using an ad-hoc cross-section obtained by simulating the effect based on a high-resolution solar reference spectrum. This can then be included as an additional pseudo-absorber in the DOAS fitting procedure.

Once per day, GOME measures a solar spectrum, when it flies over the North Pole into the sunlight along one of its orbits. Hence when GOME flies into the Sun, there is a Doppler shift in the wavelength of $\lambda \upsilon/c$, where υ is the satellite velocity (about 8.3 km/s) and c the speed of light. This shift is about 0.008 nm at $\lambda = 300$ nm and 0.022 nm at $\lambda = 800$ nm. The calibration methods fitting of a shift and a squeeze against the solar reference spectrum automatically corrects for this Doppler shift.

5.4 BrO SCD and VCD retrieval from GOME in the 344.7-359.0 nm Spectral Range

The BrO evaluation method used for the retrieval of GOME BrO total SCD is the Differential Optical Absorption Spectroscopy (DOAS) method [*Platt*, 1994] and it has similarities to that developed for ground-based DOAS measurements [*Richter et al.*, 1998]. The total GOME BrO SCD includes contributions from the stratosphere, the free troposphere and the boundary layer. The inversion is performed in the 344.7-359.0 nm spectral range using:

- The appropriate absorption cross sections (Table 5.1)

- Accounting for the GOME undersampling [*Chance*, 1998]. The undersampling problem arises from the poor sampling ratio of the instrument which results in a loss of spectral information when interpolating earthshine spectra during the DOAS fitting process

- A correction for the GOME diffusor plate spectral artefact [*Richter et al.*, 2002]. In practice, this is done afterwards on the slant columns retrieved.

- The effect of degradation of the scanning mirror. As with any space-borne instrument, the external optics of GOME undergo degradation over their lifetime, and since mid-2001, changes in the GOME scanning mirror surface structure introduced spectral anomalies in the measurements depending on viewing direction. These anomalies correlate with BrO absorption structures and introduce a large scan angle dependency in the retrieved columns. Using

the same assumption as for the irradiance correction, empirical compensation functions could be determined for each month and a large improvement in consistency achieved (see figure 5.3). This is done by taking the ratio of the east and west scans of the GOME of earthshine spectra over the ocean near the equator (where BrO amounts are assumed to be constant and at a background low). With this approach, the GOME BrO time series could be extended from 2001 up till date, albeit at reduced accuracy.

BrO total vertical columns are then derived from total slant columns, using the stratospheric AMF described in figure 4.4.

Arctic GOME VCD:
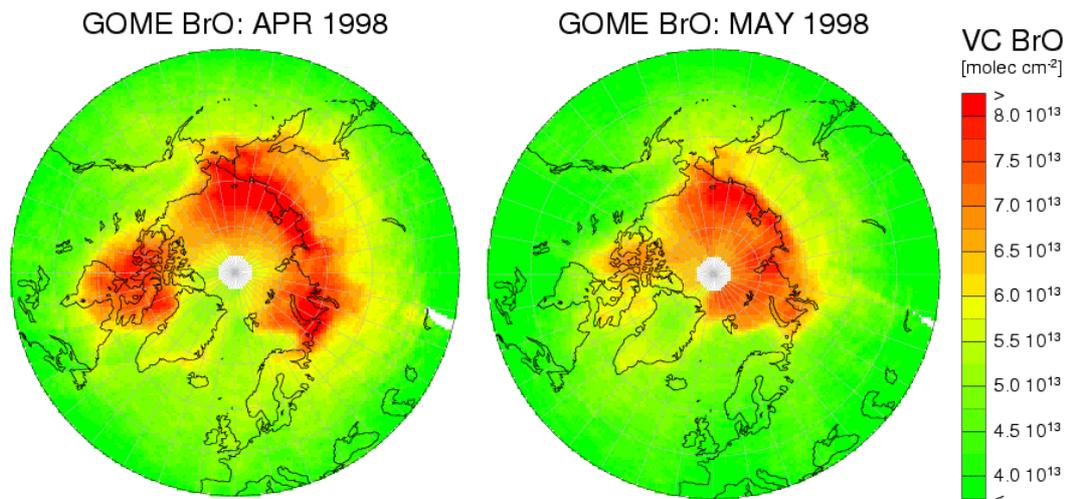
Antarctic GOME VCD:
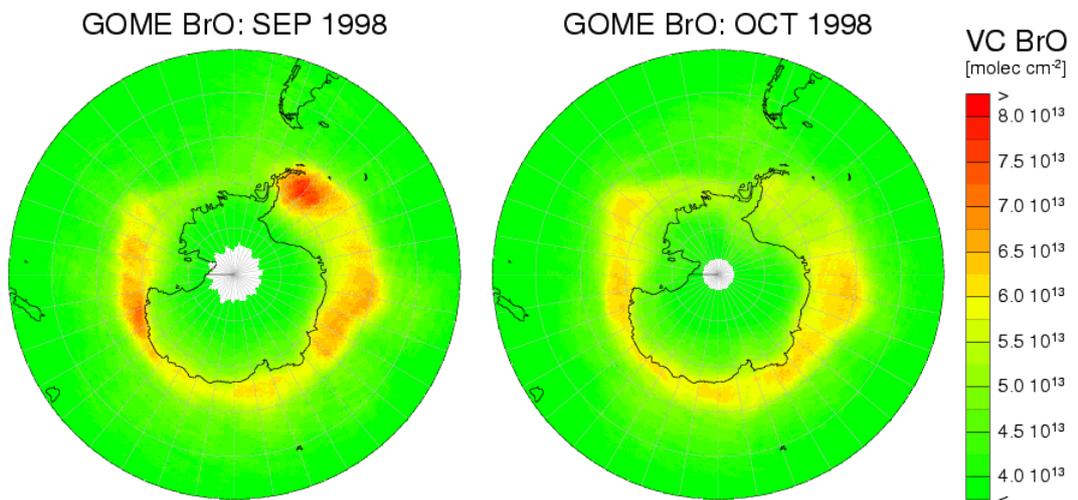
Figure 5.2: Examples of GOME monthly averaged VCD's for the Arctic and Antarctic in 1998.
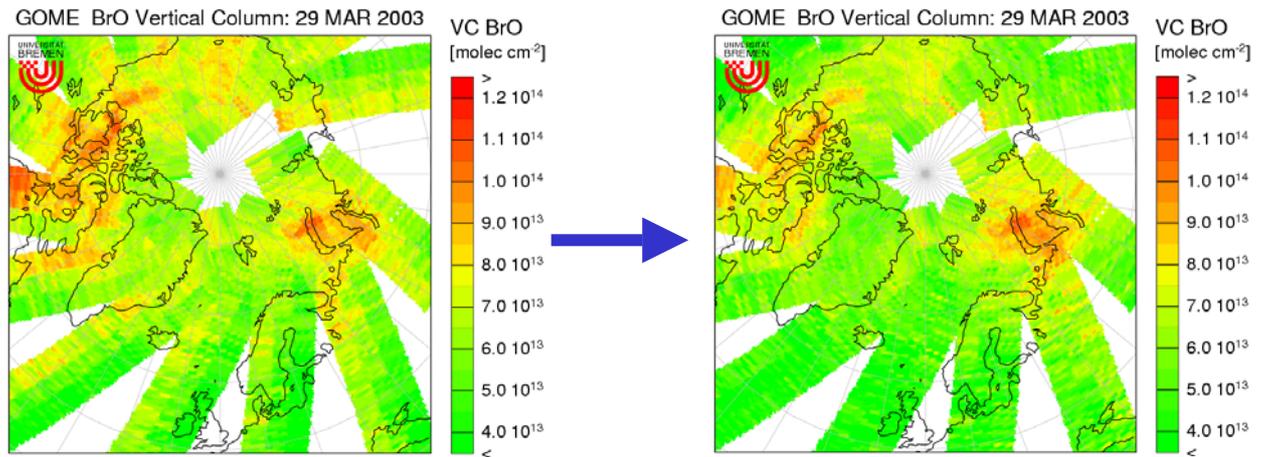
Figure 5.3: GOME BrO vertical columns without (left) and with (right) degradation correction for a single day (29th March 2003).

Chapter 6

BrO DOAS Analysis of SCIAMACHY Nadir Observations

6.1 Calibration of SCIAMACHY nadir Level 0 – 1 Spectra

SCIAMACHY level 0 data is converted into 'calibrated radiance' (level 1b) by applying calibration algorithms and calibration parameters. Parts of these calibration parameters are determined regularly using in-flight measurement data when SCIAMACHY looks into deep space or takes white light or spectral lamp, or sun diffuser calibration measurements. In addition, data from preflight instrument calibration, the so-called Key Data are required.

Currently, the level 1b data have been calibrated using the SciaL1C tool, which is part of the EnviView distribution. Existing calibration options (numbered from 0 to 7) of lv-1 data extraction procedures include:

- 0: Memory Effect Correction
- 1: Leakage Correction
- 2: Straylight Correction
- 3: PPG (Pixel-Pixel-Gain) Correction
- 4: Etalon Correction
- 5: Wavelength Calibration
- 6: Polarization Sensitivity Calibration
- 7: Radiance Sensitivity Calibration

However for the SCIAMACHY level 1b data set used for the DOAS analysis in this work, only Dark Current/Leakage Correction and Spectral/Wavelength calibration options were applied in the extraction of dataset for all UV/Visible channels.

6.2 Polarization Response in SCIAMACHY Channel 2

SCIAMACHY polarization response in the UV spectral range is characterized by the presence of a strong Wood's anomaly in channel 2 (309.0-405.0 nm) [*De Smedt et al.,* 2004; *Van Roozendael et al.,* 2004, *Afe et al.*, 2004], see *figures 6.1 and 6.2*. This anomaly introduces residual structures that interfere with the absorption features of BrO and HCHO in SCIAMACHY hence impacting on their retrieval in the traditional GOME fitting window at (344.7-359.0 nm) for BrO and (336.5-358.0 nm) for HCHO.
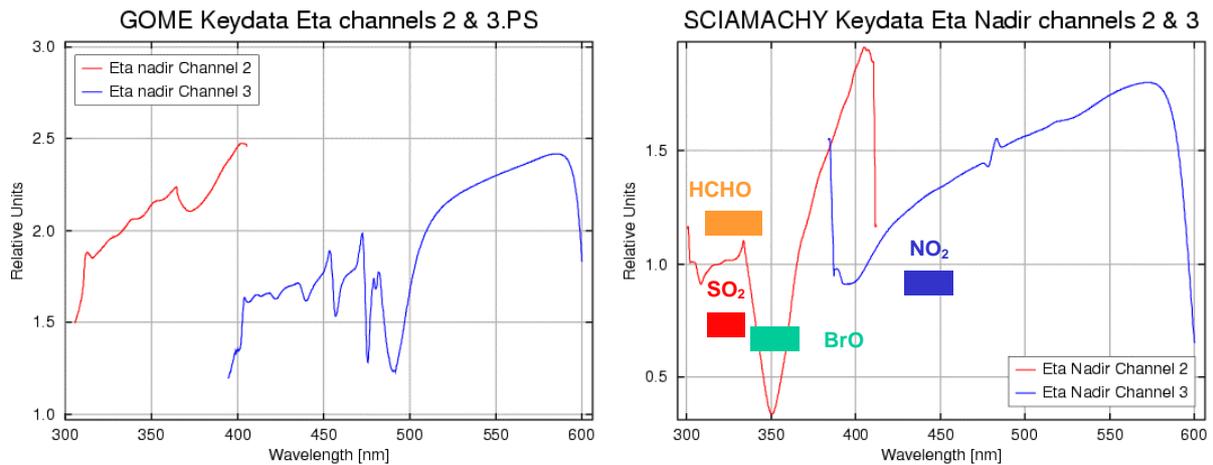
Figure 6.1: GOME (left) and SCIAMACHY (right) polarization response in the UV/Visible spectral range – nadir keydata functions (Eta channels 2 and 3) emphasizing the sensitivity of both instruments with respect to the wavelength range relevant to some trace gases.
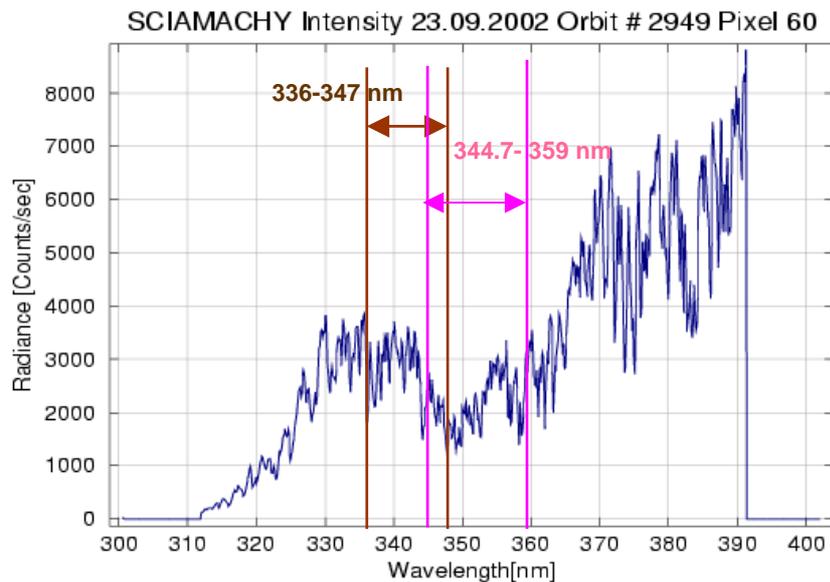
Figure 6.2: An example of an earthshine radiance spectrum from SCIAMACHY nadir mode recorded on the 23rd September 2002. The presence of a strong Woods anomaly in the 344.7-359 nm range used for the retrieval of GOME BrO leads to poor signal-noise-ratio in this wavelength range. Thus an alternative fitting window (336.0-347.0 nm) was employed to minimize the impact of residual structures from the polarization sensitivity of the instrument.

This lead to a change of settings in the analysis for the DOAS retrieval of SCIAMACHY BrO slant column densities.

6.3 BrO SCD Retrieval from SCIAMACHY

6.3.1 SCIAMACHY BrO data fitted using GOME BrO windows and settings

Initial attempts to fit the SCIAMACHY BrO data in the traditional GOME BrO spectral range (344.7-359.0 nm) using similar settings had to be abandoned due to problems related to the presence of strong polarization structures that interfere with the BrO absorption in the UV (*see section 6.2 above*).

Figure 6.3 depicts an example of a DOAS analysis performed on SCIAMACHY and GOME data taken from an orbit recorded on the 23rd of September 2002. Comparison of the overlapping slant column densities investigated reveals very poor signal-to-noise ratio accompanied by large offsets for SCIAMACHY BrO columns when fitted in the GOME BrO window with similar settings (Figure 6.3a). Later, two SCIAMACHY polarization key data functions (Eta and Zeta nadir key data) were included as part of the DOAS fitting process in an attempt to minimize the large errors. This attempt lead to relatively ample improvements in the SCIAMACHY BrO slant columns (Figure 6.3b), in particular reducing the large offsets but the noise in the SCIAMACHY BrO SCD's was still unacceptably high in all cases.

6.3a   **6.3b**
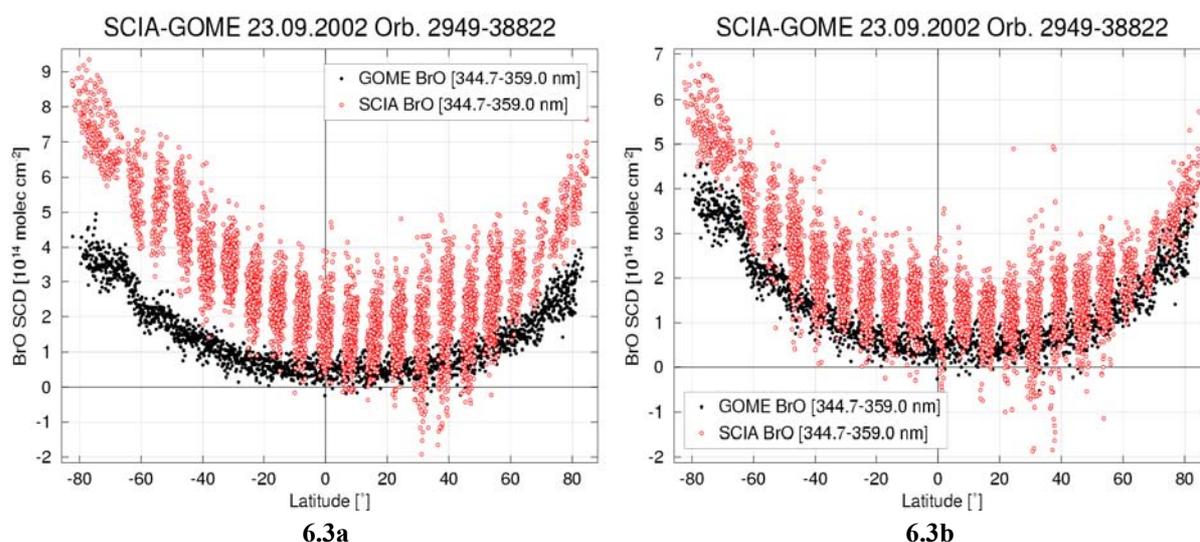
Figure 6.3: Comparison of SCIAMACHY and GOME BrO slant column densities fitted within the (344.7-359.0 nm) spectral range. SCIAMACHY key data functions were excluded (i.e. in 6.3a) and included (i.e. in 6.3b) in the DOAS fitting process.

Thus, the need arose for an alternative spectral range needed for the optimization of the SCIAMACHY BrO slant columns in the UV spectral range that minimizes the impact of the residual structures and ensures the quality of the retrieval is not affected.

6.3.2 SCIAMACHY BrO data fitted in new UV- shifted window-Comparisons to GOME BrO SCD's

Thus, a new UV-shifted window (336.0-347.0 nm), was tested on the SCIAMACHY BrO data. In this shorter wavelength region, the effects of the polarization structures are weaker (*figure 6.2*) and therefore have little impact on the accuracy of the DOAS procedures). The retrieved BrO slant column densities were found to be consistent with the GOME BrO slant columns and offer improved signal-noise-ratio (*as an example see figure 6.4 below*). Degradation of SCIAMACHY data to the GOME resolution further improves
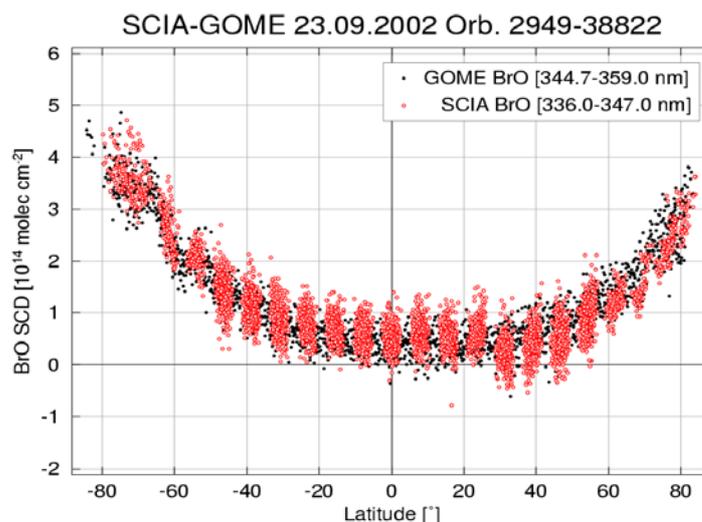
Figure 6.4: Comparison of the SCIAMACHY data fitted in the new UV-shifted wavelength interval (336.0-347.0 nm) and GOME BrO slant column densities fitted within the (344.7-359.0 nm) spectral range.
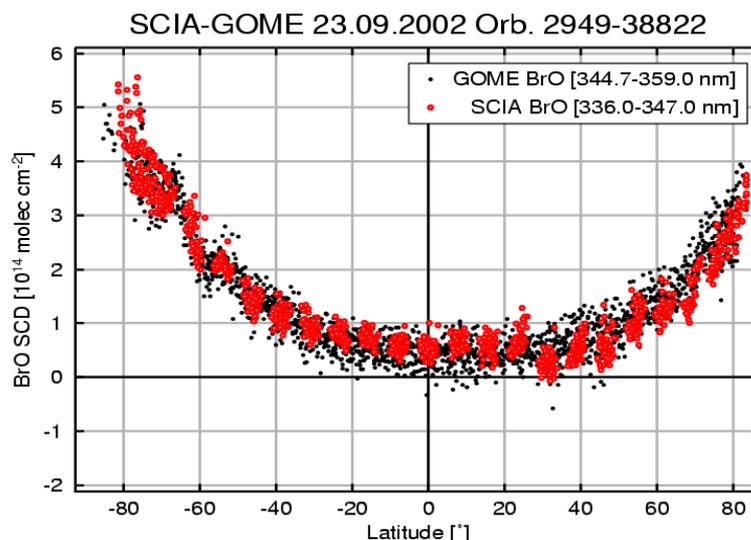
Figure 6.5: Comparison of the SCIAMACHY SCD (in this case degraded to the GOME resolution i.e. similar integration times) fitted in the new UV-shifted wavelength interval (336.0-347.0 nm) and GOME BrO slant column densities fitted within the (344.7-359.0 nm) spectral range. The relatively larger scatter in SCIAMACHY SCD in figure 6.4 is a result of the shorter integration time that improves spatial resolution at the expense of signal-noise-ratio. The scatter has significantly reduced in figure 6.5.

the signal-to-noise ratio of the SCIAMACHY SCD relative to the GOME SCD (figure 6.5)

Consistency checks: GOME BrO in the different fitting windows

Sensitivity studies were also performed on the GOME BrO data in the UV-shifted
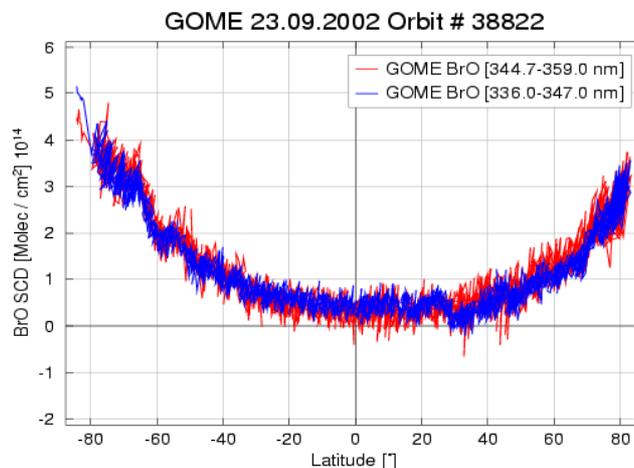
Figure 6.6: Comparison of GOME BrO in the traditional fitting window (344.7-359.0 nm) and the new UV-shifted wavelength interval (336.0-347.0 nm).

wavelength interval and comparisons of the resulting slant column densities made to the same data analyzed in the traditional spectral range (344.7-359.0 nm) but using similar settings. Extensive tests show that the slant column density evaluations in both windows are in very good agreement, though the UV-shifted window seems to offer a better signal-to-noise ratio (*see figure 6.6 as an example*) on an orbit-to-orbit basis.

Influence of the OClO cross-section in the GOME UV-shifted window

GOME BrO evaluations in the 336-347 nm spectral range is also influenced by the inclusion of the OClO cross-section in the DOAS fitting process. The OClO cross-section used for the DOAS analysis in this study is the vacuum wavelength cross-section of *Kromminga et al.*, 1999 obtained from Fourier Transform Spectroscopy.
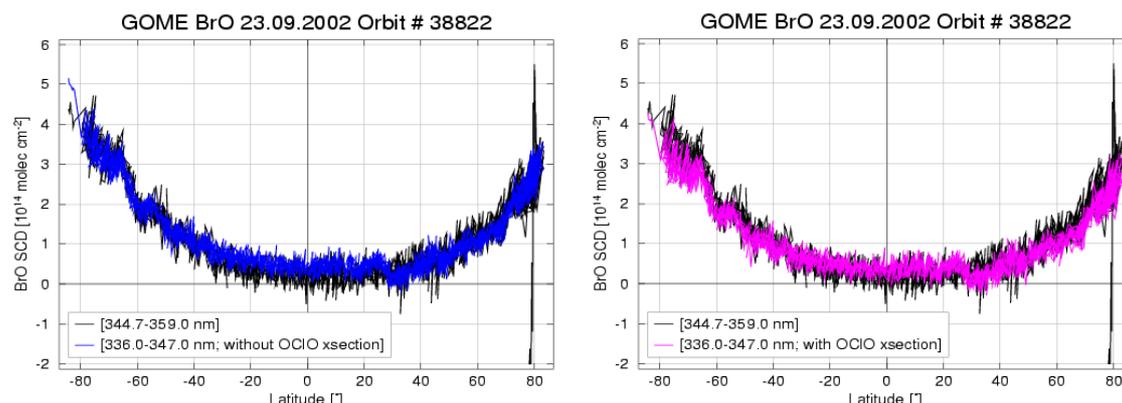
Figure 6.7: Comparison of GOME BrO SCD in the 344.7-359.0 nm and the new UV-shifted wavelength interval (336.0-347.0 nm) excluding (left panel) and including (right panel) the OClO cross-section in the DOAS process. Exclusion of the OClO cross-section from the DOAS process in the 336-347 nm range matches very well with the retrieval at the 344.7-359 nm but problems are evident with the BrO SCD in the 336-347 nm window resulting in slightly lower slant columns especially at polar high latitudes.

As shown in figure 6.7 for example, excluding the OClO cross-section in the DOAS procedures for the GOME BrO analysis in the 336.0-347.0 nm agrees well at all latitudes to the GOME BrO evaluations in the 344.7-359.0 nm spectral range (figure 6.7 – left panel). However, inclusion of the OClO cross-section in the shorter UV-shifted window results in slightly lower SCD at the polar high latitudes when compared to the SCD obtained in the traditional fitting window (figure 6.7b).

6.3.3 HCHO Interference in SCIAMACHY BrO DOAS Analysis

The formaldehyde cross-section has strong absorption features in the UV-shifted spectral range where SCIAMACHY BrO is analyzed and thus influences the retrieved BrO SCD's especially over areas of strong biomass burning which is a major source of HCHO release into the atmosphere. However, accounting for HCHO absorption in the DOAS process for SCIAMACHY BrO analysis results in poorer signal-to-noise ratio in the retrieved SCD's (e.g. figure 6.8a) relative to when HCHO is excluded from the SCIAMACHY BrO DOAS fits (figure 6.8b).

6.8a   6.8b
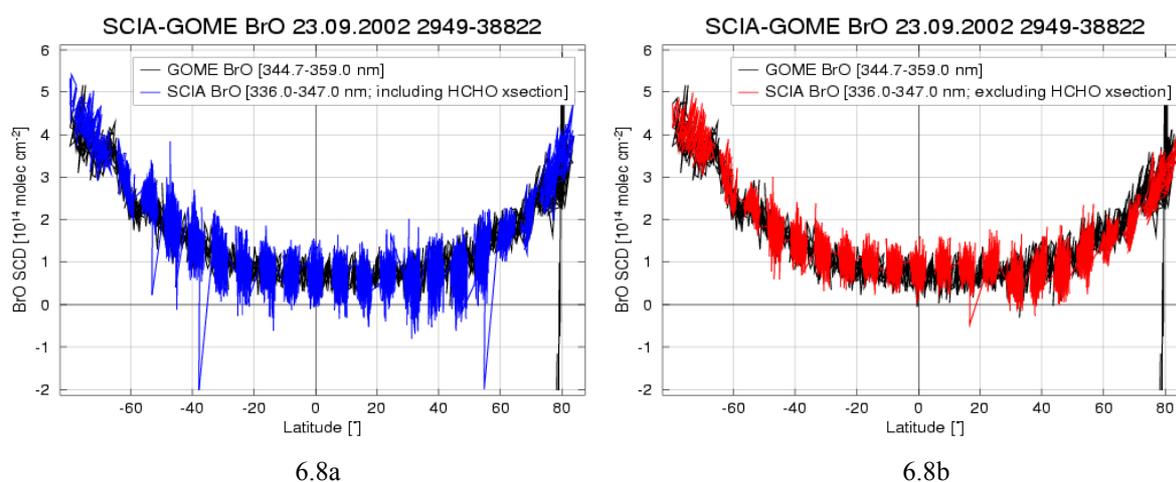
Figure 6.8: An example of SCIAMACHY and GOME BrO SCD comparisons with HCHO cross-section included in the SCIAMACHY BrO DOAS fitting procedure (left) and without accounting for HCHO cross-section in the fit process (right). Accounting for HCHO in the DOAS fitting process leads to poorer signal-to-noise ratio in the BrO SCD in all cases of the SCIA BrO analysis even over areas of particularly strong biomass burning that injects HCHO into the atmosphere. This effect is however most prevalent at mid-latitudes and the equatorial regions but generally less pronounced at high polar latitudes.

Thus the current option or analysis settings for SCIAMACHY BrO SCD retrieval excludes HCHO cross-section from the DOAS procedures. These results in smoother (better signal-to-noise) BrO slant columns, that matches well with the corresponding GOME slant column densities.

6.4 Impact of using different BrO Cross-sections

Extensive tests have been performed using three different BrO cross-sections: the **Wahner** [*Wahner et al.*, 1988], **Wilmouth** [*Wilmouth et al.*, 1999] and **Fleischmann** cross-sections [*Fleischmann et al.*, 2004]. Although, SCIAMACHY BrO SCD's using the Wilmouth and Fleischmann cross-sections at 336.0-347.0 nm demonstrated a better signal-noise-ratio compared to evaluations done with the Wahner cross-section, the best consistency and stability of SCIAMACHY BrO SCD at 336.0-347.0 nm with subsequent GOME BrO evaluations at 344.7-359.0 nm is achieved using the Wahner
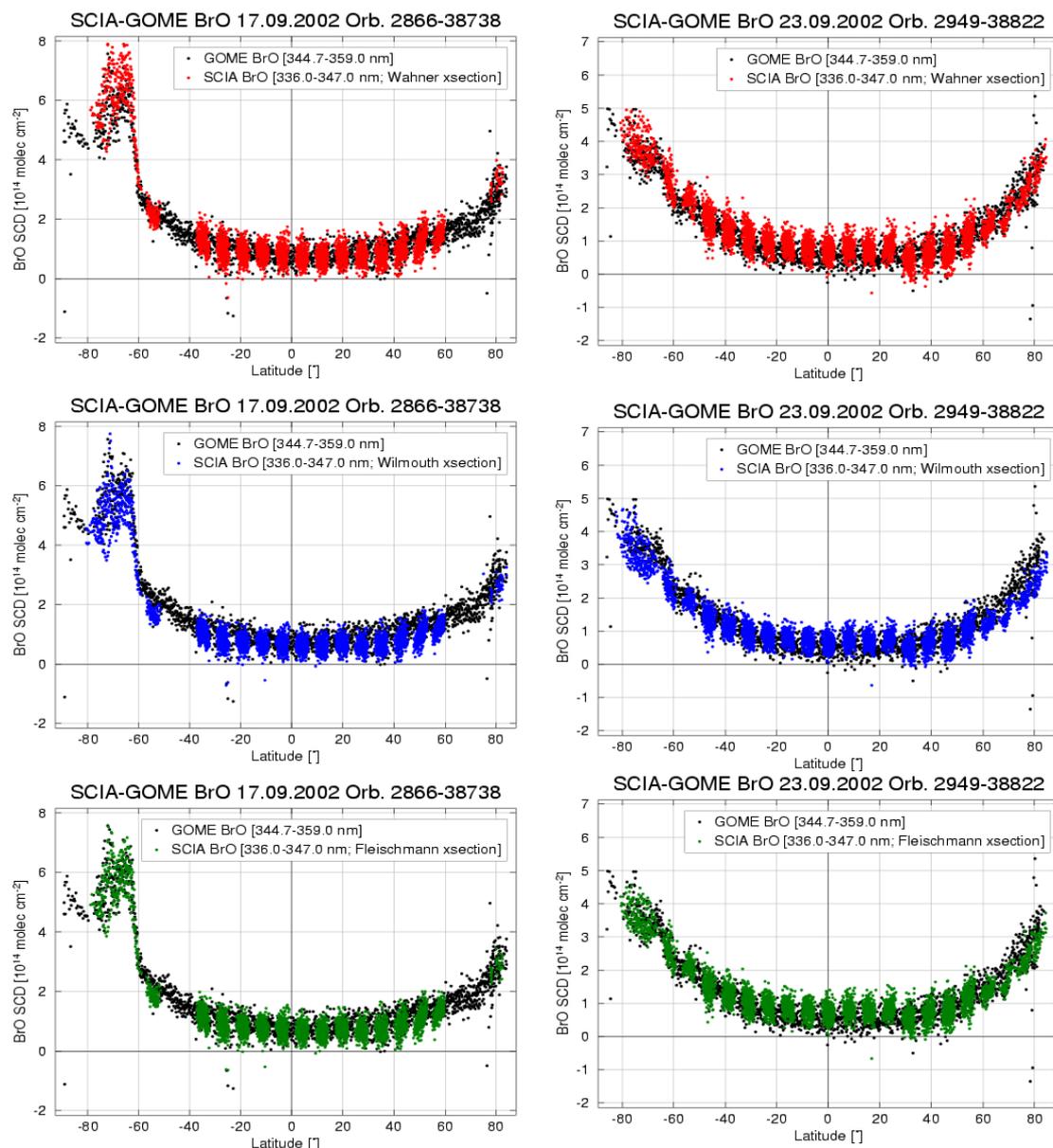
Figure 6.9: Comparisons between SCD's of GOME BrO analysis (using Wahner BrO cross-section) and corresponding SCD's of SCIAMACHY BrO at **336.0-347.0 nm** using the Wahner, Wilmouth and the Fleischmann BrO cross-sections respectively. Best consistency with the GOME BrO slant columns is achieved using Wahner and Fleischmann cross-sections.

cross-section. This is particularly obvious at high polar latitudes (*see figure 6.9 for example*) in the comparison of GOME and SCIAMACHY SCD's recorded on the 17th and 23rd September 2002.

Another alternative UV-shifted window for SCIAMACHY BrO has also been proposed and tested at 336.0-351.5 nm. In this case, polarisation correction functions Eta- and Zeta- nadir keydata functions (*figure 6.1*) have to be included in the DOAS fitting procedures.
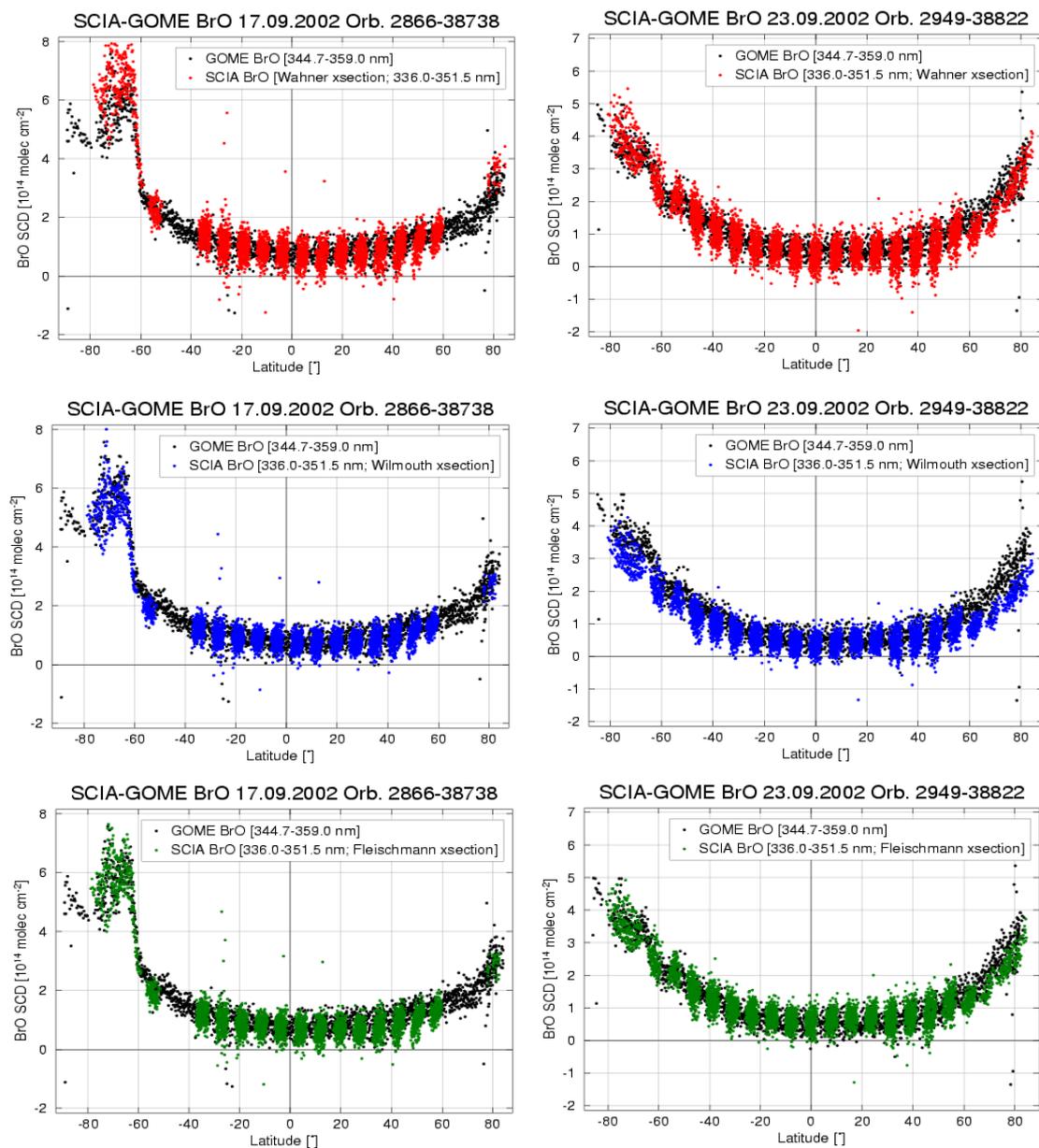
Figure 6.10: Comparisons between SCD's of GOME BrO analysis (using Wahner BrO cross-section) and corresponding SCD's of SCIAMACHY BrO on the 17th and 23rd September 2002 at a longer UV-shifted spectral range **336.0-351.50 nm** using the Wahner, Wilmouth and the Fleischmann BrO cross-sections respectively. In this case, polarisation correction functions Eta- and Zeta nadir keydata are included in the DOAS analysis. Best results for consistency and stability with the GOME BrO SCD's are also achieved using the Wahner cross-sections for the SCIAMACHY BrO retrieval in the DOAS analysis.

Extensive tests on SCIAMACHY BrO data fitted in the longer UV-shifted spectral range (336.0-351.5 nm) show that the same problems of inconsistency in SCD with GOME BrO evaluations in the traditional fitting window are encountered when using the Wilmouth BrO cross-sections in the DOAS analysis (*figure 6.10*). However, the results of the SCIAMACHY BrO SCD's obtained using the Wahner cross-sections at 336.0-351.5 nm in the DOAS analysis are consistent and stable with respect to GOME BrO SCD's at the 344.7-359.0 nm range (*See figure 6.10*).

In this PhD thesis, the recommended settings for the optimum retrieval of SCIAMACHY BrO using the DOAS technique is done in the 336.0-347.0 nm window and the cross-sections employed are displayed in Table 6.1. In this spectral range, the SCD's retrieved from SCIAMACHY are stable and consistent with respect to the GOME BrO evaluations at 344.7-359.0 nm. Moreover, additional correction functions for the polarization sensitivity of the instrument in channel 2 (i.e. the nadir keydata polarisation correction functions) are also avoided.

Ref. Spectrum	Temperature [K]	Source
BrO	228	*Wahner et al.*, 1988
O_3	223	*Bogumil et al.*, 1999
O_3	243	*Bogumil et al.*, 1999
NO_2	243	*Bogumil et al.*, 1999
OClO	293	*Bogumil et al.*, 1999
O_4	296	*Greenblatt et al.*, 1991
Calc. Ring Spectrum		*Vountas et al.*, 1998, (SCIATRAN RTM)
Fraunhofer Spectrum		Kuructz, 1998
Undersampling		Chance, 1998
Wavelength calibration based on Kurucz solar spectrum		
Offset (constant + slope)		
Daily noon ASM solar reference spectrum		

Table 6.1: Reference spectra and molecular absorption cross-sections employed in the SCIAMACHY BrO analysis at 336.0-347.0 nm.

Figure 6.11 highlights examples of the measured fit spectrum of the various absorption cross-sections of the relevant atmospheric trace gases compared to corresponding laboratory absorption cross-sections.
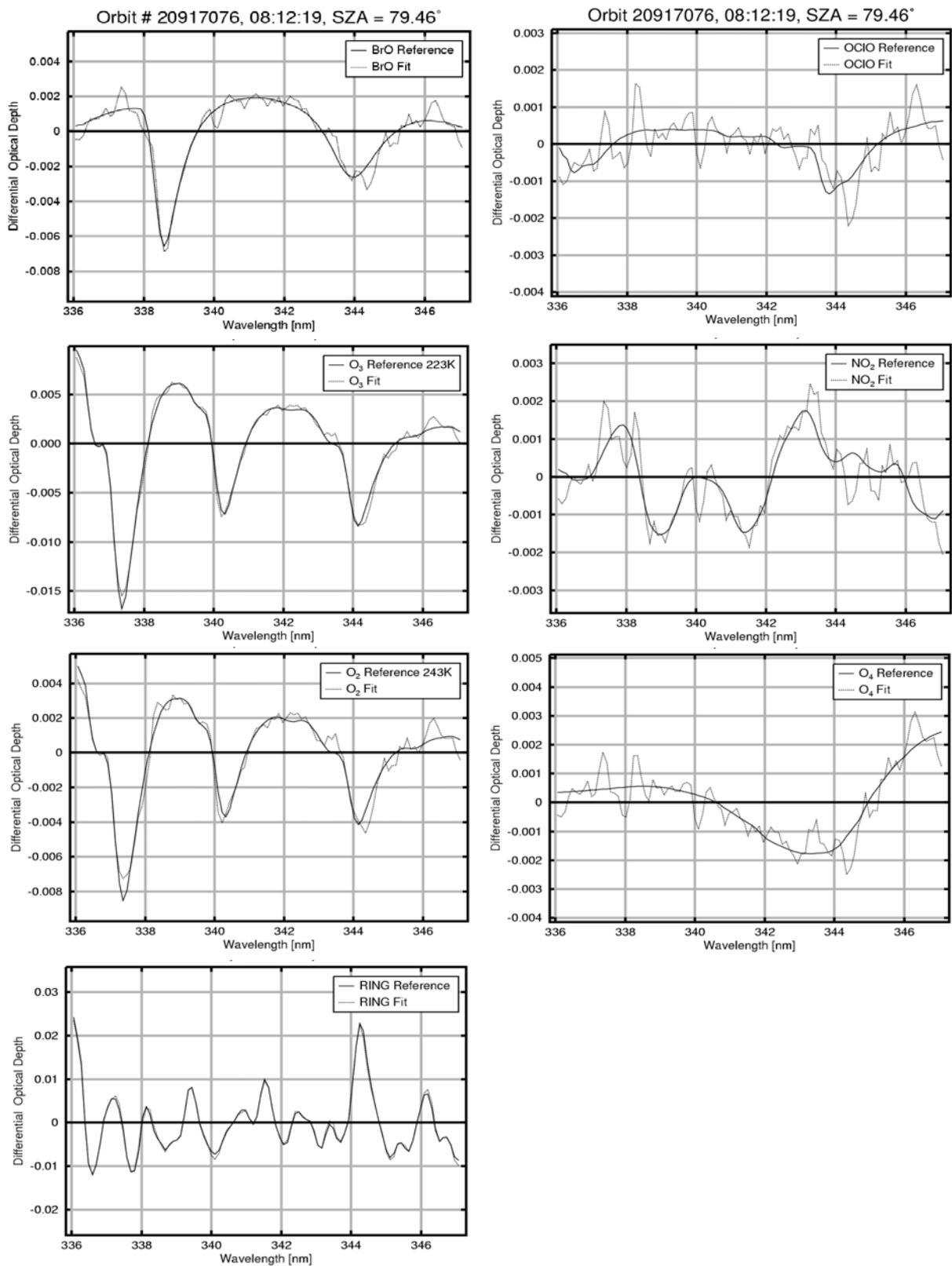
Figure 6.11: Examples of the laboratory (thick lines) and observed (dashed lines) fit spectrum employed in the evaluation of the SCIAMACHY BrO analysis.

6.5 SCIAMACHY BrO Vertical Column Densities – Enhanced BrO Explosion Events in the PBL.

From the derived SCIAMACHY BrO slant column densities, vertical column densities can be obtained using appropriate airmass factors calculated using the RTM SCIATRAN. The RTM takes into account the effects of multiple scattering in the atmosphere.

As a prerequisite for the conversion of the obtained SCD's to VCD's, the stability of the SCIAMACHY instrument with respect to the retrieval of BrO SCD was checked. This was done by obtaining a longer time series in SCD's retrieved over the Atlantic (where variations in BrO are supposed to be at the very minimum) using a fixed solar reference spectrum on one hand and an ASM solar irradiance spectrum taken each day at noon in the DOAS procedures on the other hand.

Employing a fixed solar reference spectrum as an absorption-free background in the analysis for all measurements introduces huge deviations (or offsets) in the retrieved SCD's during decontamination and large changes ((> 100%) during nominal operations (*figure 6.12*). Although stability is a problem (when using a fixed solar reference spectrum as background), the main point of figure 6.12 is a spectral interference of solar activity and BrO retrieval. However, use of a daily noon solar irradiance spectrum leads to much ample improvements in the quality and stability of the retrieved BrO SCD's.
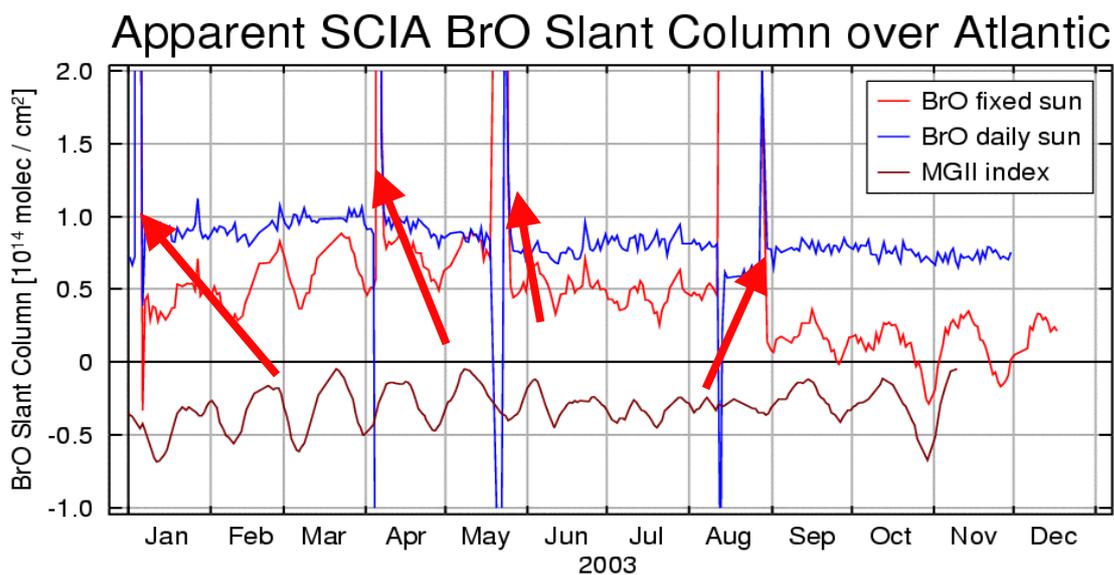
Figure 6.12: SCIAMACHY BrO slant columns over the Atlantic for a fixed and daily noon ASM solar irradiance spectrum as background for year 2003. Daily noon ASM solar spectrum is the obvious choice for the SCD determination as it results in smoother columns. The SCD's achieved with a fixed solar spectrum shows large variations and huge offsets. It also shows a strong correlation with the MGII index. The red bold arrows indicating irregularities (sharp peaks) are periods when SCIAMACHY undergoes decontamination in orbit.

The BrO VCD maps shown in figures 6.13 are calculated using a stratospheric AMF profile based on balloon-borne UV/Visible spectroscopic measurements of *Pundt et*

70

al., 2002 (see figure 4.4). It has already been pointed out in section 4 that the main error source of the nadir BrO columns is the uncertainty in the AMF's. Satellite nadir measurements are much less sensitive to BrO in the lower troposphere (for low albedo surfaces – but sensitivity is high for surfaces covered by sea ice) than in the stratosphere [*Afe et al.*, 2004]. Hence, BrO contributions from the lower troposphere will therefore be underestimated, while BrO over bright clouds might be slightly overestimated. The spectral analysis and a possible bias from the irradiance spectrum used also contribute to the overall error, which is estimated to be ~20% at mid and high latitudes and ~30% in the tropics.

The daily VCD maps from GOME and SCIAMACHY from the 16th – 18th September 2002 are shown below (*Figure 6.13*). An ASM solar reference spectrum recorded on 15th December 2002 was used as an absorption-free background in the absence of daily-distributed solar spectrum products for the determination of SCIAMACHY VCD's on these days. Maximum and persistent enhancements in total BrO VCD's were observed by both instruments at various locations especially on the edge of the Antarctic continent close to the sea ice south of the Weddell Sea (*black triangles*) and in the proximity of the Ross Ice Shelf (*black spheres*).
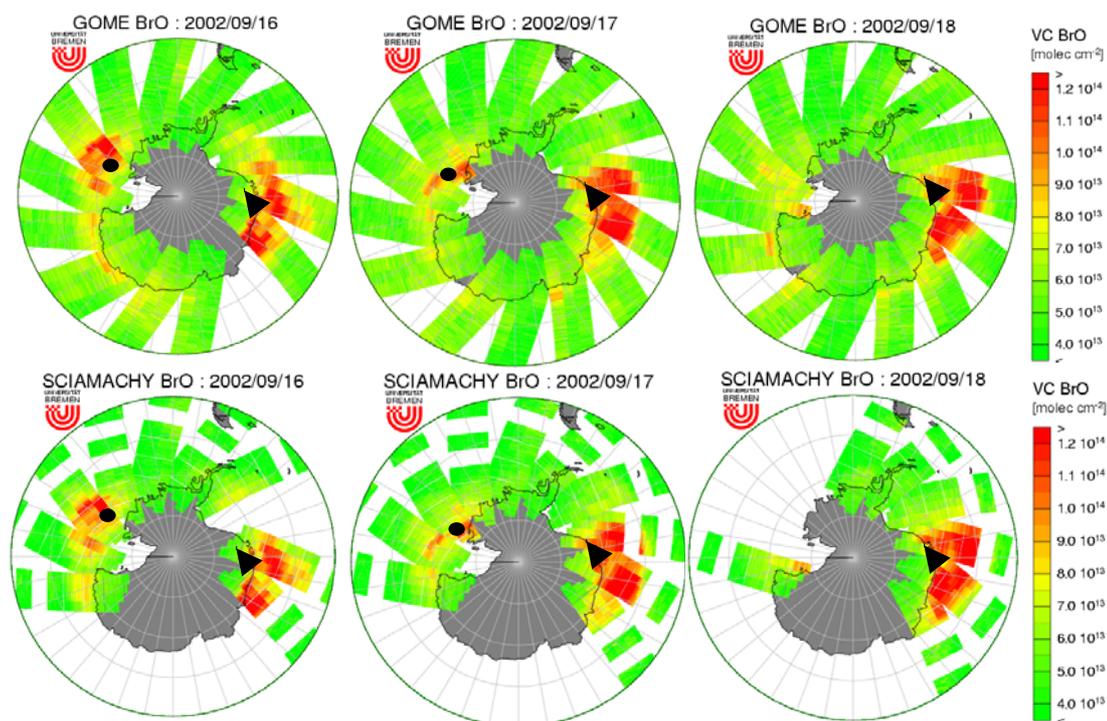
Figure 6.13: Antarctic Polar Spring BrO from GOME and SCIAMACHY for the 16th – 18th of September 2002. Both instruments mutually capture BrO explosion events on the separate days. The green colors represent typical 'background' values mainly located in the stratosphere and in the free troposphere. BrO hotspots (black ovals and triangles) are in yellow, orange and red indicate high boundary layer mixing ratios of BrO that are located above and near sea ice/frost flowers. Data gaps in between SCIAMACHY orbits are due to limb observations of the atmosphere. However, the huge gaps in the SCIAMACHY coverage is as a result of sparsely distributed data at these times.

For the monthly mean plots from January 2003 till year 2005 (*Figure 6.16*), an ASM solar irradiance spectrum taken each day at noon is used as an absorption-free background. This was done to avoid offsets in the determination of the SCIAMACHY

BrO SCD's as a daily noon solar reference spectrum results in smoother columns relative to employing a single solar irradiance spectrum where variations can be seen in BrO columns over the Atlantic (*Figure 6.15*).

$$y = 0.62862*10^{13} + 0.91793\ x$$

Error

A   = 0.05019

B   = 0.00686

R	SD	N	P
0.98102	0.39081	701	< 0.0001

$$y = 0.8657*10^{13} + 1.00349\ x$$

Error

A   = 0.02544

B   = 0.00337

R	SD	N	P
0.99621	0.20898	677	< 0.0001
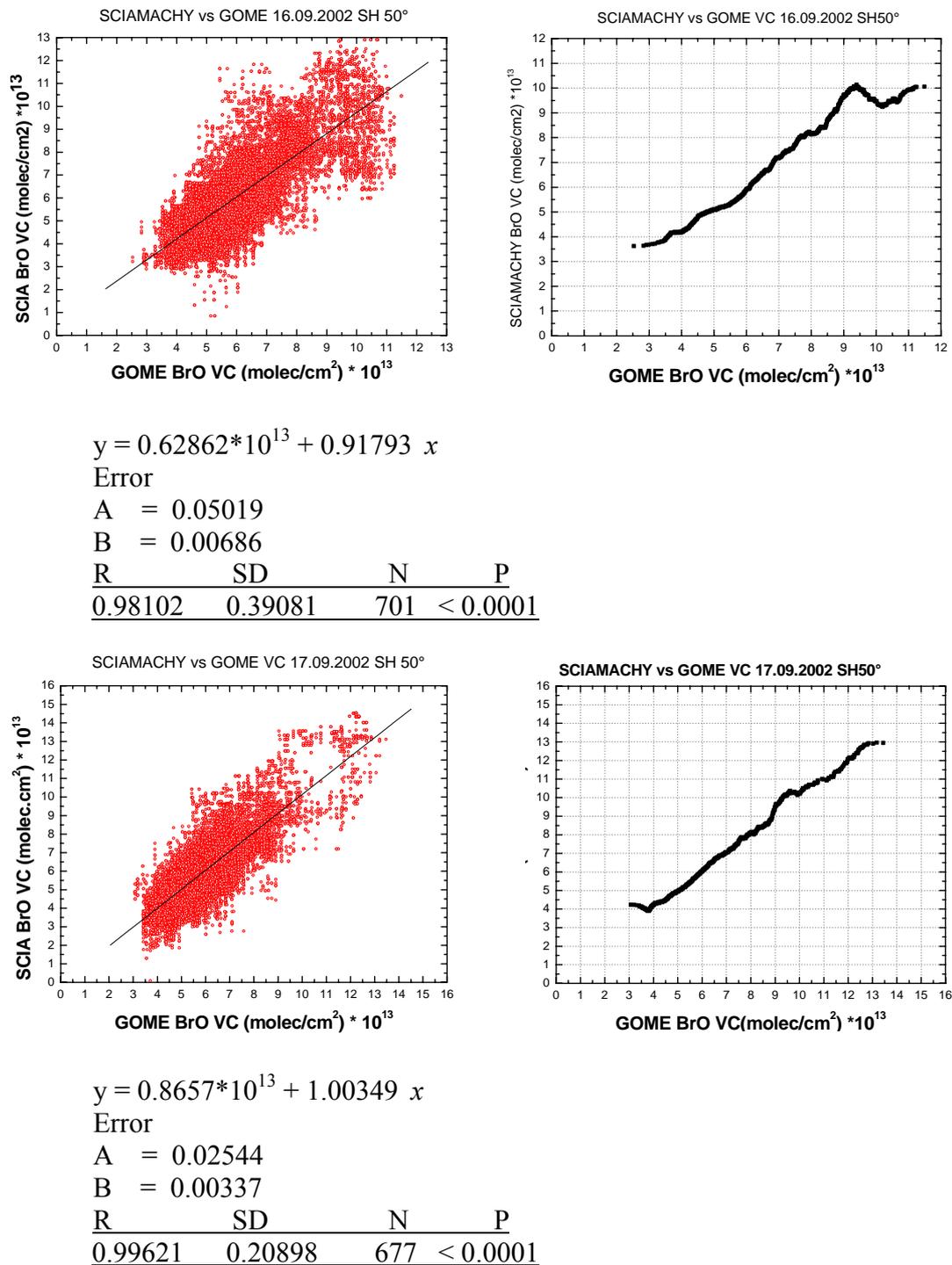
Figure 6.14: Correlation plots of all available raw data (restricted to a southern hemispheric latitude of 50°) from SCIAMACHY VCD's on the 16th and 17th September 2002 plotted against corresponding GOME pixels. The data are in very good agreement (except for the disagreement at high BrO VCD on the 16th which may be due to the influence of changing cloud cover within the 30-minute time difference in measurements between GOME and SCIAMACHY) for the separate days. Note that the influence of clouds in the retrieval is not accounted for in this correlation plots.
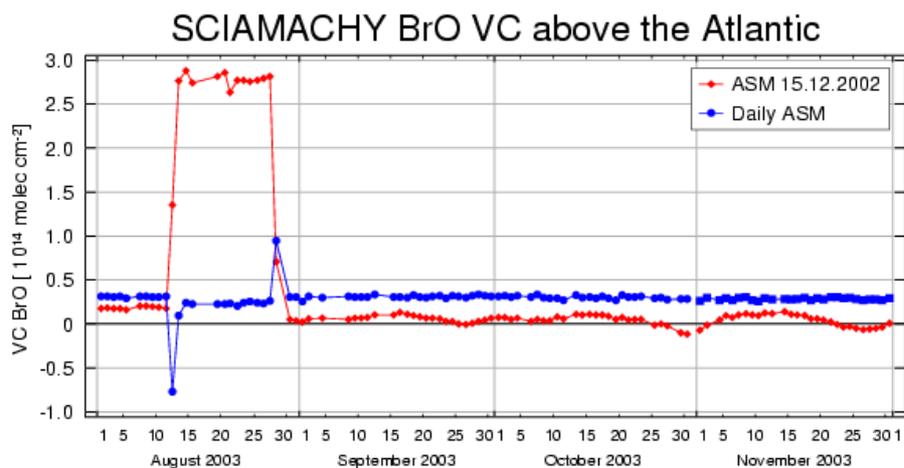
Figure 6.15: SCIAMACHY VCD variation over the Atlantic from the 1st of August 2003 till the end of November 2003. Use of a daily noon ASM solar irradiance spectrum results in smoother vertical columns (blue line) whereas employing a single solar reference spectrum results in variations that are uncharacteristic of BrO column behaviour over the Atlantic (expectedly constant background values).

Large tropospheric BrO columns are observed in polar spring of every year in both hemispheres from SCIAMACHY (*Figure 6.16*). Earliest indications for BrO enhancements are found from January for the northern hemisphere and from July in the southern hemisphere. In particular the areas over and around the Hudson Bay, Canada stretching east to the Caspian Sea is a persistent and recurring source of BrO explosion in the Arctic boundary layer. These events have already been reported in previous publications from measurements made from the GOME instruments (*Wagner and Platt,* 1998; *Wagner*, 1999; *Richter et al.,* 1998, 1999, 2002]). In the northern hemisphere the BrO distribution is centred over the pole (March, April and May) whereas it is distributed in a ring-like formation over and around the edges of Antarctica (from August to December). The difference in BrO distribution in both polar hemispheres is related to differences in sea ice distribution and the processes on sea ice and frost flowers that release bromine into the atmosphere [*Kaleschke et al.,* 2004].

Global Monthly mean Maps of BrO VCD's
Year 2003

SCIAMACHY BrO VC, January 2003

SCIAMACHY BrO VC, February 2003

SCIAMACHY BrO VC, March 2003

SCIAMACHY BrO VC, April 2003

SCIAMACHY BrO VC, May 2003

SCIAMACHY BrO VC, June 2003

SCIAMACHY BrO VC, July 2003

SCIAMACHY BrO VC, August 2003

VC BrO
[molec cm⁻²]

74

SCIAMACHY BrO VC, September 2003

SCIAMACHY BrO VC, October 2003

SCIAMACHY BrO VC, November 2003

SCIAMACHY BrO VC, December 2003

VC BrO
[molec cm⁻²]

**Global Monthly mean Maps of BrO VCD's
Year 2004**

SCIAMACHY BrO VC, January 2004

SCIAMACHY BrO VC, February 2004

VC BrO
[molec cm⁻²]

SCIAMACHY BrO VC, March 2004

SCIAMACHY BrO VC, April 2004

SCIAMACHY BrO VC, May 2004

SCIAMACHY BrO VC, June 2004

SCIAMACHY BrO VC, July 2004

SCIAMACHY BrO VC, August 2004

SCIAMACHY BrO VC, September 2004

SCIAMACHY BrO VC, October 2004

VC BrO
[molec cm^{-2}]

$\geq 8.0\ 10^{13}$
$7.5\ 10^{13}$
$7.0\ 10^{13}$
$6.5\ 10^{13}$
$6.0\ 10^{13}$
$5.5\ 10^{13}$
$5.0\ 10^{13}$
$4.5\ 10^{13}$
$4.0\ 10^{13}$
$<$

Global Monthly mean Maps of BrO VCD's
Year 2005

Figure 6.16: SCIAMACHY BrO measurement maps in total VCD's. Monthly averages from January 2003 to February 2005, highlighting areas of intense BrO explosion events in the polar boundary layer (i.e. areas shaded in yellow orange and red). Typical background values are represented in green. These BrO explosion events are attributed to sea ice distribution and processes on sea ice and frost flowers that release bromine into the atmosphere.

6.6 Resolution Effects: SCIAMACHY and GOME BrO VCD's

As the GOME and SCIAMACHY nadir measurements are very similar, the SCIAMACHY data are well suited to continue the existing GOME time series that basically ended their global coverage in June 2003. However, instrumental issues as well as the difference in sampling (SCIAMACHY has only half the coverage per day of GOME) and the difference is resolution can have an impact on the retrieved tropospheric BrO columns. The spatial resolution of SCIAMACHY measurements is generally determined by the signal-noise-ratio requirements i.e. detector filling-in and the maximum available data rate [*Noel et al.,* 2000].

Issues:

- GOME ground scenes have a coarse spatial resolution (typically: 320×40 km^2) with respect to SCIAMACHY (typically: 30×60 km^2) leading to smearing out of details in GOME tropospheric measurement map scenes.
- SCIAMACHY data should improve the accuracy of retrievals for better identification of local sources of polar BrO events and simplify the difference between source and local transport events.
- Improved SCIAMACHY spatial resolution implies a higher probability of finding cloud-free scenes which is relevant to retrieval of tropospheric trace gas constituents

Evidence for the improved spatial resolution in SCIAMACHY nadir measurements have been demonstrated for some tropospheric trace gases, in particular NO_2 and SO_2 [e.g. *Richter et al*., 2004; *Beirle et al*., 2004; *Afe et al.*, 2004]. This has also been demonstrated for atmospheric BrO [*Afe et al.*, 2005].

Resolution Effects: Individual days:
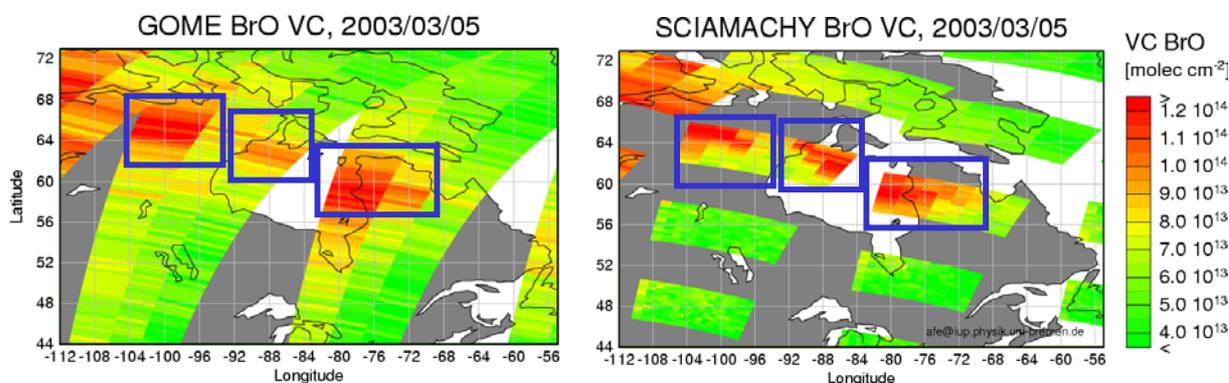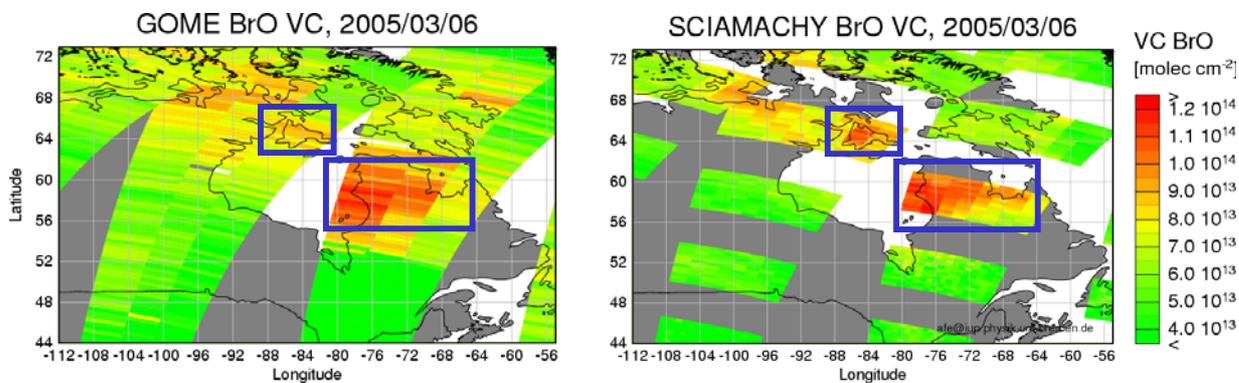
Figure 6.17: Resolution effects of GOME and SCIAMACHY BrO nadir observations over the Hudson Bay and near environs in the Arctic. SCIAMACHY ground scene observations of BrO events are more detailed with respect to GOME. Note for example, the high BrO event over areas of the Southampton Island (highlighted over the smaller rectangular box on the 6th March 2005), which might be due to transport.

Resolution Effects: Monthly Mean:
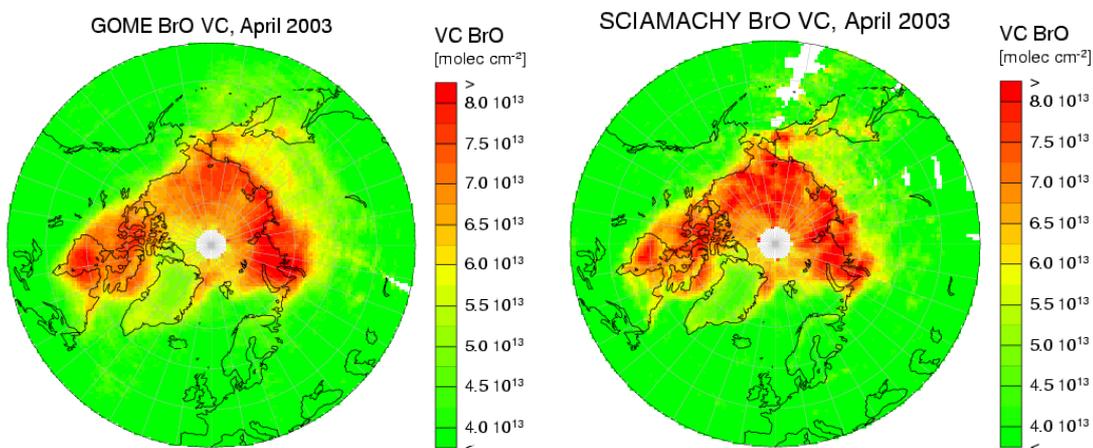
Figure 6.18: Resolution Effects - Comparison of the BrO monthly mean VCD for April 2003 over the Arctic for GOME and SCIAMACHY. The results are mutually consistent for both instruments despite the limitations of (a) a 30-minute time difference for every overpass between both instruments; (b) For SCIAMACHY, half the data sets/coverage are lost to limb observations; (c) The impact of cloud cover was not accounted for in this retrieval.

Chapter 7

Application of Satellite Observations of BrO

7.1 Investigating the Significance of BrO Emission from Volcanic Eruptions

Volcanic eruptions are a major source of SO_2 and some reactive halogen species notably HCl and HF. Recent studies have however observed the presence of large amounts of BrO with tight correlation to SO_2 in a volcanic plume by ground-based spectroscopic measurements. In this PhD thesis, upper limits of BrO columns have been estimated for a number of volcanic eruptions observed in measurements made by the satellite instruments - GOME and SCIAMACHY. The results obtained for the eruptions covered by satellite overpasses over the Etna, Nyamuragira, Popocatepetl, and Reventador volcanoes show no correlation between enhanced volcanic SO_2 during large eruptions and the corresponding BrO columns. Evidence for BrO enhancement was also not found in the vicinity of the Soufrière Hills volcanoes. The possible reasons for the differences between ground-based and satellite observations are considered.

Introduction

Explosive volcanic activity is characterized by the ejection of pyroclastic material, the outpour of magma, ash, dust and gases into the atmosphere [*Bates and Jackson*, 1980]. In particular SO_2 and HCl are known to be injected into the troposphere and sometimes directly into the stratosphere. In the troposphere, the HCl is rapidly removed by uptake on aerosols and subsequent wet deposition, while SO_2 is oxidized to H_2SO_4 in the gas phase by the OH and in the liquid phase by H_2O_2 [e.g., *Finlayson-Pitts and Pitts*, 2000]. In the stratosphere, volcanic eruptions can lead to a dramatic increase in the aerosol content, which has a large impact on the radiative balance and on stratospheric chemistry.

The detection of BrO from a volcanic plume of the Soufrière Hills volcano on Montserrat, 23rd –31st May 2002, by the use of a ground-based sequential scanning MAX-DOAS instrument [*Bobrowski et al.,* 2003] indicates a source of bromine for the atmosphere, which was previously considered negligible. In that study, slant column densities of BrO (up to 2.0E15 molecules.cm^{-2}) were reported, corresponding to mixing ratios of 1 ppb. BrO was closely correlated with SO_2 and a BrO:SO_2 molar ratio of 0.001 inferred. Based on these measurements, a total source strength of 350 t yr^{-1} of reactive bromine was derived for this volcano.

A global estimate of 30,000 t Br yr^{-1} from all volcanoes was obtained assuming the observed Br:S ratio to be representative for all volcanoes. This has important

consequences for the atmosphere because reactive halogen species, in particular bromine, are known to be effective in the catalytic depletion of ozone in both the stratosphere and the troposphere. Bromine is central to the destruction of boundary layer ozone in polar spring as was confirmed by ground-based spectroscopic measurements [e.g., *Hausmann and Platt*, 1994] and remote sensing measurements from the Global Ozone Monitoring Experiment GOME [*Wagner and Platt*, 1998; Richter et al., 1998]. Finally, the satellite data and comparison with ground-based measurements indicate the presence of a tropospheric background of about 1 ppt BrO of unknown origin [*Van Roozendael et al.*, 2002].

SO_2 from volcanic eruptions has also been observed from space [e.g., *Krueger et al., 1995*; *Eisinger and Burrows*, 1998], but the retrieval of volcanic BrO from satellite measurements has never been reported in literature before. In order to assess how representative the measurements of *Bobrowski et al.*, 2003 are on a global scale, more measurements of volcanic plumes are needed. Satellite measurements offer a unique opportunity to measure SO_2 and BrO globally.

This thesis reports on simultaneous satellite borne measurements of volcanic SO_2 and the corresponding columns of BrO retrieved during or after eruptions in the vicinity of volcanic vent sites of the Etna (37.73°N, 15.00°E, summit elevation 3350 m, a shield volcano), Popocatépetl (19.02°N, 98.62°W, summit elevation 5426 m; a stratovolcano) the Soufrière Hills volcanoes (16.72°N, 62.18°W, summit elevation 1052 m; a stratovolcano), Reventador (0.07S, 77.65W, summit elevation 3562 m; a stratovolcano) and Nyamuragira (1.41°S, 29.20°E, summit elevation 3058 m; a shield volcano). Measurements from the GOME and SCIAMACHY instruments are used, the latter providing superior spatial resolution.

7.1.1 Data Analysis

As mentioned in the previous chapter, data analysis of GOME and SCIAMACHY BrO is identical with the GOME and SCAMACHY BrO fitted in the 344.7-359.0 nm and 336.0-347.0 nm spectral range respectively.

The SCIAMACHY SO_2 fitting interval is similar to the GOME SO_2 fitting interval at 315.0-327.0 nm.

To isolate the effect of the volcanic emissions and remove the impact of stratospheric contributions and possible instrumental offsets, a normalization was applied to both the BrO and SO_2 measurements. This was done by the subtraction of the columns retrieved from a neighboring orbit well away from the volcanic plume taken at the same latitude on the same day. Thus, any impact of the volcanic eruption would show up as deviation from zero. To focus on the volcanic effects, only data within ±3° of latitude to the base of SO_2 enhancement were considered. No attempt was made to convert the measured slant column densities (SCD's) to vertical columns as the focus is on the correlation between SO_2 and BrO behavior which is largely unaffected by radiative transfer (*see section 7.1.4*).

7.1.2　Results

All GOME measurements from 1996–June 2003 have been investigated and a total of 54 orbits directly above or in the near vicinity of the Etna, Nyamuragira, Popocatépetl, Reventador and the Soufrière Hills volcanoes were selected based on the large SO_2 columns observed (SCD > 3.0E17 molecules.cm^{-2})[*]. Using the same SO_2 threshold, SCIAMACHY measurements over 33 scenes of SO_2 emissions from the volcanic vent sites mentioned above from August 2002–January 2004 have also been chosen for this study. The data analysis described above has been applied to all selected measurements from both instruments and some results are listed in Table 1.

Soufrière Hills Volcano
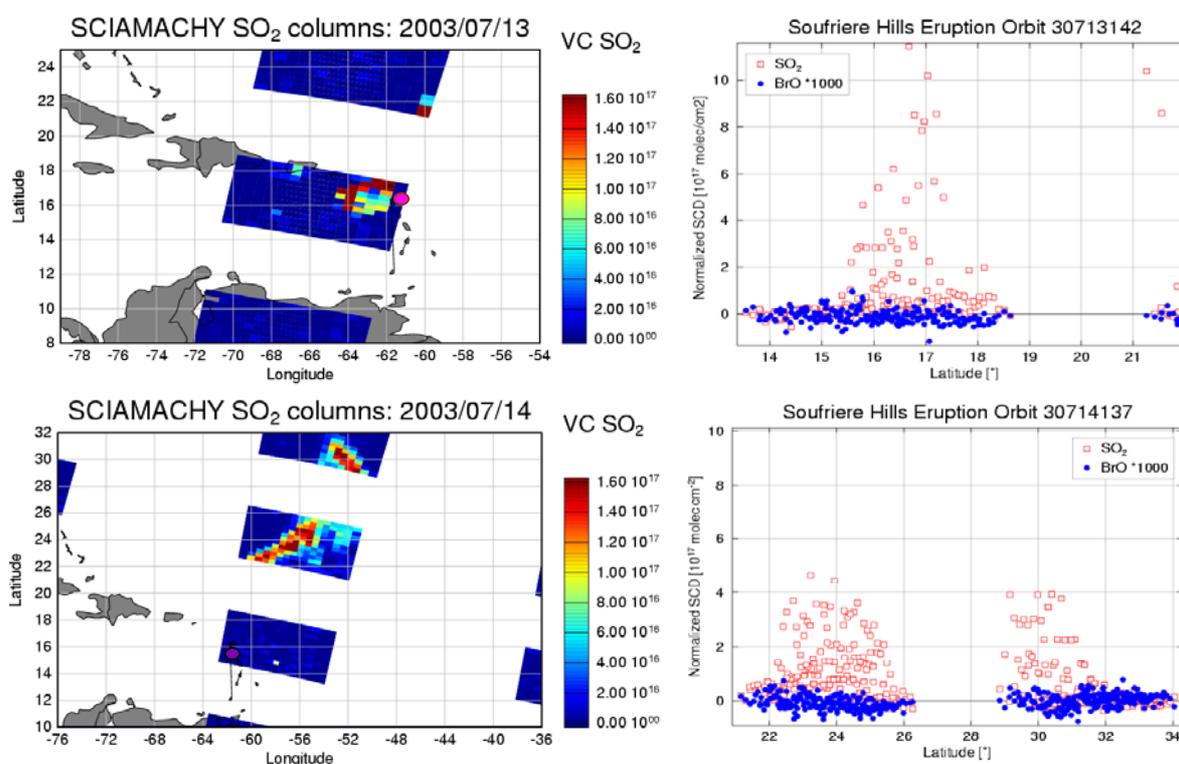
Figure 7.1: SCIAMACHY overpasses over the Soufrière Hills volcano (marked in oval sphere) on the 13th and 14th July 2003 and corresponding slant column densities of SO_2 and BrO (factored out by 1000) compared for these eruptions. The volcanic plume recorded on the 13th coincided with the volcano location and a **BrO:SO_2** of **8.29×10^{-5}** was calculated. The ageing volcanic plume on the 14th July recorded a **BrO:SO_2** of **1.68×10^{-4}** and the plume could be tracked several hundreds of kilometers from the volcanic site in a northeasterly direction.

Table 1: List of Volcanoes Investigated in This Study and Normalized Maximum Slant Column Densities (for specific Days of Satellite Overpass)

Volcano	Summit Elevation (m)	GOME Max. SCD SO_2 (molec./cm^2)	SCIA Max. SCD SO_2 (molec./cm^2)	GOME Max. SCD BrO (molec./cm^2)	SCIA Max. SCD BrO (molec./cm^2)	Day of overpass
Etna	3350	< 3E17	3.05E17	5.20E13	9.28E13	31.10.2002
Nyamuragira	3058	4.69E17	3.49E17[a]	5.47E13	1.4E14[a]	31.07.2002
Popocatépetl	5465	1.01E18	(no data)	8.09E13	(no data)	19.12.2000
El Reventador	3562	3.14E17	4.21E17	3.19E13	1.08E14	21.11.2002
Soufrière Hills I	1052	6.18E17	(no data)	6.79E13	(no data)	30.07.2001
Soufrière Hills II	1052	(no data)	1.04E18	(no data)	9.48E13	13.07.2003

[a] Maximum of emissions missed due to gaps in the SCIAMACHY coverage.

As an example, Figure 7.1 depicts a SCIAMACHY overpass over the Soufrière Hills Volcano on Montserrat on the 13th (top panel) and the 14th of July 2003 (bottom panel) a day of explosive eruptions following low seismic activity. Heavy falls of ash clouds, dust, and rock fragments rose up to about 12-15 km above sea level in altitude and pyroclastic flows impacted the area between the Tar River valley and Spanish point (http://www.volcano.si.edu/reports/usgs/). Eruptive activity was so intense that the lava dome structure collapsed (figure 7.2) leaving the landscape extensively modified.
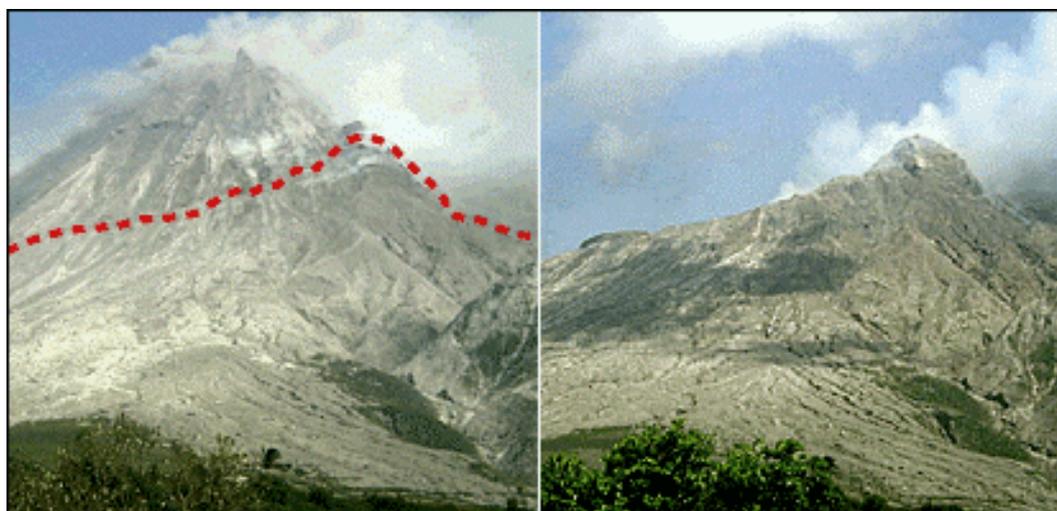
Figure 7.2: The Soufrière Hills volcano on Montserrat before and after blowing it's top in July 2003 *(Image courtesy of MVO/BGS/Government of Montserrat)*

SCIAMACHY observed a large volcanic plume measuring about 200×300 km^2 on the 13th July 2003 coinciding with the summit location of the Soufrière Hills volcano. Maximum slant column densities (SCD's) of 9.48×10^{13} molecules/cm^2 and 1.04×18 molecules/cm^2 were obtained for the SCIAMACHY columns of BrO and SO_2 (BrO:SO_2 ~ 8.29×10^{-5}). The ageing plume measured by SCIAMACHY on the 14th

July 2003 had already moved several hundreds of kilometers northeast. A BrO:SO_2 ~ $1.68{\times}10^{-4}$ was calculated based on the maximum SCD's recorded (see figure 7.1). Whilst the SO_2 is clearly enhanced, no evidence of BrO enhancement was seen in the volcanic plume by either of the instruments despite observations being made directly over the source of volcanic activity. Similar results were obtained for the other volcanoes studied (see Figure 7.3 as examples for the Nyamuragira volcano, in the Democratic Republic of the Congo) where maximum SCD's of $5.5{\times}10^{-17}$ molecules cm^{-2} and $8.7{\times}10^{-13}$ molecules cm^{-2} were obtained for the SCIAMACHY columns of SO_2 and BrO respectively. Both instruments saw no evidence of BrO enhancement.

Nyamuragira Volcano
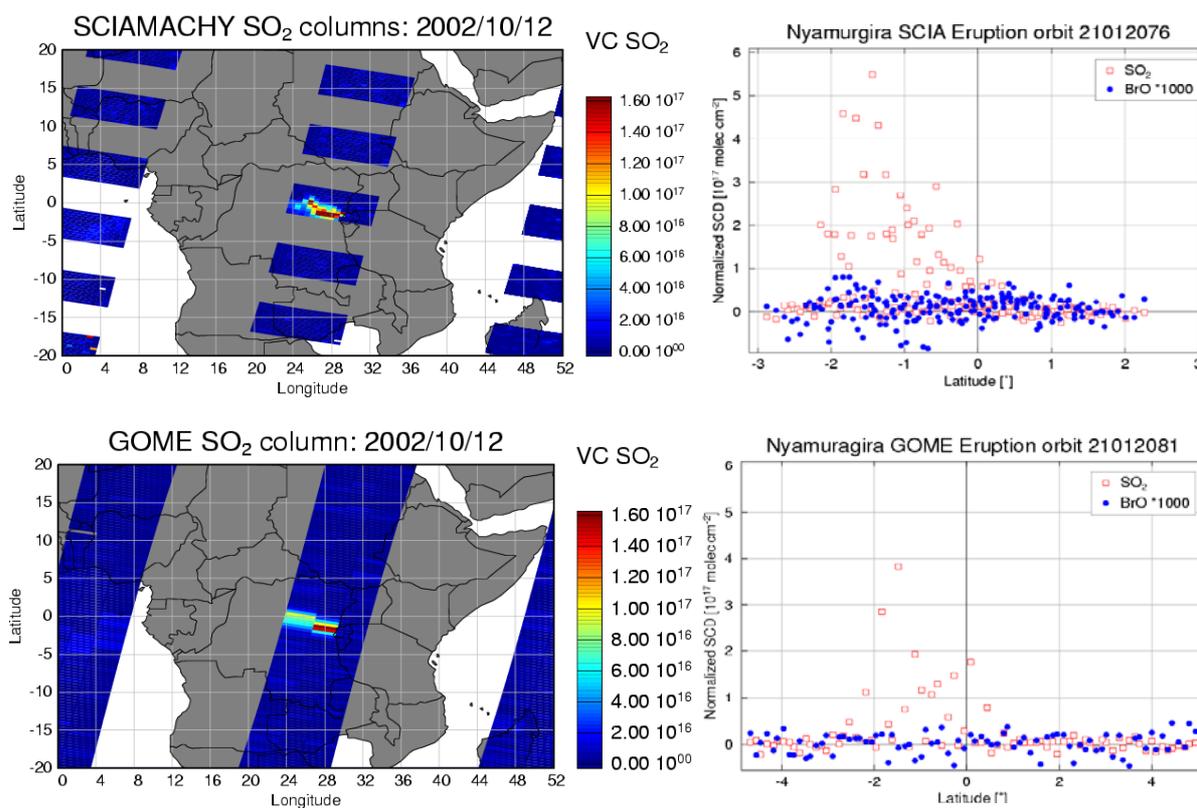
Figure 7.3: SCIAMACHY and GOME measurement maps of volcanic SO_2 from the Nyamuragira volcano on the 12th October 2002 and corresponding slant column densities of SO_2 and BrO (factored out by 1000), compared for this eruption. A BrO:SO_2 upper limit of **$1.58{\times}10^{-04}$** was obtained from SCIAMACHY data for this eruption.

In Figure 7.4, all selected BrO and SO_2 columns over the Nyamuragira volcano are shown for GOME and SCIAMACHY respectively. This site was selected as it has the largest number of direct overpasses in the satellite records. Again, there is no indication for a correlation between the measured BrO and SO_2 columns from either instrument. Similar results are obtained for all the volcanoes studied.

In summary, analysis of all 87 scenes of volcanic activity with high SO_2 columns gives no indication for a correlation between SO_2 and BrO columns. Upper limits for the BrO:SO_2 ratios are determined by the BrO uncertainties and were smaller by factors of 5–20 than the value expected from the emission ratio given by *Bobrowski et al. 2003*.
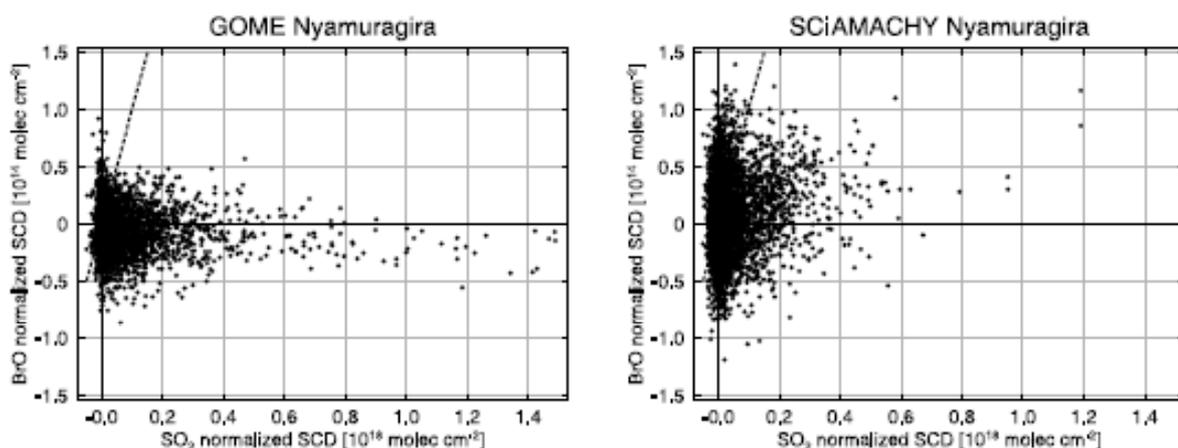
Figure 7.4: Normalized slant column densities of volcanic SO_2 and corresponding BrO from GOME (January 1996–June 2003) and SCIAMACHY data (August 2002–January 2004) for the Nyamuragira volcano. The dashed line is the correlation found by Bobrowski et al. [2003].

7.1.3 Discussion

Several possible explanations have been considered for the lack of correlation between corresponding columns of BrO and volcanic SO_2 in the satellite-based measurements. First, the sensitivity of the satellite BrO measurements has to be evaluated.
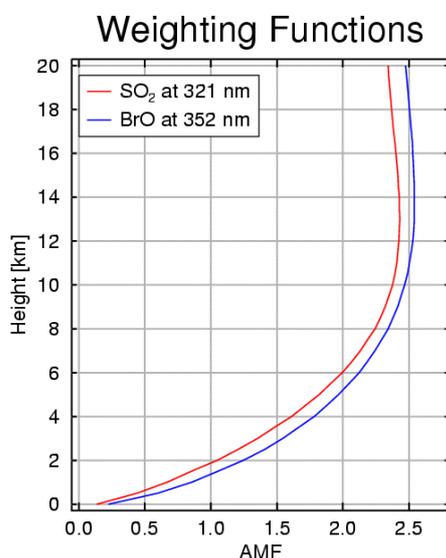
Figure 7.5: Sensitivity of satellite measurements of SO_2 and BrO: Airmass factor variation as a function of altitude for 40° solar zenith angle, 5% albedo and a cloud-free scene.

Figure 7.5 shows a typical sensitivity of the BrO and SO_2 satellite measurements as a function of altitude. The air mass factor is similar for both species and above 5 km depends only slightly on altitude, facilitating the detection of volcanic plumes. Given a detection limit of about 5.0×10^{13} (7.5×10^{13}) molecules cm^{-2} for BrO and assuming a

85

layer of 1 km thickness at 3 km altitude, a BrO mixing ratio of 20 (30) ppt should be detectable for GOME (SCIAMACHY) if sustained throughout a single ground scene. Although part of the gases emitted by the volcano are probably hidden from the satellite measurements within and below the plume, this shielding effect should be similar for BrO and SO_2 and not affect the observed ratio.

Secondly, the large measurement pixels of the satellite instruments result in a dilution effect that could mask high but localized BrO concentrations. For example, a plume of 1 km width and 30 km length covers only 1/400th of a GOME pixel and even at large local BrO concentrations could be below the detection limit. As SCIAMACHY ground scenes are smaller than those of GOME by a factor of 7–14, one would expect the effect to be smaller, but there is no significant difference in the results from the two instruments apart from the larger scatter in SCIAMACHY data. The latter is a result of the shorter integration time that improves spatial resolution at the expense of signal to noise ratio.

Thirdly, the lifetime of BrO within the volcanic plume must be taken into consideration. The expected lifetime for BrO in this situation is very short (a few minutes based on HO_2 loss mechanism estimate) hence satellite measurements might not be able to observe BrO in an aging plume in contrast to local ground-based measurements. Depending on the exact composition of the plume, rapid recycling on the abundant aerosols could also extend the BrO lifetime in analogy to polar boundary layer events where BrO can be observed over hours and days [*Wagner et al.*, 2001].

A last possibility is a difference in Br:S ratio for eruptive emissions. In-situ observations at the Stromboli volcano indicate that HCl to SO_2 ratios are much larger during quiescent degassing [*Aiuppa and Federico*, 2004]. This might explain the lack of enhancement in BrO during major eruptions, since Cl and Br are strongly correlated in terrestrial reservoirs [*Bureau et al.*, 2000].

In the case of the Soufrière Hills volcano, one additional explanation is that BrO is produced and destroyed within the volcanic plume that is mixing with marine air. Clearly, detailed chemical models are needed to investigate these possibilities in a quantitative manner.

7.1.4 Conclusions

All available data from the GOME instrument (1996–June 2003) and over one year of SCIAMACHY measurements (August 2002–January 2004) have been analyzed for SO_2 and BrO slant columns during episodes of large volcanic emissions. Results obtained from a total of 87 retrievals for both instruments for direct satellite overpasses over the Etna, Nyamuragira, Popocatepetl, Reventador and the Soufrière Hills volcanoes with SO_2 slant columns above a threshold of 3.0E17 molecules cm^{-2} provide no indication of enhancement of BrO during large volcanic eruptions. Taking into account the sensitivity of the satellite instruments and their detection limit, an upper limit of 20(30) ppt BrO in a 1 km thick layer at 3 km can be determined for a completely filled GOME (SCIAMACHY) ground scene, but much larger mixing ratios could be present in more localized plumes. No correlation could be found between the SO_2 and the BrO columns observed.

These findings are in contrast to those of the ground-based measurements of *Bobrowski et al.* [2003] at least with respect to the volcanic eruptions studied.

One explanation for the lack of signal in the satellite data is a short lifetime of BrO in the volcanic plume, either through loss by reaction with, for example HO_2 or through

heterogeneous reactions on and in the volcanic aerosol present in the plumes. Another possibility is a fundamental difference in BrO to SO_2 ratio for the large eruptions studied here when compared to degassing as observed by Bobrowski et al. It can however also not be excluded that the observations by Bobrowski et al. were specific to the volcano and or the event studied. Extrapolation from this event to determine a global emission of bromine therefore requires caution. This study focused on individual large eruptions and did not attempt to quantify the effect of degassing. Clearly more ground-based measurements combined with satellite observations and studies of BrO chemistry are needed to resolve the differences between the ground-based and satellite observations of SO_2 and BrO.

This will enable the significance of the bromine input to the atmosphere for volcanic degassing and eruptions to be established.

7.2 Influence of Frost flowers on Tropospheric Halogen Chemistry

In section 2.2, a brief overview of frost flowers as one of the dominant sources of sea salt aerosols in both polar hemispheres was discussed. The aerosols produced from frost flowers have been identified in Antarctic ice cores and at coastal stations due to the depleted sulphate-to-sodium ratio compared to the aerosol originating from the open ocean [*Wagenbach et al.,* 1998; *Rankin et al.,* 2002; *Rankin and Wolff,* 2003]. Frost flowers grow on newly formed sea ice from a saturated water vapour layer. It has been speculated that they could be involved in processes that cause severe ozone depletion events in the polar boundary layer during polar sunrise. These events have been found to be associated with elevated amounts of inorganic bromine compounds [*Barrie et al.,* 1998; *McConnell et al.,* 1992; *Foster et al.,* 2001]. These can be explained by heterogeneous autocatalytic reactions occurring on salt-laden ice surfaces, which exponentially increase the reactive gas phase bromine i.e. 'bromine explosion' (*see figure 2.4*). The main source of bromine over the open oceans in the MBL outside the polar regions was identified to be sea salt aerosol generated by sea spray on the ocean surface [*Vogt et al.,* 1996; *Sander et al.,* 2003]. However ground-based stations [e.g. *Ridley et al.,* 2003; *Frieß et al.,* 2004] as well as space-borne spectrometers, GOME and SCIAMACHY have observed maximum BrO amounts over areas covered by sea ice during polar sunrise [*Richter et al.,* 1998; *Wagner and Platt;* 1998; *Van Roozendael et al.,* 2004]. Because frost flowers exhibit enhanced salinities and bromide ion concentrations triple that of bulk seawater [*Perovich and Richter-Menge,* 1994], their potential role in ozone depletion events in polar spring has been raised [*Rankin et al.,* 2002].

In a recent publication, *Kaleschke et al.,* 2004 provided a method to associate regions potentially covered with frost flowers as prerequisites for the bromine explosion events in polar spring. Tropospheric BrO was analyzed from the GOME and SCIAMACHY instruments using the DOAS retrieval algorithm. The sea ice coverage and concentration was determined from analyses of the thermal microwave emission measured by the Special Sensor Microwave Imager (SSM/I) onboard the Defense Meteorological Satellite Program (DMSP) platform using the ASI algorithm [*Kaleschke et al.,* 2001; *Maslanik and Stroeve,* 2003]. The ASI algorithm takes advantage of the higher polarisability of a specularly reflecting water surface compared to the more diffusely reflecting sea ice surface [*Kaleschke et al.,* 2001;

Kern et al., 2003]. A one-dimensional thermodynamic model was developed to calculate the frost flower coverage. Two model input parameters, which are the surface air temperature and the open water fraction, were obtained from the numerical weather predicting reanalysis data (NCEP/NCAR) and from satellite passive microwave instruments respectively. The model yields a maximum percentage area potentially covered by frost flowers for a given surface air temperature and the total potential frost flower (PFF) area is obtained by weighting the total area with the new ice fraction (*see Kaleschke et al., 2004 for more details*).

7.2.1 Comparison of Model Results and BrO Data

Some examples of the resulting PFF and BrO data are shown in Figures 7.6, 7.7, and 7.8. The overall mechanism requires the release of bromine atom precursors, either directly on the frost flower surface or within the aerosol.
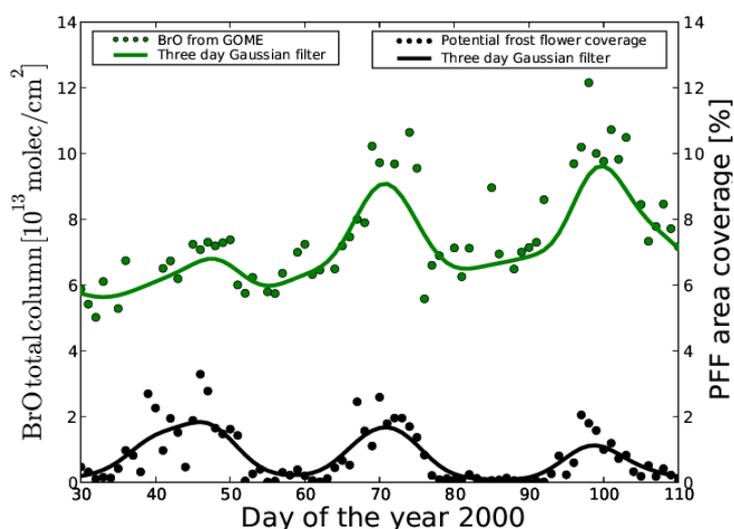
Figure 7.6: A time series of GOME BrO total column for the year 2000 (green dots) and corresponding PFF area coverage (black dots) for an area over the Hudson Bay, Canada (depicted in red box below in figure 7.7). A three-day Gaussian filter was applied and the result displayed in corresponding color-coded solid lines [Kaleschke et al., 2005, *unpublished manuscript*].
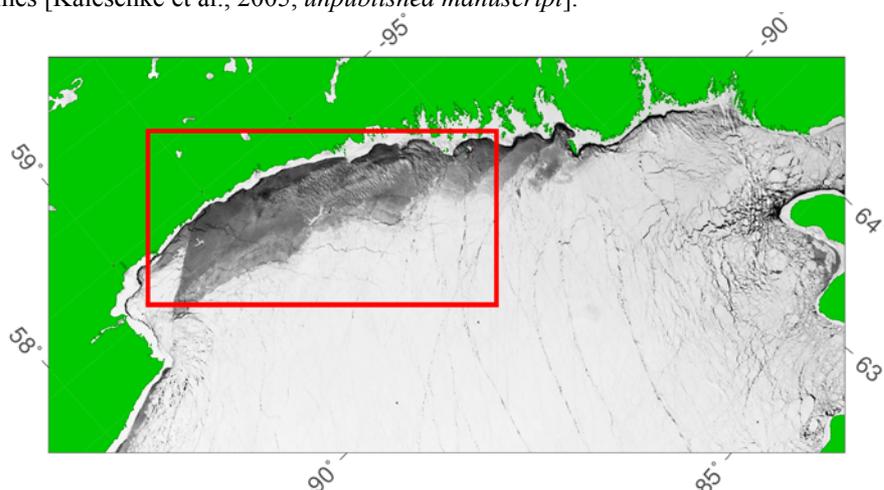
Figure 7.7: MODIS image (channel 1, 250 m resolution) over the area of investigation on the 5th of March 2003. Offshore winds frequently cause the opening of the ice near the coastline – the main

reason for new ice production during the cold season. A thin ice area of ~20,000 km^2 can be identified by it's darker appearance. The first 120 days (January-April) have been analyzed for the indicated area for the years 2000-2003. For this period, daily average values of the PFF coverage have been calculated [Kaleschke et al., 2005, *unpublished manuscript*].

GOME:

Figure 7.7: Example of total PFF coverage (green stars) and enhanced BrO (red isolines) over the Hudson Bay for 11th March 2001. The green stars mark the endpoints of 24 hr forward air trajectories starting at frost flower area coverage of greater than 0.4%, sampled every 187 km. The PFF field was smoothed to 300 km spatial resolution to match the GOME resolution. The 24hr air trajectories start at PFF greater than 1% sampled every 62.5 km. The red isolines correspond to enhanced BrO amounts of 8.8×10^{13} molec/cm^2, which is the mean (6.2) plus two standard deviations (1.3). The isolines are broken due to the data gaps in the GOME coverage. [Images from *Kaleschke et al.,* 2004].
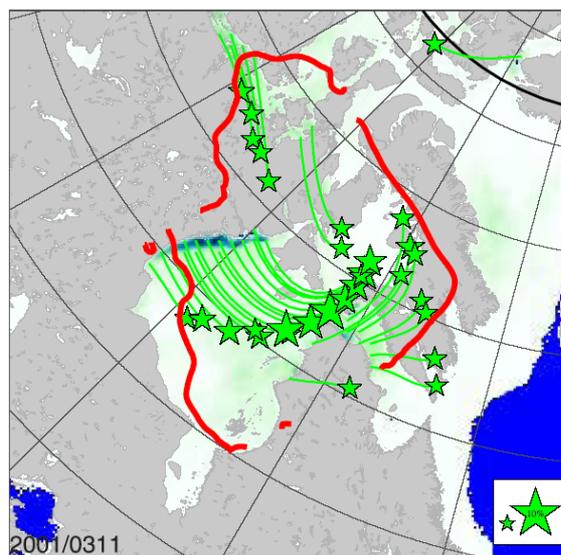
Figure 7.8: Area of potential frost flower coverage (green stars) and enhanced BrO amounts (red isolines) over the Antarctic Ocean. The maximum values of two consecutive days are shown: from the 28th – 29th and the 29th – 30th August 1997 for PFF and BrO respectively. Symbols and lines are similar to figure 7.6, but the PFF coverage is displayed color-coded. The total PFF coverage is proportional to the size of the stars. Two stars of 1% and 10% area coverage are shown in the lower right corner for comparison. The red isolines corresponds to the enhanced BrO amounts of 3.6×10^{13} molec/cm^2, which is the mean (1.4) plus one standard deviation (2.2). The black circle indicates the almost dark latitudes (solar zenith angle > 80°) where there is not enough light available for photochemistry. Sea ice covered regions are presented in white and the open ocean is coloured in blue. [Images from *Kaleschke et al.,* 2004].
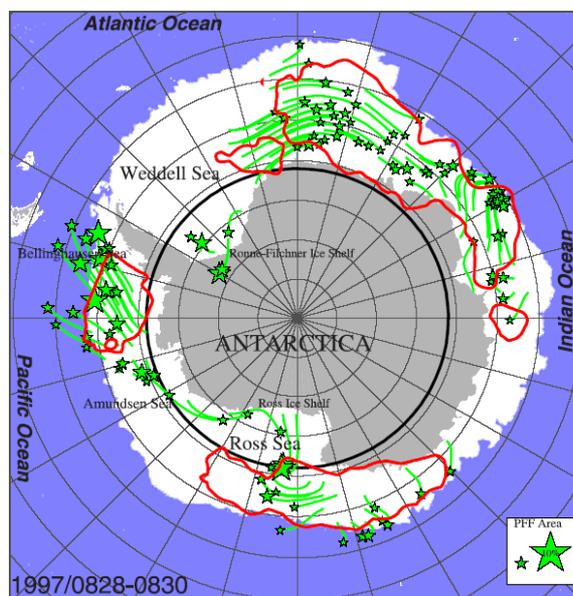
SCIAMACHY:
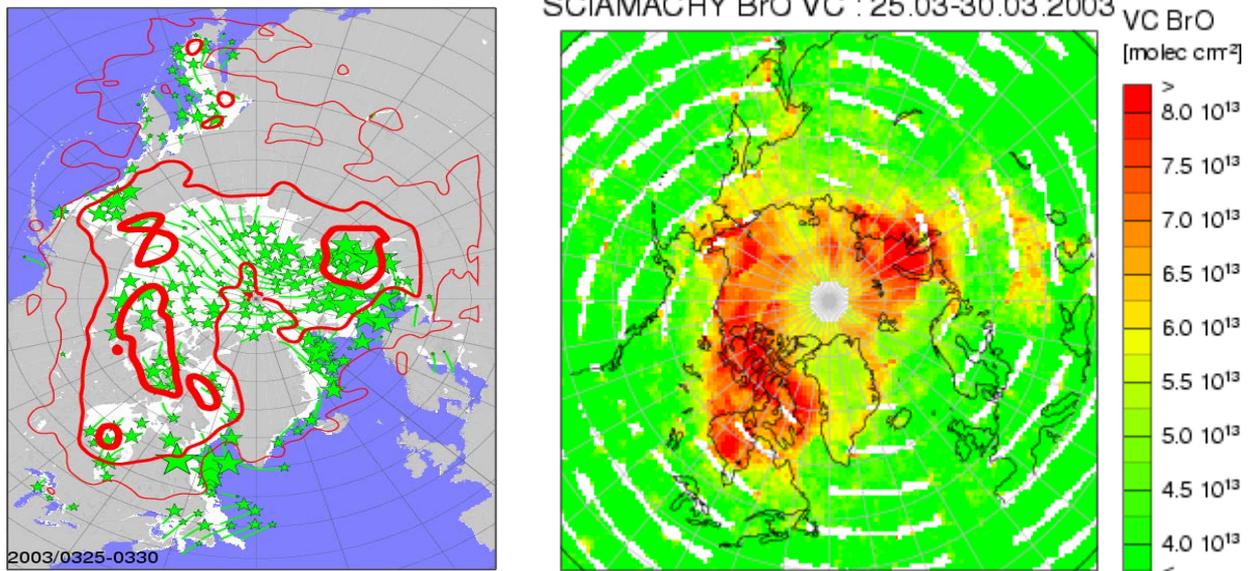
Figure 7.9: (Left) Example of total PFF coverage (green stars) and enhanced atmospheric BrO (red isolines) averaged to measurements from SCIAMACHY data from the 25th – 30th March 2003 over the Arctic. SCIAMACHY data were smoothed around a scale of 500 km radius. The green asterisks mark the terminator points of 24hr trajectories, which were computed on the basis of the surface wind from weather model data (NRA). The corresponding SCIAMACHY BrO Vertical column densities averaged over the same time period is depicted on the right panel. Most of the forward air trajectories starting at regions with high PFF values hit the enhanced BrO areas. The potential sea ice flower coverage is the theoretical upper border of the surface coverage, which is computed from the measured sea ice concentration and the air temperature by means of a physical model. The quite rough approximation of the BrO sources describes well the spatial and temporal (not represented here) situation of the measured BrO maxima.

Summary and Outlook

In this PhD thesis, an optimized scheme for the DOAS retrieval of atmospheric bromine monoxide (BrO) has been developed and applied to satellite data from the nadir UV/Visible spectral range of the SCIAMACHY instrument using algorithms similar to that employed for the retrieval of atmospheric BrO from the GOME satellite data. Due to the impact of residual structures in the channel 2 spectral range of the SCIAMACHY instrument, a UV-shifted window (336.0-347.0 nm) has been searched and tested on SCIAMACHY data and the resulting BrO slant column densities (SCD's) from the DOAS analysis found to be consistent to corresponding GOME BrO evaluations obtained in the traditional spectral range (344.7-359.0 nm). From these evaluations, total vertical column densities (VCD's) of atmospheric BrO have been calculated from the slant columns by applying a stratospheric Airmass Factor (AMF) that has atmospheric BrO profile information obtained from balloon-borne UV/Visible spectroscopy.

BrO explosion events in both the Arctic and Antarctic polar regions have been captured by SCIAMACHY (from August 2002 till date) and these have been compared to corresponding GOME BrO events. The results of BrO evaluations from both instruments are similar and found to be very consistent. Hence, SCIAMACHY measurements of atmospheric BrO are well suited to continue the existing GOME BrO time series which basically ended the their global coverage in June 2003.

Searching for Volcanic BrO over active volcanoes

Volcanic eruptions are a large source of SO_2 and some reactive halogen species, in particular, HCl and HF. But in a recent publication by *Bobrowski et al.*, 2003, using a MAX-DOAS ground-based instrument, large amounts of BrO (up to 2.0E15 molec./cm^2, corresponding to about 1 ppb) was observed in the degassing vents of a volcanic plume of the Soufrière Hills volcanoes and BrO closely correlated to SO_2. A BrO to SO_2 ratio of 0.001 was then inferred i.e. (BrO:SO_2=1:1000).

As SCIAMACHY ground scenes offers a higher spatial resolution (typically: 30 × 60 km^2) compared to that of GOME (typically: 320 × 40 km^2), a potential exists for the retrieval of improved tropospheric columns (or signals) of enhanced BrO events. Hence, within the THALOZ project, all available BrO data from the SCIAMACHY and GOME instruments were searched for volcanic BrO using the high SO_2 SCD's observed as an indicator over explosive activities of the Nyamuragira, Reventador, Etna, Popocatepetl, and the Soufrière Hills volcanoes. The results obtained from the satellite measurements do not provide any indication for BrO enhancement in the plumes emanating from active volcanoes. Upper limits of BrO:SO_2 of 8.29×10^{-5} and 1.68×10^{-4} was calculated directly above and at large distances from the Soufrière Hills volcano. Hence, no correlation could be found between the large SO_2 and corresponding BrO columns observed. These findings are in apparent disagreement to the ground-based observations of *Bobrowski et al.*, 2003.

Taking into account the sensitivity of the satellite measurements and their detection limit, an upper limit of ~20 (30 ppt) BrO in a 1 km thick layer at 3 km altitude can be determined for a completely filled GOME (SCIAMACHY) ground scene.

Several reasons have been given for the lack of BrO signal in the satellite data:

- A short lifetime of BrO in the volcanic plume, either through loss by reaction with, for example HO_2 radical or heterogeneous reaction on and in the volcanic aerosols present in the plumes. The ground-based measurements are taken close to the source, whereas, the satellite averages over a large area (and thereby over time). However, recent measurements have shown significant BrO concentrations at about 25 km from the volcano, indicating that the lifetime cannot be very short.

- Another possibility is a fundamental difference in the BrO to SO_2 ratios for the large eruptions studied here when compared to degassing as observed by Bobrowski et al. In fact, there are indications from some measurements that $Cl:SO_2$ ratios are different for eruptive events, and a similar effect could exist for Br.

- It can however also not be excluded that the observations by Bobrowski et al. were specific to the volcano and or the event studied. Hence, extrapolation from this event to determine a global emission of bromine therefore requires caution.

This study focused on individual large eruptions over active volcanoes and did not attempt to quantify the effects of degassing. Clearly more ground-based measurements combined with satellite observations and studies of BrO chemistry are needed to resolve the differences between the satellite and ground-based observations of SO_2 and BrO. This will enable the significance of the bromine input to the atmosphere for volcanic degassing and eruptions to be established.

Frost flowers as a source of BrO

From both GOME and SCIAMACHY nadir observations combined with ground-based measurements, it is known, that large plumes of elevated BrO form in each polar spring in both hemispheres in the boundary layer. The original source of the bromine is seawater, and once the bromine is inside of aerosols, an autocatalytic release of bromine will rapidly increase BrO concentrations. However, the exact mechanism of the transfer of bromine from sea water to the atmosphere is not yet clear. One recent hypothesis is that frost flowers are involved in this process. Frost flowers form on fresh, thin ice of frozen leads and polynyas at very low temperatures, and are known to exhibit enhanced salinities and bromide ion concentrations of about three times of that of bulk seawater. They also have very large surface areas, and are easily blown away, being one of the largest sources of sea salt aerosol in the Antarctic. In polar regions, frost flowers form on a regular basis and potentially, they could act as the missing link to transfer Br into the atmosphere.

To test the connection between frost flowers and BrO, a study was undertaken that combines remote sensing of BrO and ice cover with meteorological data and a simplified model of frost flower growth. First, sea ice coverage was estimated using SSM/I measurements. Then, a model computes the area where frost flower formation is possible based on ice and temperature data (Potential Frost Flower area PFF), and 24-hour forward trajectories are calculated. These data are then compared to areas of enhanced BrO as observed from GOME. The results demonstrated very good agreement between BrO plumes and air originating from frost flower areas. It should be noted that the autocatalytic release of BrO is based on photolysis and therefore frost flowers in the dark region are not directly linked to enhanced BrO. Similar

correlations are found for the Northern hemisphere, indicating that frost flowers play in fact a key role in polar bromine explosion events. Confirmation for the hypothesis comes from recent ship-borne measurements within a frost flower field close to Spitsbergen, where rapid ozone destruction was observed on a day when high BrO was detected from satellite in the same area.

Future works

- Derivation of improved tropospheric columns of BrO through the limb-nadir-matching technique from SCIAMACHY, which should effectively separate the tropospheric and stratospheric excess of BrO.

- Further improvements in the DOAS SCIAMACHY analysis of BrO will be possible through the use of better cross-sections of atmospheric trace gases with high spectral resolution.

- Interference from some trace gases e.g. HCHO (and possibly the unknown absorber) in the DOAS fitting procedure affects significantly BrO retrieval in both the GOME and SCIAMACHY measurements. More work needs to be done to account for these effects within the retrieval.

- SCIAMACHY as well as the existing GOME data provide a unique opportunity for the validation of global 3D-chemical transport models.

Acknowledgements

References

Abbatt, J. P. D. and G. C. G. Waschewsky, 'Heterogeneous interactions of HOBr, HNO_3, O_3 and NO_2 with deliquescent NaCl aerosols at room temperature', *J. Phys. Chem*. A, **102**, 3719 – 3725, (1998).

Abbatt, J. P. D. and Molina, M. J., 'The heterogeneous reaction HOCl + HCl $\rightarrow$ Cl_2 + H_2O on ice and nitric acid trihydrate: reaction probabilities and stratospheric implications', *Geophys. Res. Lett.*, **19,** 461-464, (1992).

Afe, O. T., A. Richter, B. Sierk, F. Wittrock and J. P. Burrows, 'BrO Emission from Volcanoes - a Survey using GOME and SCIAMACHY Measurements', *Geophys. Res. Lett.*, **31**, L24113, doi:10.1029/2004GL020994, (2004).

Afe, O. T., A. Richter, L. Kaleschke and J. P. Burrows, 'Effects of improved spatial resolution in SCIAMACHY BrO measurements compared to GOME BrO retrievals' Geophysical Research Abstracts, *Oral presentation, proceedings of the European Geosciences Union*, EGU05-A-08843, **7**, 08843, (2005).

Aiuppa, A., and C. Federico, 'Anomalous magmatic degassing prior to the 5th April 2003 paroxysm on Stromboli', *Geophys. Res. Lett.*, **31**, L14607, doi:10.1029/2004GL020458, (2004).

Alicke, B. K., K. Hebestreit, J. Stutz, and U. Platt, Iodine oxide in the marine boundary layer, *Nature*, **397**, 572–573, (1999).

Aliwell, S. R., R. L. Jones, and D. J. Fish, 'Mid-latitude observations of the seasonal variation of BrO, 1, Zenith-sky measurements', *J. Geophys. Res.*, **24**, 1195– 1198, (1997).

Aliwell, S. R., et al., 'Analysis for BrO in zenith-sky spectra: An intercomparison exercise for analysis improvement', *J. Geophys. Res.*, **107**(D14), doi: 10.1029/2001JD000329, (2002).

Allan, B. J., J. M. C. Plane, and G. McFiggans, Observations of OIO in the remote marine boundary layer, *Geophys. Res. Lett.*, **28**, 1945–1948, (2001).

Andreae, M. O., Atlas, E., Harris, G. W., Helas, G., de Kock, A., Koppmann, R., Maenhaut, W., Mano, S., Pollock, W. H., Rudolph, J., Scharffe, D., Schebeske, G., and Welling, M.: 'Methyl halide emissions from savanna fires in Southern Africa', *J. Geophys. Res.*, **101D**, 23 603–23 613, (1996).

Andreae, M. O., Andreae, T. W., Annegarn, H., Beer, J., Cachier, H., le Canut, P., Elbert, W., Maenhaut, W., Salma, I., Wienhold, F. G., and Zenker, T.: 'Airborne studies of aerosol emissions from savanna fires in southern Africa: 2. Aerosol chemical composition', *J. Geophys. Res.*, **103D**, 32 119–32 128, (1998).

Arpag, K. H., P. V. Johnston, H. L. Miller, R. W. Sanders, and S. Solomon, 'Observations of the stratospheric BrO column over Colorado, 40° N', *J. Geophys. Res.,* **99**, 8175–8181, (1994).

Balzer, W., D. Loyola, B. Aberle, E. Mikusch, T. Ruppert, C. Schmid, S. Slijkhuis, R. Spurr, W. Thomas, A. Tuerk, and M. Wolfmueller: 'Ground Segment for ERS-

2/GOME Sensor at the German D-PAF', IGARSS '96, Lincoln, Nebraska, May (1996).

Barrie, L. A., Bottenheim, J. W., Schnell, R. C., Crutzen, P. J. & Rasmussen, R. A., 'Ozone destruction and photochemical reactions at polar sunrise in the lower Arctic atmosphere', *Nature* **334**, 138-141, (1988).

Bates, R. L., and J. A. Jackson, Glossary of Geology, *2nd ed., Am. Geol. Inst.*, Falls Church, Va., (1980).

Bedjanian, Y., G. Le Bras, and G. Poulet, 'Kinetic study of the Br + IO, I + BrO, and Br + I$_2$, Reactions. Heat of Formation of the BrO Radical', *Chem. Phys. Lett.,* **266**, 233-238 (1997b).

Bedjanian, Y., G. Le Bras, and G. Poulet, 'Kinetics and Mechanisms of IO + BrO Reaction', *J. Phys. Chem. A,* **102**, 10501-10511 (1998).

Bednarz, F.: 'Global Ozone Monitoring Experiment (GOME) Users Manual', *European Space Agency Publi. Div,* Noordwijk, The Netherlands, (1995).

Behnke, W., Krüger H. -U., Scheer V. and Zetzsch C., 'Formation of ClNO$_2$ and HONO in the presence of NO$_2$, O$_3$ and wet NaCl aerosol, *J. Aerosol Sci.,* **23**, 933-936, (1992).

Behnke W., Scheer V. and Zetzsch C., 'Formation of ClNO$_2$ and HNO$_3$ in the presence of N$_2$O$_5$ and wet pure NaCl- and wet mixed NaCl/Na$_2$SO$_4$-aerosol', *J. Aerosol Sci.,* **24**, 115-116, (1993).

Behnke, W., Scheer, V., and Zetzsch, C.: Production of BrNO$_2$, Br$_2$ and ClNO$_2$ from the reaction between sea spray aerosol and N$_2$O$_5$, *J. Aerosol Sci.*, **25**, S277–S278, (1994).

Behnke, W., Elend, M., Krüger, U., and Zetzsch, C.: 'The influence of NaBr/NaCl ratio on the Br−-catalyzed production of halogenated radicals', *J. Atmos. Chem.*, 34, 87–99, (1999).

Beirle, S., U. Platt, R. von Glasow, M. Wenig, and T. Wagner, 'Estimate of nitrogen oxide emissions from shipping by satellite remote sensing', *Geophys. Res. Lett.*, **31**, L18102, doi:10.1029/2004GL020312, (2004).

Bekki, S., 'Oxidation of Volcanic SO$_2$: 'A Sink for Stratospheric OH and H$_2$O', *Geophys. Research Lett.,* 22, 913-916, (1995).

Bjarnason, G. G., Ö. E. Rögnavaldsson, T. I. Sigfússon, T. Jakobsson, and B. Thorkelsson, 'Total ozone variations at Reyjavik since 1957', *J. Geophys. Res.,* **98**, 23 059-3 077, (1993).

Bobrowski, N., G. Hönninger, B. Galle and U. Platt, 'Detection of bromine monoxide from a volcanic plume', *Nature,* **423**, 273-276, (2003).

Bobrowski, N., G. Hönninger, I. Louban, O. I. Whaba and U. Platt, 'Reactive bromine and chlorine chemistry in volcanic plumes', *Geophys. Res. Abstracts*, **Vol. 7**, 09102, *Proceedings of the European Geosciences Union*, Vienna, Austria, (2005).

Bodeker, G. E., J. C. Scott, K. Kreher, R. L. McKenzie, 'Global ozone trends in potential vorticity coordinates using TOMS and GOME intercompared against the Dobson network: 1978 – 1998', *J. Geophys. Res.,* **106** (D19), 23029-23042, 10.1029/2001JD900220, (2001).

Bogumil, K., J. Orphal und J. P. Burrows, 'Reference spectra of atmospheric relevant trace gases measured with the SCIAMACHY PFM satellite spectrometer', *Proc. 5th Colloquium, Atmospheric Spectroscopy Applications* (ASA), Reims, France, (1999).

Bojkov, R. D., and V. E. Fioletov, Changes of the lower stratospheric ozone over Europe and Canada, *J. Geophys. Res.*, **102**, 1337–1347, (1997).

Bottenheim J. W., Gallant A. C. and Brice K. A., 'Measurements of NO_y species and O_3 at 82° N latitude', *J. Geophys. Res.*, **13**, 113 –114, (1986).

Bovensmann, H., J. P. Burrows, M. Buchwitz, J. Frerick, S. Noël, V. V. Rozanov, K. V. Chance, and A. H. P. Goede, 'SCIAMACHY - Mission objectives and measurement modes', *J. Atmos. Sci.*, **56, (2)**, 127-150, (1999).

Brinkmann, R.T.: 'Rotational Raman scattering in planetary atmospheres, *Astrophys. J.* **154**, 1087-1093, (1968).

Bureau, H., H. Keppler, and N. Métrich, 'Volcanic degassing of bromine and iodine: Experimental fluid/melt partitioning data and applications to stratospheric chemistry', *Earth Planet. Sci. Lett.*, **183**, 51– 60, (2000).

Burkholder, J. B., Curtius, J., Ravishankara, A. R., and Lovejoy, E. R.: Laboratory studies of the homogeneous nucleation of iodine oxides, *Atmos. Chem. Phys. Discuss.*, **3**, 4943–4988, (2003).

Burrows, J. P., E. Hölzle, A. P. H. Goede, H. Visser, and W. Fricke, 'SCIAMACHY—Scanning Imaging Absorption Spectrometer for Atmospheric Chartography', *Acta Astronaut.,* **35**, 445–451, (1995).

Burrows, J. P. , A. Dehn, B. Deters, S. Himmelmann, A. Richter, S. Voigt and J. Orphal, Atmospheric Remote-Sensing Reference Data from GOME: 1. Temperature-Dependent Absorption Cross Sections of NO_2 in the 231-794 nm Range, *JQSRT,* **60***, 1025, (1998).

Burrows, J. P., A. Richter, A. Dehn, B. Deters, S. Himmelmann, S. Voigt, and J. Orphal, 'Atmospheric remote -sensing-reference data from GOME: 2. Temperature-dependent absorption cross sections of O_3 in the 231-794 nm range', *JQSRT,* **61***, 509-517, (1999).

Burrows, J. P., M. Weber, M. Buchwitz et al., 'The Global Ozone Monitoring Experiment (GOME): Mission concept and first scientific results', *J. Atmos. Sci.,* **56**, 151– 175, (1999).

Bussemer, M., 'Der Ring-Effekt: Ursachen und Einfluß auf die spektroskopische Messung stratosphärischer Spurenstoffe', *Diploma thesis, University of Heidelberg,* (1993).

Carpenter, L. J., Sturges, W. T., Penkett, S. A., Liss, P. S., Alicke, B., Heibestreit, K., and Platt, U.: Short-lived alkyl iodides and bromides at Mace Head: links to macroalgal emissions and halogen oxide formation, *J. Geophys. Res.*, 104, 1679–1689, (1999).

Carpenter, L. J., Malin, G., Liss, P. S., and Küpper, F. C.: Novel biogenic iodine-containing trihalomethanes and other short-lived halocarbons in the coastal East Atlantic, *Glob. Geochem. Cycles*, **14**, 1191–1204, (2000).

Chance, K, 'Analysis of BrO Measurements from the Global Ozone Monitoring Experiment,' *Geophys. Res. Lett.,* **25***,* 3335-3338, (1998).

Chapman, S., 'On Ozone and Atomic Oxygen in the Upper Atmosphere', *Philos. Mag*. **10**, 369-383, (1930).

Crutzen P. J. et al., 'Biomass burning as a source of atmospheric trace gases: CO, H_2, N_2O, NO, CH_3Cl and COS', *Nature,* **282***,* 253-256, (1979).

Crutzen, P. J., and F. Arnold, 'Nitric acid cloud formation in the cold Antarctic stratosphere: A major cause for the springtime 'ozone hole,' *Nature,* **324**, 651–655, (1986).

Crutzen and Andreae, 'Biomass burning in the tropics: Impact of atmospheric chemistry and biogeochemical cycles', *Science,* **250***,* 1669-1678, (1990).

Davis, D., J. Crawford, S. Liu, S. McKeen, A. Bandy, D. Thornton, F. Rowland, and D. Blake, 'Potential Impact of Iodine on Tropospheric levels of Ozone and other Critical Oxidants', *J. Geophys. Res.*, **101**, 2135-2147, (1996).

DeMore, W. B. et al., 'Chemical kinetics and photochemical data for use in Stratospheric modeling', Evaluation number 12, *JPL Publ*. 97 - 4, (1997).

De Muer, D., and H. De Backer, 'Revision of 20 years of total ozone data at Uccle (Belgium): Fictitious Dobson ozone trends induced by sulfur dioxide trends', *J. Geophys. Res.*, **97**, 5921-5937, (1992).

De Smedt, I., M. Van Roozendael, T. Jacobs, 'Optimization of DOAS settings for BrO fitting from SCIAMACHY nadir spectra - Comparison with GOME BrO retrievals', *tech-note*, (2004).

Dobson, G. M. B., 'Forty years research on atmospheric Ozone at Oxford', *Appl. Opt.*, **7**, 387-405, (1968).

Domine, F., R. Sparapani, A. Ianniello and H. J. Beine, 'The origin of sea salt in snow on Arctic sea ice and in coastal regions', *Atmos. Chem. Phys.*, **4**, 4737–4776, (2004).

Dütsch, H. V., 'Ozone distribution in the atmosphere', *Can. J. Chem*., **52**, 1491–1504, (1974).

Ebinghaus, R., Kock, H.H., Temme, C., Einax, J.W., Lowe, A. G., Richter, A., Burrows, J.P. and Schroeder, W. H., 'Antarctic springtime depletion of atmospheric mercury' *Environ. Sci & Techno.*, **36**, pp.1238-1244, (2002).

Echalar, F., Gaudichet, F., Cachier, H., and Artaxo, P.: 'Aerosol emissions by tropical forest and savanna biomass burning: Characteristic trace element and fluxes', *Geophys. Res. Lett.*, **22**, 3039–3042, (1995).

Eisinger, M., and J. P. Burrows, 'Tropospheric sulfur dioxide observed by the ERS-2 GOME instrument', *Geophys. Res. Lett.,* **25**, 4177– 4180, (1998).

Fickert, S., J. W. Adams, and J. N. Crowley, 'Activation of Br_2 and BrCl via uptake of HOBr onto aqueous salt solutions', *J. Geophys. Res.*,**104**, 23 719 - 23 727, (1999).

Finlayson-Pitts, B. J. and James N. Pitts, 'Chemistry of the upper and lower Atmosphere: Theory, Experiments and Applications', *Academic Press,* (2000).

Entzian, G. and Peters, D. *Proc. Quad. Ozone Symp.*, Sapporo,

European Space Agency (ESA), 'The GOME Users Manual', edited by F. Bednarz, *ESA Publ. Div., Eur. Space Res.* and *Techn. Cent.*, Noordwijk, Netherlands, (1995).

Hood, L. L., Rossi, S. & Beulen, M. *J. Geophys. Res*. **104,** 23321–24339 (1999).

Fabry, C. and H. Buisson, 'L'absorption de l'ultraviolet par l'ozone et la limite due spectre solaire', *J. Phys. Paris,* **3**, 196-206, (1913).

Fan, S. M., and D. J. Jacob, 'Surface ozone depletion in Arctic spring sustained by bromine reactions on aerosols', *Nature*, **359**, 524– 552, (1992).

Farman, J. C., B. G. Gardiner, and J. D. Shanklin, 'Large losses of total ozone in Antarctica reveal seasonal ClO$_x$/NO$_x$ interaction', *Nature*, *315*, 207–210, (1985).

Ferlemann, F., Camy-Peyret, C., Harder, H., Fitzenberger, R., Hawat, T., Osterkamp, H., Perner, D., Platt, U., Schneider, M., Vradelis, P., Pfeilsticker, K., 'Stratospheric BrO profile measured at different latitudes and seasons. Measurement technique'. *Geophys. Res. Lett.* **25**, 3847–3850, (1998).

Finlayson-Pitts B. J. and Johnson S. N., 'The reaction of NO$_2$ with NaBr: Possible source of BrNO in polluted marine atmospheres, *Atmos. Environ.* **22**, 1107 − 1112, (1988).

Finlayson-Pitts, B. J., and J. N. Pitts Jr., 'Chemistry of the upper and lower atmosphere, in Theory, Experiments and Applications', Academic Press, New York, (2000).

Fish, D. J., and M. R. Burton, 'The effect of uncertainties in kinetic and photochemical data on model predictions of stratospheric Ozone depletion', *J. Geophys. Res.,* **102***, 25537-25542, (1997).

Fish, D. J., S. R. Aliwell, and R. L. Jones, 'Mid-latitude observations of the seasonal variation of BrO, 2, Interpretation and modeling study', *Geophys. Res. Lett.*, **24**, 1199– 1202, (1997).

Fitzenberger, R., H. Bösch, C. Camy-Peyret, M. P. Chipperfield, H. Harder, U. Platt, B. -M. Sinnhuber, T. Wagner, and K. Pfeilsticker, 'First profile measurements of tropospheric BrO', *Geophys. Res. Lett.*, **27**, 2921–2924, (2000).

Fleischmann, O. C., M. Hartmann, J. P. Burrows, and J. Orphal, 'New ultraviolet absorption cross-sections of BrO at atmospheric temperatures measured by time-windowing Fourier transform spectroscopy', *J. Photochem. Photobio., A: Chemistry*, *168*, 117-132, (2004).

Foster, K. L., R. A. Plastridge, J. W. Bottenheim, P. B. Shepson, B. J. Finlayson-Pitts, and C. W. Spicer, 'The role of Br-2 and BrCl in surface ozone destruction at polar sunrise', *Science*, **291**(5503), 471–474, (2001).

Francis, P., A. Maciejewski, C. Oppenheimer, C. Chaffin, and T. Caltabiano, 'SO$_2$:HCl ratios in the plumes from Mt. Etna volcano determined by Fourier Transform Spectroscopy, *Geophys. Res. Lett.* **22**, 1717-1720, (1995).

Frieß, U., M. Chipperfield, H. Harder, C. Otten, U. Platt, J. Pyle, T. Wagner, and K. Pfeilsticker, 'Intercomparison of measured and modeled BrO slant column amounts for the Arctic winter and spring 1994– 1995, *Geophys. Res. Lett.*, **26**, 1861– 1864, (1999).

Frieß, U., J. Hollwedel, G. König-Langlo, T. Wagner and U. Platt, 'Dynamics and chemistry of tropospheric bromine explosion events in the Antarctic coastal region', *J. Geophys. Res. Lett.,* **109**, D06305, doi: 10.1029/2003JD004133, (2004).

Garcia, R. R. and S. Solomon: A New Numerical Model of the Middle Atmosphere. 2. Ozone and related species, *J. Geophys. Res.*, **99**, 12937-12951, (1994).

Giese, B., F. Laturnus, F. C. Adams, and C. Wiencke, 'Release of Volatile Iodinated C1 - C4 Hydrocarbons by Marine Macroalgae from Various Climate Zones. *Environ. Sci. Technol.*, **33**, 2432 - 2439, (1999).

Gilles, M. K., A. A. Turnipseed, J. B. Burkholder, A. R. Ravishankara, and S. Solomon, 'Kinetics of the IO Radical. 2. Reactions of IO with BrO', *J. Phys. Chem. A,* **101***, 5526-5534, (1997).

Graedel, T. E. And W. C. Keene, 'The Tropospheric Budget of reactive Chlorine', *Global Biogeochem. Cycles,* **9***, 47-78, (1995).

Graedel, T. E. And W. C. Keene, 'The budget and cycle of Earth's natural Chlorine', *pure and appl. Chem.* 68, 1689-1697, (1996).

Grainger, J. F., and J. Ring: 'Anomalous Fraunhofer line profiles', *Nature*, **193**, 762, (1962).

Greenblatt G. D., J. J. Orlando, J.B. Burkholder, and A. R. Ravishankara, 'Absorption measurements of oxygen between 330 and 1140 nm', *J. Geophys. Res.,* **95**, 18577-18582, (1990).

Hanson, D. R., and Ravishankara, A. R., 'The reaction probabilities of $ClONO_2$ and N_2O_5 on polar stratospheric cloud materials', *J. Geophys. Res.,* **96,** 5081-5090, (1991).

Harder, H., et al., Stratospheric BrO profiles measured at different latitudes and seasons - atmospheric observations, *Geophysical Research Letters*, *25*(20), 3843–3846, (1998).

Harder, H., et al., Comparison of measured and modeled stratospheric BrO: Implications for the total amount of stratospheric bromine., *Geophysical Research Letters*, *27*(22), 3695–3698, (2000).

Harris, N. R. P., et al., 'Trends in stratospheric and free tropospheric ozone', *J. Geophys. Res.*, **102**, 1571–1590, (1997).

Harris, N., R. Hudson, and C. Phillips (Eds.), 'Assessment of trends in the vertical distribution of ozone', *SPARC Rep. 1, Ozone Res. and Monit. Proj. Rep.* **43**, *World Meteorol., Organ.*, Geneva, May 1998.

Haug, H., 'Raman-Streuung von Sonnenlicht in der Atmosphäre', *Diploma thesis*, University of Heidelberg, Germany, (1996).

Hausmann, M., and U. Platt, 'Spectroscopic measurements of bromine oxide and Ozone in the high Arctic during the Polar Sunrise Experiment 1992', *J. Geophys. Res.*, **99**, 25,399– 25,414, (1994).

Hebestreit, K., J. Stutz, D. Rosen, V. Matviev, M. Luria, and U. Platt, 'DOAS measurements of tropospheric bromine oxide in mid-latitudes', *Science,* **283** (5398) 55-57, (1999).

Hegels, E., et al., 'Global distribution of atmospheric bromine oxide from GOME on the earth observing satellite ERS-2', *Geophys. Res. Lett.*, **25**, 3127– 3130, (1998).

Hofmann, D. J., S. J. Oltmans, J. M. Harris, B. J. Johnson, and J. A. Lathrop, 'Ten years of ozonesonde measurements at the South Pole: Implications for recovery of springtime Antarctic ozone', *J. Geophys. Res.*, **102**, 8931–8943, (1997).

Holland, H. D., 'The Chemistry of the Atmophere and the Oceans', New York: *John Wiley and Sons*, (1978).

Hollandsworth, S. M., R. D. McPeters, L. E. Flynn, W. Planet, A. J. Miller, and S. Chandra, 'Ozone trends deduced from combined Nimbus 7 SBUV and NOAA 11 SBUV/2 data', *Geophys. Res. Lett.*, **22**, 905–908, (1995).

Holton, J. R., P. H. Haynes, M. E. McIntyre, A. R. Douglas, R. B. Rood, and L. Pfister, 'Stratosphere-Troposphere exchange', *Rev. of. Geophys.*, **33**, 403–439, (1995).

Hood, L. L., J. P. McCormack, and K. Labitzke, 'An investigation of dynamical contributions to mid-latitude ozone trends in winter', *J. Geophys. Res.*, **102**, 13,079 –13,093, (1997).

Howard, J. N., J. I. F. King, and P. R. Gast, 'Thermal Radiation', *Handbook of Geophys., Chap. 16*. Macmillan, New York, (1960).

Hönninger G. and Platt U., Observations of BrO and its Vertical Distribution during Surface Ozone Depletion at Alert, *Atmos. Environ.* **36**, 2481-2489, (2002).

Hönninger, G., N. Bobrowski, E. R. Palenque, R. Torrez, and U. Platt, 'Reactive bromine and sulfur emissions at Salar de Uyuni, Bolivia', *Geophys. Res. Lett.*, **31**, L04101, doi:10.1029/2003GL018818, (2004).

Ingham, T., D. Bauer, R. Sander, P. J. Crutzen, and J. N. Crowley, 'Kinetics and Products of the Reactions BrO + DMS and Br + DMS at 298 K', *J. Phys. Chem. A,* **103**, 7199-7209, (1999).

IPCC, Climate Change 2001: The Scientific Basis., in *Contribution of Working Group I to the Third Assessment Report of the Intergovernmental Panel on Climate Change*, edited by J. T. Houghton, Y. Ding, D. J. Griggs, M. Noguer, P. J. van der Linden, X. Dai, K. Maskell, and C. Johnson, Cambridge University Press, Cambridge, UK and New York, USA, (2001).

Jacob et al., 'The origin of ozone and NO_x in the tropical troposphere: A photochemical analysis of aircraft observations over the South Atlantic Basin', *J. Geophys Res*. **101**, 24235-24250, (1996).

Jaegle, L., D. Jacob, J., Brune W. H., Faloona, I. C., Tan, D., et al.: 'Ozone production in the upper troposphere and the influence of aircraft during SONEX: Approach of NO_x-saturated conditions, *Geophys., Res. Lett., **26***, 3081–3084*, (1999).

Jaenicke, R., 'Aerosol physics and chemistry, in Landolt-Börnstein: Zahlenerte und Funktionen aus Naturwissenschaften und Technik', Vol. **4b**, Springer, (1988).

Jimenez, J. L., Bahreini, R., Cocker, D. R., Zhuang, H., Varutbangkul, V., Flagan, R. C., Seinfeld, J. H., O'Dowd, C. D., and Hoffmann, T.: New Particle Formation from Photooxidation of Diiodomethane (CH_2I_2), *J. Geophys. Res.*, **108**, D10, 4318, doi:10.1029/2002JD002452, (2003a).

Jones, A. E. and Shanklin, J. D. 'Continued decline of total ozone over Halley, Antarctica since 1985', *Nature*, **376**, 409-411, (1995).

Johnston, P.V., 'Studies on the I_0-effect', *unpublished manuscript*, (1996).

Kaleschke, L., A. Richter, J. Burrows, O. Afe, G. Heygster, J. Notholt, A. M. Rankin, H. K. Roscoe, J. Hollwedel, T. Wagner, H. -W. Jacobi, 'Frost flowers on sea ice as a source of sea salt and their influence on tropospheric halogen chemistry', *Geophys. Res. Lett.,* **31**, L16114 doi: 1029/2004GL020655, (2004).

Kaleschke, L. and G. Heygster, 'Influence of Frost Flowers on the Ku-Band Backscatter for a Large Recurring Shore Polynya', *Unpublished manuscript* (2005).

Kane, R. P., Y. Sahai and C. Casiccia, 'Latitude dependence of the quasi-biennial oscillation and quasi-triennial oscillation characteristics of total ozone measured by TOMS', *J. Geophys. Res.*, **103**, 8477-8490, (1998).

Keene, W. C., A. A. P. Pszenny, D. J. Jacob, R. A. Duce, J. N. Galloway, J. J. Schultz-Tokos, H. Sievering, and J. F. Boatman, 'The geochemical cycling of reactive chlorine through the marine troposphere', *Global Biogeochemical Cycles,* **4**, 407-430, (1990).

Keene et al., 'A Measurement Technique for HCl and Cl_2 in the Marine Boundary Layer', *Environ. Sci. Technol.* **27**, 866-874, (1993).

Keene, W. C., D. J. Jacob, and S. -M. Fan, 'Reactive chlorine: a potential sink for dimethylsulfide and hydrocarbons in the marine boundary layer', *Atmos. Environ.,* **30**, i-iii, (1996).

Keene, W. C., D. J. Jacob, and S. M. Fan, 'Reactive chlorine: A potential sink for dimethylsulfide and hydrocarbons in the marine boundary layer', New Directions Commentary*, Atmos. Environ.,* **30**, i-iii, (1996).

Keene W. C. et al., 'Composite global emissions of reactive chlorine from anthropogenic and natural sources: Reactive Chlorine Emissions'. *J. Geophys. Res.,* **104**, 8429-8440, (1999).

Khalil, M. A. K., Rasmussen, R. A., and Gunawardena, R.: 'Atmospheric methyl bromide: Trends and global mass balance', *J. Geophys. Res.*, **98D**, 2887–2896, 1993.

Khalil et al., 'Natural emissions of chlorine-containing gases: Reactive Chlorine Emission Inventories', *J. Geophys. Res.,* **104**, 8333-8346, (1999).

Kleeman, M. J., Schauer, J. J., and Cass, G. R.: 'Size and composition distribution of fine particulate matter emitted from wood burning, meat charbroiling, and cigarettes', *Environ. Sci. Technol.*, **33**, 3516–3523, (1999).

Koelemeijer, R.B.A., 'A Fast method for retrieval of clouds parameters using oxygen A band measurements from the Global Ozone Monitoring Experiment', *J. Geophys. Res.,* **106**, 3475-3490, (2001).

Kolb, C.: 'Iodine's air of importance', *Nature*, **417**, 597–598, (2002).

Kourtidis, K et al., 'Vertical distribution of methyl bromide in the stratosphere', *Geophys. Res. Lett.*, **25**, 505-508, (1998).

Kreher K., 'Spectroscopic Measurements of Atmospheric OClO, BrO and NO$_2$ and their Relation to Antarctic Ozone Depletion', *Ph.D. Thesis*, University of Heidelberg, (1996).

Kreher, K., P. V. Johnston, S. Wood, B. Nardi, and U. Platt, 'Ground-based measurements of tropospheric and stratospheric BrO at Arrival Heights, Antarctica', *Geophys. Res. Lett.*, **24**, 3021–3024, (1997).

Krueger, J., et al., 'Volcanic sulfur dioxide measurements from the total ozone mapping spectrometer instruments', *J. Geophys. Res.*, **100**, 14,057– 14,076, (1995).

Krzyscin, J. W., 'Changes in ozone trends over the northern hemisphere middle latitudes during the period 1970–1990', *Theor. Appl. Climatol*, **49**, 1–7, (1994).

Kromminga, H., J. Orphal, S. Voigt and J. P. Burrows, "Fourier-transform-spectroscopy of symmetric chlorine dioxide (OClO)", *Proc. EC Advanced Study Course*, (ASTAIRE 1999), Bergen, Norway, (1999).

Kurosu, T., Rozanov, V. V., and Burrows, J. P.: Parameterization schemes for terrestrial water clouds in the radiative transfer model GOMETRAN, *J. Geophys. Res.*, **102**, 21 809–21 823, (1997).

Kurosu, T., V. V. Rozanov, and J. P. Burrows: Parameterization schemes for terrestrial water clouds in the radiative transfer model GOMETRAN, *J. Geophys. Res.*, **104**, 8263-8280, (1999).

Lamarque, J. -F. et al., 'Three-dimensional study of the relative contributions of the different nitrogen sources in the troposphere', *J. Geophys. Res.*, **101**, 22955-22968, (1996).

Lary, D. J., 'Gas Phase Atmospheric Bromine Photochemistry', *J. Geophys. Res.*, **101**, 1505-1516, (1996).

Lary, D. J., M. P. Chipperfield, R. Toumi, and T. Lenton, 'Heterogeneous Atmospheric Bromine Chemistry', *J. Geophys. Res.*, **101**, 1489-1504, (1996).

Lary D. J., 'Halogens and the chemistry of the free troposphere', *Atmos. Chem. Phys. Discuss.*, **4**, 5367–5380, (2004).

Lazlo, B., R. E. Huie, M. J. Kurylo, and A. W. Miziolek, Kinetic Studies of the Reactions of BrO and IO Radicals, *J. of Geophys. Res.*, **102**, 1523-1532, (1997).

Lee, A. M., R. L. Jones, I. Kilbane-Dawe, and J. A. Pyle, 'Diagnosing ozone loss in the extratropical lower stratosphere', *J. Geophys. Res.* **107**(D11), doi: 10.1029/2001JD000538, (2002).

Leser, H., Hönninger, G., and Platt, U., 'MAX-DOAS measurements of BrO and NO$_2$ in the marine boundary layer', *Geophys. Res. Lett.*, **30**, 10, doi:10.1029/2002GL015811, (2003).

Levine J. S. (Ed.), 'Biomass Burning and Global change, vol. 1 and vol. 2, Remote Sensing, Modeling and Inventory development and Biomass Burning in Africa', **902**, *MIT Press*, Cambridge, Mass, (1996).

Lindberg, S. E., Brooks, S., Lin, C. -J., Scott, K. J., Meyers, T., Chambers, L., Landis, M. S., Steven, R. K., Formation of Reactive gaseous Mercury in the Arctic: Evidence of oxidation of Hg^0 to gas-phase Hg^{-II} compounds after Arctic Sunrise, *Water, Air, Soil Pollu.* doi: 10.1023/A:1013171509022, **1** (5-6): 295-302, (2001).

Lindberg, S. E., Brooks, C. -J. Lin, K. J. Scott, M. S. Landis, R. K. Stevens, M. Goodsite, A. Richter, Dynamic Oxidation of Gaseous Mercury in the Arctic Troposphere at Polar Sunrise, *Environ. Sci. Techno.*, **36**,1245-1256, (2002).

Lobert, J. M., J. H. Butler, S. A. Montzka, L. S. Geller, R. C. Myers, and J. W. Elkins, 'A net sink for Atmospheric CH_3Br in the cast Pacific Ocean, *Science,* **267**, 1002-1005, (1995).

Lobert, J. M., et al., 'Global chlorine emissions from Biomass burning: Reactive chlorine emissions inventories', *J. Geophys. Res.,* **104**, D7, 8373-8389, (1999).

Lobert, J. M., W.C. Keene, J.A. Logan, R. Yevich, *J. Geophys. Res.* **104**, 8373-8390, (1999).

Lovelock, J. E., R. J. Maggs, and R. J. Wade, 'Halogenated hydrocarbons in and over the Atlantic', *Nature,* **241**, 194 - 196, (1973).

Lovelock, J. E., 'Natural halocarbons in the air and in the sea', *Nature*, **256**, 193 - 194, (1975).

Lu, Y. Julia*,* W. H. Schroeder, L. A. Barrie, A. Steffen, H. E. Welch, K. Martin, L. Lockhart, R. V. Hunt, G. Boila and A. Richter, 'Magnification of atmospheric mercury deposition to polar regions in springtime: the link to tropospheric ozone depletion chemistry', *Geophys. Res. Lett.*, Vol. 28, No. **17**, 3219-3222, (2001).

Maenhaut, W., Salma, I., Cafmeyer, J., Annegarn, H. J., and Andreae, M. O.: Regional atmospheric aerosol composition and sources in the eastern Transvaal, South Africa, and impact of biomass burning, *J. Geophys. Res.*, **101D**, 23 631–23 650, (1996b).

Mankin, W. G., and M. T. Coffey, 'Increased Stratospheric Hydrogen Chloride in the El Chicon cloud', *Science,* **226**, 170-172, (1984).

Martin et al., 'Detection of a lightning influence on tropical tropospheric ozone', *Geophys. Res. Lett.*, **27**, 1639-1642, (2000).

Martinez, M., T. Arnold, D. Perner, 'The role of bromine and chlorine chemistry for arctic ozone depletion events in Ny-Ålesund and comparison with model calculations', *Ann. Geophysicae* **17**, 941-956 Springer-Verlag, (1999).

Maslanik, J., and J. Stroeve, 'DMSP SSM/I daily polar gridded brightness temperatures' [CD-ROM], *Natl. Snow and Ice Data Cent.*, Boulder, Colo., (2003).

Matveev, V., M. Peleg, D. Rosen, D. S. Tov-Alper, K. Hebestreit, J. Stutz, U. Platt, D. R. Blake, and M. Luria, 'Bromine oxide—Ozone Interaction over the Dead Sea', *J. Geophys. Res.,* **106**, 10,375– 10,387, (2001).

McConnell, J. C., G. S. Henderson, L. A. Barrie, J. Bottenheim, H. Niki, C. H. Langford, and E. M. J. Templeton, 'Photochemical bromine production implicated in Arctic boundary-layer ozone depletion', *Nature*, **355**, 150– 152, (1992).

McCormick, M. P., H. M. Steele, P. Hamill, W. P. Chu, and T. J. Swissler, 'Polar Stratospheric Cloud sightings by SAM II', *J. Atmos. Sci.*, **39**, 1387–1397, (1982).

McCormick, M. P., R. E. Veiga, and W. P. Chu, 'Stratospheric ozone profile and total ozone trends derived from the SAGE I and SAGE II data', *Geophys. Res. Lett.*, **19**, 269–272, (1992).

McElroy, M. B., R. J. Salawitch, S. C. Wofsy, and J. A. Logan, 'Reductions of Antarctic ozone due to synergistic interactions of chlorine and bromine', *Nature*, **321**, 759–762, (1986).

McElroy, C. T., C. A. McLinden, and J. C. McConnell, 'Evidence for bromine monoxide in the free troposphere during the Arctic polar sunrise', *Nature*, **397**, 338–341, (1999).

McFiggans, G., J. C. Plane, B. J. Allan, L. J. Carpenter, H. Coe, and C. D. O'Dowd, 'Modeling study of iodine chemistry in the marine boundary layer', *J. Geophys. Res.*, **105**, 14,371–14,385, (2000).

McFiggans, G., H. Coe, R. Burgess et al., 'Direct evidence for coastal iodine particles from Laminaria macroalgae – linkage to emissions of molecular iodine', *Atmos. Chem. Phys.*, **4**, 701–713, (2004).

McGrath M. P., Clemitshaw, K. C., Rowland, F. S., and Hehre, W. J., 'Structures, relative stabilities, and vibrational spectra of isomers of Cl_2O_2: the role of chlorine oxide dimmer in Antarctic ozone depletion mechanisms', *J. Phys. Chem*., **94,** 6126-6132, (1990).

McKenzie, L. M., Ward, D. E., and Hao, W. M.: 'Chlorine and bromine in the biomass of tropical and temperate ecosystems, in: Biomass Burning and Global Change, Vol. 1, Remote Sensing, Modeling and Inventory Development, and Biomass burning in Africa', edited by Levine, J. S., pp. 241–248, The MIT press, Cambridge, Massachusetts, USA, (1996).

McKinlay, A. F. and B. L. Diffey: 'A reference action spectrum for ultraviolet induced erythema in human skin'. CIE Research Note, CIE-Journal, **Vol. 6**, No.1 (17-22), (1987).

McLinden, C. A., S. C. Olsen, B. J. Hannegan, O. Wild, M. J. Prather, and J. Sundet, 'Stratospheric ozone in 3-D models: A simple chemistry and the cross-tropopause flux', J. Geophys. Res., **105**, 14,653-14,665, (2000).

McPeters, R. D., and G. J. Labow, 'An assessment of the accuracy of 14.5 years of Nimbus 7 TOMS version 7 Ozone data by comparison with the Dobson network', *Geophys. Res. Lett*., **23**, 3695–3698, (1996a).

McPeters, R. D., S. M. Hollandsworth, L. E. Flynn, J. R. Herman, and C. J. Seftor, 'Long-term ozone trends derived from the 16-year combined Nimbus 7/Meteor 3 TOMS version 7 record', *Geophys. Res. Lett*., **23,** 3699–3702, (1996b).

Mickley, L. J., Murti, P. P., Jacob, D. J., Logan, J. A., Koch, D. M., Rind, D., 'Radiative forcing from tropospheric ozone calculated with a unified chemistry-climate model', *J. Geophys Res.,* **104**, 30153–30172, (2001).

Miller, A. J., G. C. Tiao, G. C. Reinsel, D. Wuebbles, L. Bishop, J. Kerr, R. M. Nagatani, J. J. DeLuisi, and C. L. Mateer, 'Comparisons of observed ozone trends in the stratosphere through examinations of Umkehr and Balloon Ozonesonde data', *J. Geophys. Res.*, **100**, 11,209 –11,217, (1995).

Mochida, M., J. Hirokawa, Y. Kajii, and H. Akimoto, 'Heterogeneous reactions of Cl_2 with sea salts at ambient temperature: Implications for halogen exchange in the atmosphere', *Geophys. Res. Lett*., **25**, 3927 - 3930, (1998).

Molina, L. T., and M. J. Molina, 'Production of Cl_2O_2 from the self-reaction of the ClO radical', *J. Phys. Chem.*, **91,** 433–436, (1987).

Molina, M. J., Colussi, A. J., Molina, L. T., Schindler, R. N., and Tso, T. –L. 'Quantum yield of chorine-atom formation in the photodissociation of chlorine peroxide (ClOOCl) at 308 nm', *Chem. Phys. Lett.*, **173,** 310-315, (1990).

Molina, M. J., 'Heterogeneous chemistry on polar stratospheric clouds', *Atmos. Environ.,* **25A,** 2535-2537, (1991).

Moore, R. M., and W. Groszko, 'Methyl Iodide distribution in the ocean and fluxes to the atmosphere', *J. Geophys. Res.,* **104**, 11,163–11,171, (1999).

Mozurkewich, M., 'Mechanisms for the release of halogens from sea-salt particles by free radicals reactions', *J. Geophys. Res.,* **100**, 14199-14207, (1995).

Murphy, D.M. and D.W. Fahey, 'An estimate of the flux of stratospheric reactive nitrogen and ozone into the troposphere', *J. Geophys. Res.*, **99**, 5325-5332, (1994).

Newman, P. A., J. G. Gleason, R. D. McPeters, and R. S. Solarski, 'Anomalously low ozone over the Arctic', *Geophys. Res. Lett.*, **24**, 2689–2692, (1997).

Noel, S., Bovensmann, H., Wuttke, M. W., Burows, J. P., Gottwald, M., Krieg, E., Goede, A. H. P., and Mager, R., 'SCIAMACHY nomial operations and special features', In *Proc. ERS-ENVISAT symposium Gothenburg, 10-16 Oct. 2000, CD-ROM (SP-461)*, (2000).

O'Dowd, C. D et al.: 'A dedicated study of new particle formation and fate in the coastal environment (PARFORCE): Overview of objectives and achievements', *J. Geophys. Res.*, **107**, D19, 8108, doi:10.1029/2001JD000555, (2002).

O'Dowd, C. D., Jimenez, J. L., Bahreini, R., Flagan, R. C., Seinfeld, J. H., H¨ameri, K., Pirjola, L., Kulmala, M., Jennings, S. G., and Hoffmann, T.: Marine aerosol formation from biogenic iodine emissions, *Nature*, **417**, 632–636, (2002).

Oltmans, S. J., Komhyr, W. D., 'Surface ozone distributions and variations from 1973-1984 measurements at the NOAA geophysical monitoring for climatic change baseline observatories' *J. Geophys. Res.,* **91**, 5229 - 5236, (1986).

Otten, C., F. Ferlemann, U. Platt, T. Wagner, and K. Pfeilsticker, 'Ground-based DOAS UV/visible measurements at Kiruna (Sweden) during the SESAME winters 1993/94 and 1994/95', *J. Atmos. Chem.,* **30**, 141– 162, (1998).

Ozone Trends Panel (OTP), Report of the international ozone trends panel, *WMO Rep. 18, World Meteorol. Organ.,* Geneva, (1988).

Park, J. H., M. K. W. Ko, C.H. Jackman, R. A. Plumb, J. A. Kaye, and K. H. Sage, 'Report of the Models and Measurements Intercomparison II', pp. 502, Langley Research Center, NASA, Hampton, Virginia, (1999).

Penkett, S. A., J. H. Butler, M. J. Kurylo, C. E. Reeves, J. M. Rodriguez, H. Singh, D. Toohey, and R. Weiss, 'Methyl bromide, in *Scientific Assessment of Ozone Depletion: 1994', Rep. 37,* pp. 10.1-10.26, *WMO Global Ozone Res. And Monit. Proj., Geneva,* (1995).

Penner, J. E., S. Y. Zhang, M. Chin, C. C. Chuang, J. Feichter, Y. Feng, I. V. Geogdzhayev, P. Ginoux, M. Herzog, A. Higurashi, D. Koch, C. Land, U. Lohmann, M. Mishchenko, T. Nakajima, G. Pitari, B. Soden, I. Tegen, and L.

Stowe, 'A comparison of model- and satellite-derived aerosol optical depth and reflectivity', *J. Atmos. Sci.*, **59**, 441-460, doi:10.1175/1520-0469, (2002).

Perovich, D., and J. A. Richter-Menge, 'Surface characteristics of lead ice', *J. Geophys. Res.*, **99** (C8), 16,341–16,350, (1994).

Peters, C., S. Pechtl, J. Stutz, K. Hebestreit, G. Hönninger, K. G. Heumann, A. Schwatz, J. Winterlik, U. Platt, 'Reactive and organic halogen species in three different European coastal environments', *Atmos. Chem. Phys. Discuss.*, **5**, 6077-6126, (2005).

Petersen, V., Iverfeldt, A. and Munthe J., 'Atmospheric mercury species over Central Europe, 'Model calculations and comparison with observations from the Nordic Air and Precipitation network for1987 and 1988', *Atmos. Environ.*, **29**, No. 1, pp. 47-67, (1995).

Pfeilsticker, K., F. Erle, O. Funk, L. Marquard, T. Wagner, and U. Platt: 'Optical path modifications due to tropospheric clouds: Implications for zenith sky measurements of stratospheric gases', *J. Geophys. Res.,* **103**, 25323-25335, (1998).

Pfeilsticker, K., W. T. Sturges, H. Bösch, C. Camy-Peyret, M. P. Chipperfield, A. Engel, R. Fitzenberger, M. Müller, S. Payan, and B. -M. Sinnhuber, Lower stratospheric organic and inorganic bromine budget for the Arctic winter 1998/99, Geophys. Res. Lett., **27,** 3305– 3308, (2000).

Platt, U., 'Differential Optical Absorption Spectroscopy (DOAS) in Air Monitoring by Spectroscopic Techniques', (ed. Sigrist, M.W.), Vol **127** of *Chemical Analysis Series*, John Wiley and Sons, New York, (1994).

Plumb, R. A., 'A tropical pipe model of stratospheric transport', *J. Geophys. Res.*, **101**, 3957–3972, (1996).

Pszenny, A. A. P., W. C. Keene, D. J. Jacobs, S. Fan et al., 'Evidence of Inorganic Chlorine Gases Other than Hydrogen Chloride in Marine Surface Air', *Geophys. Res. Lett.,* **20**, 699-702, (1993).

Pundt, I., et al., 'Simultaneous UV-vis measurements of BrO from Balloon, Satellite and Ground: Implications for Tropospheric BrO', in *Fifth European Workshop on Stratospheric Ozone*, vol. 1, pp. 316–319, (2000).

Pundt, I., J. - P. Pommereau, M. P. Chipperfield, M. Van Roozendael, and F. Goutail, 'Climatology of the stratospheric BrO vertical distribution by balloon-borne UV–visible spectrometry', *J. Geophys. Res.*, 107(D24), 4806, doi: 10.1029/2002JD002230, (2002).

Pyle, J. A., G. Carver, J. L. Grenfell, J. A. Kettleborough, and D. J. Lary, 'Ozone loss in Antarctica: The implications for global change', *Philos. Trans. R. Soc. London, Ser. B, 338*, 219–226, (1992).

Rankin, A. M., E. W. Wolff, and S. Martin, 'Frost flowers: Implications for tropospheric chemistry and ice core interpretation', *J. Geophys. Res.*, **107**(D23), 4683, doi: 10.1029/2002JD002492, (2002).

Rankin, A., and E. W. Wolff, 'A year-long record of size segregated aerosol composition at Halley, Antarctica, *J. Geophys. Res.*, **108**(D24), 4775, doi:10.1029/2003JD003993, (2003).

Richter, A., F. Wittrock, M. Eisinger and J. P. Burrows, 'GOME observations of tropospheric BrO in Northern Hemispheric spring and summer 1997', *Geophys. Res. Lett.*, *No*. **25**, pp. 2683-2686, (1998).

Richter, A., M. Eisinger, A. Ladstätter-Weißenmayer and J. P. Burrows, 'DOAS zenith sky observations: 2. Seasonal variation of BrO over Bremen (53° N), 1994-1995', *J. Atm. Chem.*, *No*. **32**, pp. 83-99, (1999).

Richter, A., T. Wagner, 'Diffuser plate spectral structures and their influence on GOME slant columns', *Technical note*, available at http://www.iup.physik.uni-bremen.de/gome/ (2001).

Richter, A., F. Wittrock, A. Ladstätter-Weißenmayer, and J. P. Burrows, 'GOME measurements of stratospheric and tropospheric BrO', *Adv. Space Res.*, **29** (**11**), 1667-1672, (2002).

Richter, A., V. Eyring, J. P. Burrows, H. Bovensmann, A. Lauer, B. Sierk, and P. J. Crutzen, 'Satellite measurements of NO_2 from international shipping emissions' *Geophys. Res. Lett.*, **31**, L23110, doi:10.1029/2004GL020655, (2004).

Richter, A., F. Wittrock, M. Weber, S. Beirle, S. Kühl, U. Platt, T. Wagner, W. Wilms-Grabe, and J. P. Burrows, 'GOME observations of stratospheric trace gas distributions during the splitting vortex event in the Antarctic winter 2002 Part I: Measurements', *J. Atmos. Sci.*, **62**, (**3**), 778-785, (2005).

Richter U. and D. W. R. Wallace, 'Production of methyl iodide in the tropical Atlantic Ocean', *Geophys. Res. Lett.,* **31**, L23S03, doi: 10.1029/2004GL020779, (2004).

Ridley, B. A., et al., 'Ozone depletion events observed in the high latitude surface layer during the TOPSE aircraft program', *J. Geophys. Res.*, **108(D4)**, 8356, doi:10.1029/2001JD001507, (2003).

Rozanov, V., Diebel, D., Spurr, R. J. D., and Burrows, J. P., 'GOMETRAN: A radiative transfer model for the satellite project GOME - the plane-parallel version', *J. Geophys. Res.*, **102**, 16683-16695, (1997).

Rozanov, V., Kurosu, T., and Burrows, J. P., 'Retrieval of atmospheric constituents in the UV-visible: 'A new quasi-analytical approach for the calculation of weighting functions. *J. Quant. Spectrosc. Radiat. Transfer*', **60**, 277-299, (1998).

Rozanov, A., Rozanov, V., and Burrows, J. P., 'Combined differential-integral approach for the radiation field computation in a spherical shell atmosphere: Non-limb geometry', *J. Geophys. Res.*, **105**, 22937-22942, (2000).

Rozanov, A., Rozanov, V., and Burrows, J. P., 'A numerical radiative transfer model for a spherical planetary atmosphere: combined differential integral approach involving the Picard iterative approximation. *J. Quant. Spectrosc. Radiat. Transfer*, **69**, 491-512, (2001).

Rozanov, A., Rozanov, V., and Burrows, J. P., 'Evaluation of the Combined Differential-Integral Approach for Limb Viewing Geometry', *Adv. Space Res.*, **29**, 1843-1848, (2002).

Saiz-Lopez, A., and J. M. C. Plane, 'Novel iodine chemistry in the marine boundary layer', *Geophys. Res. Lett.*, **31**, L04112, doi:10.1029/2003GL019215, (2004).

Saiz-Lopez, A., J. M. C. Plane and J. A. Shillito, 'Bromine oxide in the mid-latitude marine boundary layer', *Geophys. Res. Lett.*, **31**, L03111, doi: 10.1029/2003GL018956, (2004)

Sander, R., R. Vogt, G. W. Harris, and P. J. Crutzen, Modeling the chemistry of ozone, halogen compounds, and hydrocarbons in the arctic troposphere during spring, *Tellus*, **49B**, 522–532, (1997).

Sander, R., Rudich, Y., von Glasow, R., and Crutzen, P. J.: The role of $BrNO_3$ in marine tropospheric chemistry: A model study, *Geophys. Res. Lett.,* **26**, 2857–2860, (1999).

Sander, R. et al., 'Inorganic bromine in the marine boundary layer: a critical review', *Atmos. Chem. Phys.*, **3**, 1301–1336, (2003).

Schauffler, S. M., Atlas, E. L., Flocke, F., Lueb, R. A., Stroud, V., and Travnicek, W., 'Measurements of bromine containing organic compounds at the tropical tropopause', *Geophys. Res. Lett.*, **25**, 317-320, (1998).

Schauffler, S. M., E. L. Atlas, D. R. Blake, F. Flocke, R. A. Lueb, J. M. Lee-Taylor, V. Stroud, and W. Travnicek, Distributions of brominated organic compounds in the troposphere and lower stratosphere, *J. Geophys. Res.,* **104**, 21,513– 21,535, (1999).

Schofield, R., 'The Vertical Distribution of Atmospheric BrO from Ground-Based Measurements', *PhD Thesis*, University of Auckland, (2003).

Schofield, R., K. Kreher, B. J. Connor, P. V. Johnston, A. Thomas, D. Shooter, M. P. Chipperfield, C. D. Rodgers, and G. H. Mount, 'Retrieved tropospheric and stratospheric BrO columns over Lauder, New Zealand', *J. Geophys. Res.,* **109**, D14304, doi:10.1029/2003JD004463, (2004).

Schroeder, W.H. & J. Munthe 'Atmospheric Mercury - An Overview', *Atmos. Environ.*, **32**, pp. 809-822, (1998).

Schultz, M. G., D. J. Jacob, Y. Wang, J. A. Logan, E. L. Atlas, D. R. Blake, N. J. Blake, J. D. Bradshaw, E. V. Browell, M. A. Fenn, F. Flocke, G. L. Gregory, B. G. Heikes, G. W. Sachse, S. T. Sandholm, R. E. Shetter, H. B. Singh, and R. B. Talbot, On the Origin of Tropospheric Ozone and NO_x over the Tropical South Pacific, *J. Geophys. Res.*, **104**, 5829-5843, (1999).

Seinfeld, J. H. and S. N. Pandis, 'Atmospheric Chemistry and Physics – from Air Pollution to Climate Change', *John Wiley and Sons*, New York, Chichester, Weinheim, ISBN 0-471-17815-2, (1998).

Seisel, S. and M. Rossi, 'The heterogeneous Reaction of HONO and HBr on Ice and on Sulfuric Acid', *Ber. Bunsen- Ges. Phys. Chem.*, Vol. **101**, 943-955, 1997.

Sinnhuber, B.-M., et al., 'Intercomparison of measured and modeled slant column densities', *J. Geophys. Res.*, **107**(D19), 4398, doi: 10.1029/ 2001JD000940, (2002).

Sinnhuber, B.-M., A. Rozanov, N. Sheode, O. T. Afe, A. Richter, M. Sinnhuber, F. Wittrock, J. P. Burrows, G. P. Stiller, T. Clarmann, A. Linden, 'Global observations of stratospheric bromine monoxide from SCIAMACHY', accepted for publication in *Geophys. Res. Lett.*, (2005).

Singh, H.B. et al., 'Low ozone in the marine boundary layer of the tropical Pacific Ocean: photochemical loss, chlorine atoms, and entrainment', *J. Geophys. Res., 101*, 1907-1917, (1996).

Smith, R. A., 'Air and Rain: The Beginnings of a Chemical Climatology', *Longmans*, Green, London 1872.

Solomon, S., and R. R. Garcia, 'On the distributions of long-lived tracers and chlorine species in the middle atmosphere', *J. Geophys. Res.*, **89**, 11,633–11,644, (1984).

Solomon, S., R. R. Garcia, F. S. Rowland, and D. J. Wuebbles, 'On the depletion of Antarctic ozone', *Nature*, **321**, 755–758, (1986).

Solomon, S., A. L. Schmeltekopf, and R. W. Sanders, 'On the Interpretation of Zenith-Sky Absorption Measurements', *J. Geophys. Res, 92, 8311-8319,* (1987).

Solomon, S., R. R. Garcia, and A. R. Ravishankara, 'On the role of iodine in ozone depletion', *J. Geophys. Res.*, **99,** 20,491–20,499, (1994).

Solomon, S., R. W. Portmann, R. W. Sanders, and J. S. Daniel, 'Absorption of Solar Radiation by Water Vapor, Oxygen, and Related Collision Pairs in the Earth's Atmosphere', *J. Geophys. Res.*, **103**, 3847-3858, (1998).

Solomon, S., Stratospheric ozone depletion: A review of concepts and history, *Rev. Geophys., 37*, 275– 316, (1999).

Sommar, J. I., I. Wängberg, T. Berg, K. Gårdfeldt, J. Mlunthe, A. Richter, A. Urba, F. Wittrock, W. H. Schroeder, 'Circumpolar transport and air-surface exchange of atmospheric mercury at Ny-Ålesund, (79° N), Svalbard, spring 2002', *Atmos. Phys. Chem. Discuss., 4*, 1727 – 1771, (2004).

Spicer, C.W., E.G. Chapman, B. J. Finlayson-Pitts, R. A. Plastridge, J. M. Hubbe, J. D. Fast, and C. M. Berkowitz, 'First observations of Cl_2 and Br_2 in the marine troposphere', *Nature, 394,* 353-356, (1998).

Staehelin, J., A. Renaud, J. Bader, R. McPeters, P. Viatte, B. Hoegger, V. Bugnion, M. Giroud, H. Schill, 'Total ozone series at Arosa (Switzerland): Homogenization and data comparison', *J. Geophys. Res.*, **103** (D5), 5827-5842, 10.1029/97JD02402, (1998).

Staehelin, J., R. Kegel, N. R. P. Harris, 'Trend analysis of the homogenized total ozone series of Arosa (Switzerland), 1926 – 1996', *J. Geophys. Res.*, **103** (D7), 8389-8400, 10.1029/97JD03650, (1998).

Stolarski, R. S., A. J. Krueger, M. R. Schoeberl, R. D. McPeters, P. A. Newman, and J. C. Alpert, 'Nimbus 7 satellite measurements of the springtime Antarctic ozone decrease', *Nature*, **322**, 808–811, (1986).

Stolarski, R. S., P. Bloomfield, R. D. McPeters, and J. R. Herman, 'Total ozone trends deduced from Nimbus 7 TOMS data', *Geophys. Res. Lett.*, **18**, 1015–1018, (1991).

Stumm, W. and Brauner, P. A.: 'Chemical Speciation, in: Chemical Oceanography', Vol. 1, 2nd Ed., edited by Riley, J. P. and Skirrow, G., pp. 173–239, *Academic Press*, (1975).

Sturges, W. T., et al., "Bromoform as a source of bromine to the stratosphere", *Geophys. Res. Lett.*, **27**, 2081-2084, (2000).

Stutz, J., R. Ackermann, J. D. Fast, and L. Barrie, 'Atmospheric reactive chlorine and bromine at the Great Salt Lake, Utah' *Geophy. Res. Lett.*, 29 (10), art. no.-1380, (2002).

Symonds, R. B., W. J. Rose and M. H. Reed, 'Contribution of Cl- and F- bearing gases to the atmosphere by volcanoes', *Nature*, 334, 415-418, (1988).

Talbot, R. W., Dibb, J. E., Scheuer, E. M., Blake, D. R., Blake, N. J., Gregory, G. L., Sachse, G. W., Bradshaw, J. D., Sandholm, S. T., and Singh, H. B.: Influence of biomass combustion emissions on the distribution of acidic trace gases over the southern Pacific basin during austral springtime, *J. Geophys. Res.*, -A., 104(D5), 5623–5634, (1999).

Tang, T. and McConnell, J. C., 'Autocatalytic release of bromine from Arctic snow pack during polar sunrise', *Geophys. Res. Lett.*, **23**, 2633-2636, (1996).

Thompson, A. M., et al., 'Where did tropospheric ozone over Southern Africa and the tropical Atlantic come from in October 1992: Insights from TOMS, GTE TRACE A, and SAFARI 1992', *J. Geophys. Res.*, **101**, 24251-24278, (1996).

Toumi, R., 'BrO as a sink for dimethylsulphide in the marine atmosphere', *Geophys. Res. Lett.*, **21**, 117-120, (1994).

Tuckermann, M., R. Ackermann, C. Gölz, H. Lorenzen-Schmidt, T. Senne, J. Stutz, . Trost, W. Unold, and U. Platt, 'DOAS-observation of halogen radical-catalysed Arctic boundary layer ozone destruction during the ARCTOC-campaigns 1995 and 1996 in Ny-Alesund, Spitsbergen', *Tellus*, **49B**, 533-555, (1997).

Quack, B. and Wallace, D. W. R., 'Air-sea flux of bromoform: Controls, rates, and implications, *Global Biogeochem. Cycles*, **17**, 10.1029/2002GB001 890, (2003).

UNEP/WMO Report (2002), *Executive Summary, Scientific Assessment of Ozone Depletion*: 2002.

Van Roozendael, M., M. de Maziere, and P. C. Simon, 'Ground-based visible measurements at the Jungfraujoch station since 1990', *J. Quant. Spectrosc. Radiat. Transfer,* **52**, 231–240, (1994).

Van Roozendael, M., C. Fayt, J. -C. Lambert, I. Pundt, T. Wagner, A. Richter, and K. Chance, 'Development of a bromine oxide product from GOME', in Proc. ESAMS '99, *European Symposium on Atmospheric Measurements from Space*, WPP-161, pp. 543– 547, ESTEC, Noordwijk, Netherlands, 18– 22 January (1999).

Van Roozendael, M., T. Wagner, A. Richter, I. Pundt, D. W. Arlander, J.P. Burrows, M. Chipperfield, C. Fayt, P.V. Johnston, J.-C. Lambert, K. Kreher, K. Pfeilsticker, U. Platt, J. -P. Pommereau, B.-M. Sinnhuber, K. K. Toernkvist, and F. Wittrock: 'Intercomparison of BrO Measurements from ERS-2 GOME, ground-based and Balloon Platforms', *Adv. Space Res.*, **29(11)**, 1661-1666, (2002).

Van Roozendael, M., I. De Smedt, C. Fayt, F. Hendrick, H. Oetjen, F. Wittrock, A. Richter, O. Afe, 'First Validation of SCIAMACHY BrO Columns', submitted to the *Atmospheric Chemistry Validation of ENVISAT (ACVE-2) proceedings*, 3-7th May 2004, Frascasti, Italy, *(European Space Agency (ESA), Special Publication, SP-562, August 2004) ESC02MVR. Published on CD-ROM.* Available at: *http://envisat.esa.int/workshops/acve2/papers/ESC02MVR.pdf*, (2004).

Vogt, R., Crutzen, P. J., and Sander, R.: 'A mechanism for halogen release from sea-salt aerosol in the remote marine boundary layer', *Nature*, **383**, 327–330, (1996).

Vogt, R., Sander, R., von Glasow, R., and Crutzen, P. J.: 'Iodine chemistry and its role in halogen activation and ozone loss in the marine boundary layer: A model study', *J. Atmos. Chem*., **32**, 375–395, (1999).

Vountas, M., V.V. Rozanov, and J. P. Burrows, Ring effect: 'Impact of rotational Raman scattering on radiative transfer in earth's atmosphere', *J. Quant. Spectrosc. Radiat. Transfer,* **60** (**6**), 943-961, (1998).

Wagenbach, D., F. Ducroz, R. Mulvaney, L. Keck, A. Minikin, M. Legrand, J. S. Hall, and E. W. Wolff, 'Sea-salt aerosol in coastal Antarctic regions', *J. Geophys. Res.,* **103**(**D9**), 10,961– 10,974, (1998).

Wahner, A., Ravishankara A. R., Sander S. P., Friedl R. R., 'Absorption cross-section of BrO between 312 and 385 nm at 298 and 223 K', *Chem. Phys. Lett.,* **152***,* 507-12, (1988).

Wagner, T., and U. Platt, 'Satellite mapping of enhanced BrO concentrations in the troposphere', *Nature*, **395**, 486–490, (1998).

Wagner, T., 'Satellite observations of atmospheric halogen oxides, Ph.D. thesis, University of Heidelberg, Germany', (1999).

Wagner, T., C. Leue, M. Wenig, K. Pfeilsticker, U. Platt, Spatial and temporal distribution of enhanced boundary layer BrO concentrations measured by the GOME instrument aboard ERS-2, *J. Geophys. Res*., **106** (D20), 24225-24236, 10.1029/2000JD000201, (2001).

Wagner, T., C. von Freideburg, M. Wenig, C. Otten, and U. Platt, 'UV-visible observations of atmospheric O_4 absorptions using direct moonlight and zenith-scattered sunlight for clear-sky and cloudy-sky conditions', *J. Geophys. Res*. Vol. **107**, D20, 4424, doi: 10.1029/2001JD001026, (2002).

Wallace, J. M. and P. V. Hobbs, 'Atmospheric Science – An Introductory Survey', Academic Press, *Elsevier Science*, USA, **ISBN** 0-12-732950-1, (1977).

Wamsley, P. R. et al., 'Distribution of Halon-1211 in the upper Troposphere and Lower Stratosphere and the 1994 Total Bromine Budget', *J. Geophys. Res.,* **103***,* 1513-1526, (1998).

Wayne, R. P. et al., 'Halogen Oxides – Radicals, Sources and Reservoirs in the Laboratory and the Atmosphere', *Atmos. Environ.*, **29***,* 2677-2881, (1995).

Wayne, R. P., 'Chemistry of Atmospheres', *Third Edition*, Oxford University Press, ISBN 0 19 850375-X, (2000).

Weber, M., J. P. Burrows and R. P. Cebula, 'GOME Solar UV/VIS Irradiance Measurements between 1995 and 1997 - First Results on Proxy Solar Activity Studies, *Solar Physics,* **177**, 63-77, (1998).

Wennberg, P. O., R. C. Cohen, R. M. Stimpfle, J. P. Koplow, J. G. Anderson, R. J. Salawitch, D. W. Fahey, E. L. Woodbridge, E. R. Keim, R. S. Gao, C. R. Webster, R. D. May, D. W. Toohey, L. M. Avallone, M. H. Proffitt *et al*., 'Removal of Stratospheric Ozone by Radicals: *In Situ* measurements of OH, HO_2, NO, NO_2, ClO, and BrO', *Science,* **266***,* 398-404, (1994).

Wessel, S., Aoki, S., Winkler, P., Weller, R., Herber, A., Gernandt, H., and Schrems, O., 'Tropospheric ozone depletion in polar regions: A comparison of observations in the Arctic and Antarctic', *Tellus*, 50B, 34–50, (1998).

Wilmouth, D. M., T. F. Hanisco, N. M. Donahue, and J. G. Anderson, 'Fourier Transform Ultraviolet Spectroscopy of the A($^2\Pi_{3/2}$)← X($^2\Pi_{3/2}$) Transition of BrO', *J. Phys. Chem.,***103**, 8935-8944, (1999).

Wittrock, F., M. Eisinger, A. Ladstätter-Weißmayer, A. Richter, and J. P. Burrows, 'Ground based UV/VIS measurements of O_3, NO_2, BrO and OClO over Ny-Ålesund (78°N)', *XVIII Quadr. Ozone Symp. (IO3C), L'Aquila, Italy*, September, (1996).

Wittrock, F., R. Müller, A. Richter, H. Bovensmann, and J.P. Burrows, 'Observations of Iodine monoxide above Spitsbergen', *Geophy. Res. Lett.,* Vol. **27**, No. 10, pg. 1471-1474, (2000).

World Meteorological Organization (WMO): Scientific Assessment of Ozone Depletion: 1994, Global Ozone Research and Monitoring Project, Report no. 37, published February 1995; 1998 update, *Report No*. **44**, published February, 1999.

World Meteorological Organization (WMO), *Glob. Ozone Res. Monitor. Proj. Rep.* **44,** Ch. 4., (1999).

World Meteorological Organization (WMO), Scientific Assessment of Ozone Depletion: 2002, in *Global Ozone Research and Monitoring Project - Report No. 47*, Geneva, (2003).

Yokouchi, Y., Machida, T., Barrie, L. A., Toom-Sauntry, D., Nojiri, Y., Fujinuma, Y., Inuzuka, Y., Li, H.-J., Akimoto, H., and Aoki, S.: Latitudinal distribution of atmospheric methyl bromide: measurements and modeling, *Geophys. Res. Lett.*, **27**, 697–700, (2000).

Yung, Y. L., J. P. Pinto, R. T. Watson, and S. P. Sander, Atmospheric bromine and ozone perturbations in the lower stratosphere, *J. Atmos. Sci.*, *37*, 339–353, (1980).

Zetzsch C. and Behnke W., 'Heterogeneous reactions of chlorine compounds, NATO-ASI Series Subseries I - Global Environmental Change'. Vol. 7 (edited by H. Niki and K.H. Becker), *Springer-Verlag*, 291-306, (1993).

Zerefos, C. S., A. F. Bais, J. C. Ziomas and R. D. Bojkov, 'On the relative importance of Quasi-Biennial Oscillation and El Nino/Southern Oscillation in the Revised Dobson Total Ozone Records', *J. Geophys. Res.*, **97**, 10135-10144, (1992).

Zerefos, D. S., K. Tourpali, B. R. Bojkov, D. S. Balis, B. Rognerund, and I. S. A. Isaksen, 'Solar activity-total column ozone relationships: Observations and model studies with heterogeneous chemistry', *J. Geophys. Res.*, **102**, 1561–1569, (1997).